

Frequency Scan Based Stability Analysis of Power Electronic Systems

by

Mahsa Shirinzad

A thesis submitted to
The Faculty of Graduate Studies of
The University of Manitoba
in partial fulfillment of the requirements
of the degree of

Master of Science

Department of Electrical and Computer Engineering
The University of Manitoba
Winnipeg, Manitoba, Canada
January 2021

© Copyright 2021 by Mahsa Shirinzad

Abstract

Frequency scanning is a numerical method for extracting the frequency response of a power electronic system (PES). This technique is performed via injecting a small-amplitude wide-band signal in the time-domain simulation of a PES at steady state. This thesis presents the stability analysis of the interactions between a PES and its ac grid using frequency scanning techniques.

Frequency scanning techniques in different domains are used to extract the model of PESs and the ac grids independently. These results are then compared and the advantages and disadvantages of each of these techniques are presented. Using the obtained models of PESs and the ac grids, two different approaches i.e. the Generalized Nyquist Criterion (GNC) and the Eigenlocus Stability Analysis are applied to access the stability of the combined system. A comparison is given on the use of these methods for stability analysis.

The results obtained from the frequency scanning can be used for other applications such as finding the stability margin of the multiple input multiple output (MIMO) systems using the results of the eigenlocus approach. The adverse interactions can then be stabilized by increasing the strength of the ac grid.

The approximate stability screening technique based on the positive and negative sequence impedance/admittance can also be used for stability screening in grid-connected PESs. Although this technique is widely used in industry and generally gives correct indications of stability, it can give erroneous results due to the small but existent cross-coupling of frequencies. As a result, this thesis recommends using the DQ-based frequency scanning for stability screening purposes instead of using the positive/negative sequence-based approximate stability screening technique.

Contents

Abstract	ii
Table of Contents	vii
List of Abbreviations	xv
Acknowledgments	xviii
Dedication	xix
Chapter 1 Introduction	1
1.1 Background	1
1.2 Stability Analysis of the Interactions in grid-connected PESs	3
1.3 Small-Signal Stability Analysis Techniques	4
1.3.1 State-Space Based Stability Analysis	5
1.3.2 Impedance-Based Stability Analysis	5
1.4 Impedance-Based Approach: Impedance Extraction Techniques	7
1.5 Impedance Extraction Using Shunt Current and Series Voltage Injections	8
1.6 Problem definition	9
1.7 Frequency Scanning	10
1.8 Literature Review on Frequency Scanning an Stability Analysis	12
1.8.1 Research Gaps	15
1.8.2 Thesis Objectives	15

1.9	Thesis Organization	16
Chapter 2	Frequency Scanning Techniques	17
2.1	Introduction	17
2.2	Frequency Scanning of PESs	18
2.3	Voltage Injection Versus Current Injection	20
2.3.1	Single-Tone Injection	20
2.3.2	Multi-Tone Injection	21
2.4	Selecting an Injection Domain	26
2.5	Frequency Scanning Using Phase Variables	27
2.6	Frequency Scanning Using Sequence Variables	29
2.7	Relationship Between Phase and Sequence Variables	32
2.7.1	Case Study: Sequence-Based Frequency Scanning of a Trans- mission Network	33
2.7.2	Case Study: Sequence-Based Frequency Scanning of a STATCOM	35
2.7.3	Advantages and Disadvantages of Phase/Sequence-based Fre- quency Scanning	39
2.7.4	Mirror Frequency Coupling	39
2.7.5	Case Study: Frequency Coupling Phenomena in a Transmission Network	41
2.7.6	Case Study: Frequency Coupling Phenomena in a STATCOM	42
2.8	Solution for Distorted frequency Scanning	43
2.8.1	Case Study: Sequence-Based Frequency Scanning of a STAT- COM Obtained by Dividing the Frequency Range	45

2.9	Frequency Scanning Using DQ Variables	46
2.9.1	Case Study: DQ-Based Frequency Scanning of a Transmission Network	51
2.9.2	Case Study: DQ-Based Frequency Scanning of a STATCOM .	53
2.9.3	Absence of Frequency Interference Using DQ-Based Frequency Scanning	54
2.9.4	Relationship Between Sequence and DQ Variables	56
2.10	$\alpha\beta$ -Based Frequency Scanning	60
2.10.1	Case Study: $\alpha\beta$ -Based Frequency Scanning of a STATCOM .	64
2.11	Conclusion	65
Chapter 3	Stability Analysis of PES-Grid Interactions	66
3.1	Introduction	66
3.2	Interaction Study of Grid-connected PESs	67
3.2.1	Perturbation Via Current Signal	68
3.2.2	Perturbation Via Voltage Signal	70
3.2.3	Equivalence Between the Current Perturbation and the Voltage Perturbation for Stability Screening	73
3.3	Stability Analysis Criterion	75
3.4	Generalized Nyquist Stability Criterion	77
3.5	Eigenlocus Stability Analysis	77
3.6	Encirclement of a Contour around the Origin or $(-1, 0)$	78
3.7	Case Study: Stability Analysis of the CIGRE-HVDC Benchmark Model	80
3.7.1	Case 1: Stable Case ($K_p = 1.0 \text{ rad/p.u.}$)	82

3.7.2	Case 2: Unstable Case ($K_p = 3.0 \text{ rad/p.u.}$)	84
3.7.3	Validation by EMT Simulation	86
3.8	The Problem of Interchanging Eigenvalues	87
3.9	Conclusion	90
Chapter 4	Frequency Scanning Applications	91
4.1	Introduction	91
4.2	Determining the Gain Margin Using Nyquist Stability Approach	92
4.3	Finding the Gain Margin Using Eigenlocus Stability Approach	96
4.4	Case Study : Gain Margin Calculations for the CIGRE-HVDC Bench- mark Model	97
4.4.1	Case 1: Finding the Maximum K_p for a Stable System	99
4.4.2	Case 2: The Impact of AC System Strength on the Stability	101
4.5	Conclusion	104
Chapter 5	Grid Interaction Studies Using Sequence Domain Impedance/Ad- mittance	105
5.1	Introduction	105
5.2	Stability Screening Using the Net Sequence Admittance	107
5.3	Case Study: CIGRE-HVDC Benchmark Model Stability Screening Us- ing the Net Sequence Admittance	114
5.3.1	Case 1: Stable Case ($K_p = 1.0 \text{ rad/p.u.}$)	115
5.3.2	Case 2: Unstable Case ($K_p = 3.0 \text{ rad/p.u.}$)	118
5.4	Stability Screening Using the Net Sequence Impedance	122

5.5	Case Study: CIGRE-HVDC Benchmark Model Stability Screening Using the Net Sequence Impedance	125
5.5.1	Case 1: Stable Case ($K_p = 1.0 \text{ rad/p.u.}$)	125
5.5.2	Case 2: Unstable Case ($K_p = 3.0 \text{ rad/p.u.}$)	128
5.6	Case Study: STATCOM Stability Screening Using the Net Sequence Impedance	131
5.7	Discussion	136
5.8	Conclusion	138
Chapter 6	Conclusion	139
6.1	Concluding Remarks and Discussion	139
6.2	Suggestions for Future Work	141
Appendix A	Relationship between positive and negative frequency components	143
Appendix B	Relationship between the sequence and DQ variables	144
Appendix C	Phase to sequence admittance transformation matrix	148
Bibliography		150

List of Figures

1.1	Stability analysis methods [24], [25]	4
1.2	(a) PES connected to grid, (b) Dividing the system into two independent subsystems and (c) The closed-loop transfer function.	11
2.1	Frequency scanning via (a) voltage injection and (b) current injection [27].	19
2.2	Multi-sine from 0.5 Hz to 300 Hz with $\delta_l = 0, \forall l$ (a) $a = 0.002kV$ and (b) $a = 0.02kV$. Note that $l_0 = 0.5, N = 300$ and $f_d = 0.5 Hz$ for both multi-sines.	23
2.3	Schroeder multi-sine from 0.5 Hz to 300 Hz with $\delta_l = -\frac{(l-l_0)(l-l_0+1)}{(N-l_0+1)}\pi, \forall l$ (a) $a = 0.002kV, \forall l$ and (b) $a = 0.02kV, \forall l$. Note that $l_0 = 0.5, N = 300$ and $f_d = 0.5 Hz$ for both multi-sines.	24
2.4	Multi-sine from 0.5 Hz to 300 Hz with $a = 0.02kV$, (a) $\delta'_l = 0, \forall l$ and (b) $\delta'_l = \frac{\pi}{180}n^2, \forall l$. Note that $l_0 = 0.5, N = 300$ and $f_d = 0.5 Hz$ for both multi-sines.	25
2.5	(a) Procedure of performing frequency scanning based on phase variables for a PES and (b) Transformation to frequency domain.	27
2.6	(a) Procedure of performing frequency scanning based on sequence variables for a PES and (b) Transformation to frequency domain.	30

2.7	The transmission network system under study (the single phase equivalent circuit).	33
2.8	Sequence-based frequency scanning of a transmission network.	34
2.9	(a) STATCOM model under study (the single phase equivalent circuit) and (b) Type-I controller.	35
2.10	Frequency scanning of a STATCOM operating with a Type-I controller using sequence variables.	36
2.11	The sequence frequency response of a STATCOM operating with a Type-I controller obtained from the phase frequency scanning.	37
2.12	Comparison between sequence and phase frequency scanning results from the STATCOM.	38
2.13	Coupling between the ac and dc sides of the system and frequency interference in the phase/sequence domains.	40
2.14	Positive sequence voltage injection and the resulting positive sequence current of a transmission line. No MFC is observed.	41
2.15	Positive sequence voltage injection and the resulting positive sequence current of a STATCOM. MFC is observed	42
2.16	The sequence-based frequency scanning of a STATCOM using two independent scans: 1) from $0.5Hz$ to $49.5Hz$ 2) from $50Hz$ to $400Hz$	45
2.17	(a) Procedure of performing DQ-based frequency scanning for a PES and (b) Transformation to frequency domain.	47
2.18	DQ-based frequency scanning of a transmission network	51

2.19 D and Q voltage injection and the resulting D and Q currents of a transmission line. No MFC is observed.	52
2.20 DQ-based frequency scanning of a STATCOM	53
2.21 D and Q voltage injection and the resulting D and Q currents of a STATCOM. No MFC is observed	54
2.22 Coupling between the ac and dc sides of the system and frequency interference in DQ domain.	55
2.23 Frequency shift between Sequence and DQ-based frequency scanning	59
2.24 Comparison between the positive sequence admittance obtained from Sequence and DQ-based frequency scanning	60
2.25 (a) Procedure of performing $\alpha\beta$ -based frequency scanning for a PES and (b) Transformation to frequency domain.	61
2.26 $\alpha\beta$ -based frequency scanning of a STATCOM	64
3.1 A PES connected to a grid and the independent models of the ac grid and PES.	67
3.2 Small signal current perturbation	68
3.3 The closed-loop model of the combined system using the small signal models of ac grid and PES models, when a current perturbation is applied.	68
3.4 The closed-loop model of the combined system using the inverse small signal models of the ac grid and PES, when a current perturbation is applied.	69
3.5 Small signal voltage perturbation	70

3.6	The closed-loop model of the combined system using the small signal models of ac grid and PES models, when a voltage perturbation is applied.	71
3.7	The closed-loop model of the combined system using the inverse small signal models of ac grid and PES models, when a voltage perturbation is applied.	71
3.8	The closed-loop transfer function of the overall system.	76
3.9	(a) CIGRE-HVDC benchmark model under study (the single phase equivalent circuit) and (b) α controller at the rectifier side and γ controller at the inverter side. Note that subscripts r and i represent the rectifier and the inverter, respectively.	81
3.10	Contour of $\Delta(j\omega)$ for the stable case.	82
3.11	Contours of a) $\lambda_1(j\omega)$ and b) $\lambda_2(j\omega)$ for the stable case.	83
3.12	Contour of $\Delta(j\omega)$ for the unstable case.	84
3.13	Contours of a) $\lambda_1(j\omega)$ and b) $\lambda_2(j\omega)$ for the unstable case.	85
3.14	The dc-link current response of the HVDC system.	86
3.15	Plots of $\lambda_1(j\omega)$ and $\lambda_2(j\omega)$ (for the CIGRE-HVDC system).	87
3.16	Plots of $\lambda_1(j\omega)$ and $\lambda_2(j\omega)$ when considering swapping.	89
4.1	The closed-loop model of a system.	92
4.2	The Nyquist plot of the closed-loop system under study for $K = 1.0$	93
4.3	The Nyquist plot of the closed-loop system under study for $K = 0.75$	95
4.4	The step response of the closed-loop system under study for $K = 0.75$ and $K = 0.85$	96

4.5	(a) CIGRE-HVDC benchmark model under study (the single phase equivalent circuit) and (b) α controller at the rectifier side and γ controller at the inverter side. Note that subscripts r and i represent the rectifier and the inverter, respectively.	98
4.6	The dc-link current response of the HVDC system.	99
4.7	The dc-link current response of the HVDC system (Zoomed in). . . .	100
4.8	Frequency of the points where the counter of one eigenlocus of the unstable case crosses the real axis.	100
4.9	One eigenlocus of the unstable case with the original ac grid.	101
4.10	One eigenlocus of the stabilized case with the modified ac grid.	103
4.11	The dc-link current response of the HVDC system with scaled ac grid. . . .	103
5.1	Derivation of the sequence model for the grid-connected PES.	107
5.2	The closed-loop transfer function of the overall system	111
5.3	CIGRE-HVDC benchmark model under study (the single phase equivalent circuit).	114
5.4	The real and imaginary parts of $Z_{grid_{pp}}^{-1}(j\omega) + Y_{PES_{pp}}(j\omega)$	116
5.5	The real and imaginary parts of $Z_{grid_{nn}}^{-1}(j\omega) + Y_{PES_{nn}}(j\omega)$ at $f = 111Hz$	117
5.6	The dc-link current response for the stable case.	118
5.7	The real and imaginary parts of $Z_{grid_{pp}}^{-1}(j\omega) + Y_{PES_{pp}}(j\omega)$	119
5.8	The real and imaginary parts of $Z_{grid_{nn}}^{-1}(j\omega) + Y_{PES_{nn}}(j\omega)$	120
5.9	The dc-link current response for the unstable case.	121
5.10	The closed-loop representation of the grid-connected PES using the inverse models.	122

5.11	The real and imaginary parts of $Z_{grid_{pp}}(j\omega) + Y_{PES_{pp}}^{-1}(j\omega)$	126
5.12	The real and imaginary parts of $Z_{grid_{nn}}(j\omega) + Y_{PES_{nn}}^{-1}(j\omega)$	127
5.13	The real and imaginary parts of $Z_{grid_{pp}}(j\omega) + Y_{PES_{pp}}^{-1}(j\omega)$	129
5.14	The real and imaginary parts of $Z_{grid_{nn}}(j\omega) + Y_{PES_{nn}}^{-1}(j\omega)$	130
5.15	(a) STATCOM model under study (the single phase equivalent circuit) and (b) Type-I controller.	132
5.16	The real and imaginary parts of $Z_{grid_{pp}}(j\omega) + Y_{PES_{pp}}^{-1}(j\omega)$	133
5.17	The real and imaginary parts of $Z_{grid_{nn}}(j\omega) + Y_{PES_{nn}}^{-1}(j\omega)$	134
5.18	The response of the line current of STATCOM for the stable case. . .	135
B.1	Transformation between different domains	144

List of Abbreviations

EMT	E lectro- M agnetic T ransient.
FACTS	F lexible a c T ransmission S ystems.
FFT	F ast F ourier T ransform.
GNC	G eneralized N yquist C riterion.
LCC	L ine C ommutated C onverter.
LHP	L eft H alf P lane.
LTI	L inear T ime- I nvariant.
MFC	M irror F requency C oupling.
MIMO	M ultiple I nput M ultiple O utput.
MMC	M odular M ultilevel C onverter.
MSD	M odified S equence D omain.
PES	P ower E lectronic S ystem.
RHP	R ight H alf P lane.
SCR	S hort C ircuit R atio.
SISO	S ingle I nput S ingle O utput.
SRF	S ynchronous R eference F rame.
SSCI	S ub S ynchronous C ontrol I nteractionl.

SSSC	Static Synchronous Series Compensator.
STATCOM	Static Synchronous Cmpensator.
SVC	Static Var Compensator.
TCSC	Thyristor Controlled Series Compensator.
VSC	Voltage Source Converter.

List of Symbols

δ_l	phase angle of a signal
θ	transformation angle
a	amplitude of a signal
f	frequency
f_0	fundamental frequency of a system
f_d	frequency interval between consecutive frequency components
t	time
$Y_{\alpha\beta 0}$	$\alpha\beta 0$ admittance of a system
Y_{abc}	three phase admittance matrix of a system
$Z_{\alpha\beta 0}$	$\alpha\beta 0$ impedance of a system
Z_{abc}	three phase impedance matrix of a system
Y_{DQ0}	DQ admittance of a system
Y_{PN0}	sequence admittance of a system
Z_{DQ0}	DQ impedance of a system
Z_{PN0}	sequence impedance matrix of a system
N	the number of net encirclement around $(-1, 0)$
P	the number of the poles of an open-loop system

Y_{PES}	admittance matrix of a system
Z	the number of RHP poles of a closed-loop system
Z_{grid}	impedance matrix of an ac system
GM	gain margin of a system

Acknowledgments

I would like to express my sincere gratitude to my advisor Prof. A. M. Gole for his continuous support during the course of my Master's Degree. It has been a great honour and a privilege to work under your supervision.

I wish to thank Dr. M. K. Das for mentoring me throughout the course of my program. Your support, insightful comments and knowledge has help me get to this point and finish this research.

I would also like to thank my parents and my brothers who have supported me in every possible way during my studies. This could not have been possible without their support.

Finally, I would like to give special thanks to my committee members for their support and wonderful advice, the staff at Faculty of Graduate Studies staff and the Department of Electrical and Computer Engineering, my lab-mates at the simulation laboratory, my friends at University of Manitoba, my friends in the city of Winnipeg and all the people who have supported me along the way.

This thesis is dedicated to my dear family.

Chapter 1

Introduction

1.1 Background

Power electronic systems (PESs) are indispensable parts of the modern power grids. PESs are being used in generation, transmission and distribution parts of the power system. Some examples of these PESs are:

1. Excitation systems in synchronous generators[1]
2. Variable frequency drives in power stations[1]
3. Static VAR Compensators (SVCs) [2]
4. HVDC systems [2]
5. Flexible AC Transmission Systems (FACTS) controllers [2]
6. Integration of renewable energies with power grids [3]–[5]
7. AC Micro-grids [6]

8. Electric Railway Systems [7]

PESs are widely used in modern power systems because of their useful characteristics, such as enhancing the efficiency and reliability of the power systems [8]. The vast use of these PESs has introduced several problems:

1. PESs use power semiconductor switches operating at high switching frequencies. The switching actions of these power switches generate harmonics at the terminal voltage and current signals of the PESs. A high level of harmonic distortion has numerous negative effects on the system, such as [9]–[12]:
 - (a) Reducing the power quality of the system
 - (b) Generating heat, which leads to problems in other electronic devices such as transformers, capacitor banks, etc
 - (c) Disrupting the nearby communication lines
 - (d) Causing oscillations within the system, which can result in a system's instability
2. The wide-band fast controllers of the PESs can lead to problems such as harmonic magnification [13], torsional instabilities [14] and network-controller mode instabilities [15].

Therefore, the power semiconductor switches and the wide-band fast controllers used in the PESs can cause adverse interaction between the following elements in a power system and can lead to small-signal instability of the overall system [8], [16].

1. The grid and the PESs

2. Several cascaded PESs
3. The PESs with other passive elements in the system

The small-signal instability can be detected in several forms such as:

1. Wide-band oscillations [17]
2. Harmonic instability and resonance issues [18]

Analyzing the adverse interactions and taking necessary precautionary measures, such as proper controller design [19], [20], is required to avoid such interactions in grid-connected PESs [21], [22]. The rest of this chapter is focused on the stability analysis of the grid-connected PESs.

1.2 Stability Analysis of the Interactions in grid-connected PESs

The stability of the interactions between a PES and a grid can be studied using techniques such as time-domain transient simulations including electromagnetic transient (EMT) simulation or analytical approaches, as illustrated in Figure 1.1 [23]. Using multiple EMT simulations, requires modeling the system, including their controllers, in the simulation software. One drawback of using such simulations is that any changes in the parameters of the system, such as a change in the operating point, requires an updated simulation. Hence, making the simulations case-specific. Accordingly, a large number of simulations may be needed for a thorough understand-

ing of the different scenarios in a system, which makes this approach time-consuming.

Analytical modellings have been developed to address these issues. [20].

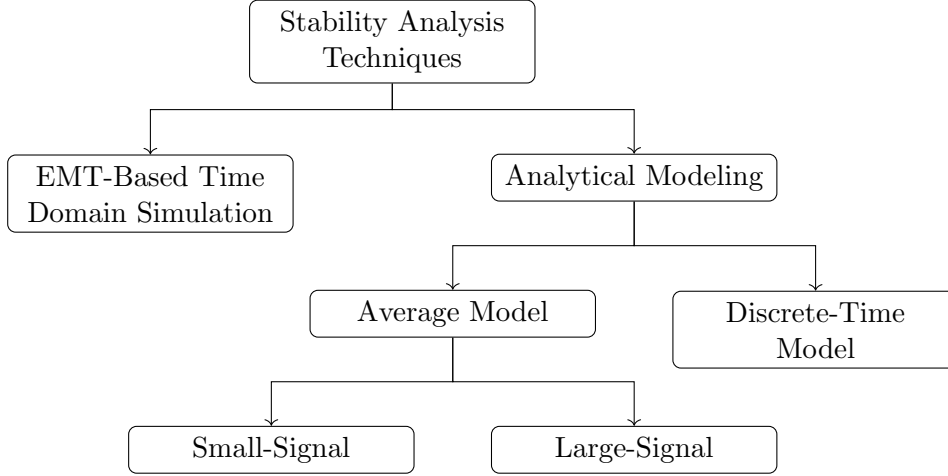


Figure 1.1: Stability analysis methods [24], [25]

1.3 Small-Signal Stability Analysis Techniques

Modern PESs often use power semiconductor devices, which makes such systems non-linear and time-variant. Analytical models apply different techniques to make PESs Linear Time-Invariant (LTI) systems.

Some methods for making a PES a time-invariant system include averaging techniques and discrete-time modelling. Since the discrete-time modelling requires complex computation during implementation, average modelling techniques are mostly preferred in larger networks [24]. Next, different linearization techniques can be applied to obtain a linear model of the system. One common technique is linearizing the system around one operation point, using small perturbations.

1.3.1 State-Space Based Stability Analysis

State-space based analysis determines the stability of the overall system by studying the different oscillation modes. The stability of each mode can then be decided using eigenvalues, which can be calculated from the full system state-space equations [26]. In this method, the state-space equations of the system are calculated and used for studying the interactions in detail. The detailed information of each component in the system is required for calculating these equations. Therefore, the state-space equations provide detailed information about a system's behaviours.

However, establishing the state-space equations may not always be possible for some systems. Some manufacturers provide black-box models, compiled into non-readable compiled code for the EMT simulator, where not enough information is at hand for obtaining the details of these models.

Even with no black-boxes in the system, the state-space equations usually require long and tedious calculations due to the complex controllers used in modern power systems [27]. Note that these controllers are not standardized, and the state-space equations which are case-specific need to be recalculated when one or more parameters of the system are changed.

Consequently, in systems with black-boxes or when obtaining the state-space equations is not feasible, the impedance-based approach can be used instead.

1.3.2 Impedance-Based Stability Analysis

The impedance-based analysis is a method for determining the stability of the grid-connected PESs [28]–[30]. In this method, the overall system is first divided

into a source and a load subsystem using Thevenin/Norton equivalent [31], [32]. The impedance/admittance of the two subsystems can then be obtained using various techniques known as the *impedance extraction techniques* to study the stability of the interactions between the two subsystems.

It is important to note that in this method, the detailed information of the subsystems is not required. Consequently, this method is preferred when dealing with black-box models in a system [32]. The problem with using the impedance-based approach is that the model of most PESs is not LTI when using the phase variables in the time domain. In such circumstances, the impedance extraction techniques which can only be used for LTI systems cannot be applied.

The advantages of impedance-based stability analysis include [30], [33]:

- Obtaining the stability of the systems containing black-box models is possible since the impedance can be calculated.
- Dealing with complex systems that are continuously changing is less complicated. Changes in the system can happen by adding/removing the units or changing the operating point. These changes can be reflected in the impedance and therefore making the stability analysis straightforward.
- Changing the load and source impedance can be a possible solution to solve the instability issues of the overall system.

1.4 Impedance-Based Approach: Impedance Extraction Techniques

The impedance-based stability analysis is a useful tool for accessing and screening the stability of PES-grid interactions [28], [30], [34]. In this technique, the overall PES-grid is divided into two subsystems, e.g. the source and load subsystems. By obtaining the frequency response of each subsystem, stability criteria, e.g. GNC, will be applied to the closed-loop system of the PES-grid for analyzing the stability of the interactions [16]. The impedance/admittance seen from the output of the ac grid and the admittance/impedance seen at the input of the PES, determine the closed-loop transfer function of the overall system. The stability of the PES-grid interactions can be obtained by applying the GNC to this closed-loop transfer function [29], [35], [36].

Since the impedance-based approach obtains the small-signal stability at the point of the interface using the impedance of the subsystems, the impedance modeling of the PES and the ac grid is thus required for stability analysis of the PES-grid interactions.

The impedance modeling methods can be categorized into two main groups:

1. **Shunt Current and Series Voltage Injections:** These methods are based on superimposing a series voltage and shunt current injection signals on the source and load subsystems, respectively. The impedance/admittance of the system is calculated using the voltage and current signals at the point of the injection.

2. **Harmonic Linearization:** In this method, a small-signal model of the system is extracted by injecting a signal containing one or more specific harmonics. The impedance of the resulting LTI system is then calculated by monitoring the response of the system [37].

Some other impedance extraction methods include:

1. Bifurcation [38]
2. Binary Sequence Injection [39]
3. Chirp Signal Injection [40]
4. Impulse Response [41]
5. Kalman Filtering [42]
6. Recurrent Neural Networks [43]

1.5 Impedance Extraction Using Shunt Current and Series Voltage Injections

Several models have been developed to extract the impedance/admittance of the ac grid and the PESs. Some of these models are:

1. Sequence models [44]: Using sequence variables, the three-phase balanced system can be modeled as two decoupled systems, one in the positive sequence and the other one in the negative sequence.

2. DQ models [8], [27], [30], [45]: For a symmetric three-phase ac system operating at balanced condition and by neglecting the switching harmonics, dc equilibrium operating points can be defined by transforming the system into a rotating DQ reference frame [8], [30], [45]. This accounts for time continuity (i.e. time-invariance) of the ac variables, since the ac variables in the time domain can be represented by dc quantities in the DQ frame [30], [45]. The non-linearity of the system can then be addressed by linearization around the operating point. This allows for the stability analysis of the resulting LTI system using small-signal analysis techniques [30].

1.6 Problem definition

Extracting an accurate analytical model for the PESs is not always an easy task due to the following reasons [27]:

1. Control systems schematics of the PESs can be case-specific as standard models do not yet exist. Therefore any proposed accurate analytical model of a PES may not be accurate enough for another PES.
2. The complexity of today's PESs causes more difficulties in accurately modeling such devices. In addition, presence of thyristors in the power electronic converters can complicate the modeling of the switching actions, since the turn off state of the thyristors depends on the current flowing through them.
3. The accurate and/or detailed information of black-box models are not available which in turn result in more problems regarding the development of analytical

models.

4. Extracting the analytical models of the PESs usually requires several assumptions for further simplification of the system. Therefore, even if the detailed accurate information of the PESs exists, such approximations usually limits the accuracy of the developed models.

Frequency scanning is an alternative solution where a time-domain simulation program is used. In this technique, numerical methods are applied to obtain the small-signal frequency response of a system [46].

1.7 Frequency Scanning

Frequency scanning technique is a useful tool for stability screening of grid-connected PESs or parallel-connected PESs [27]. A frequency scan has the information of the nodal frequency response since the impedance of the system is calculated at each frequency of the desired frequency range [47]. In this method, the system is divided into two subsystems, where the interaction between these subsystems is modeled as a closed-loop feedback system [31], [33]. The independent model of each subsystem is required as shown in Figure 1.2. The stability of the interactions between the subsystems can then be studied by applying a stability criterion, such as GNC.

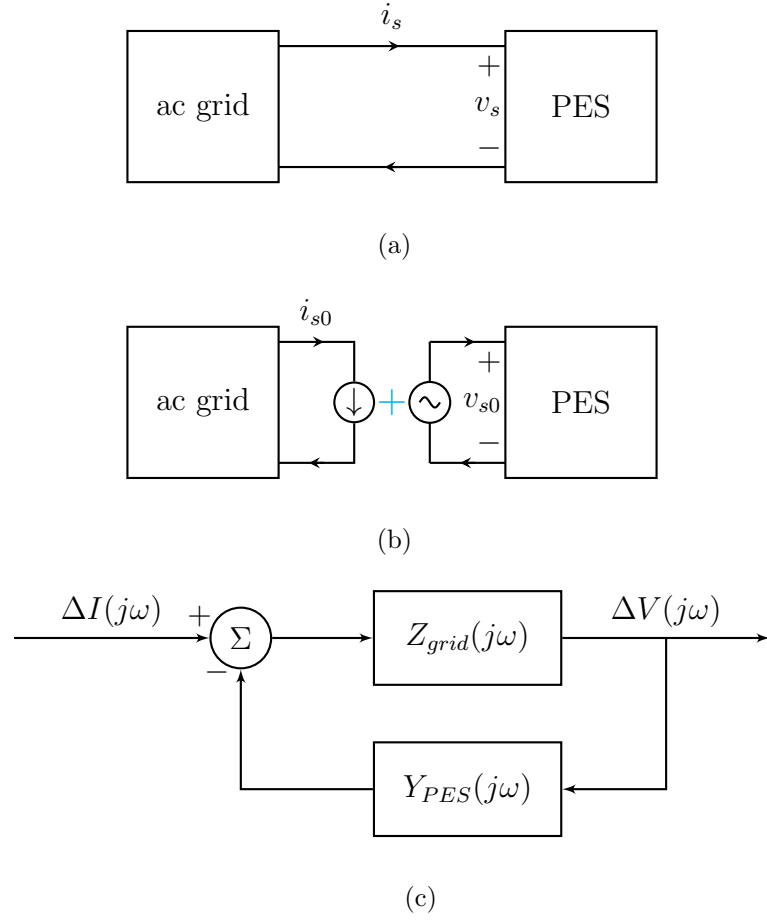


Figure 1.2: (a) PES connected to grid, (b) Dividing the system into two independent subsystems and (c) The closed-loop transfer function.

1.8 Literature Review on Frequency Scanning and Stability Analysis

Frequency scanning is a precise method of obtaining the impedance/admittance of the source and load subsystem [34]. The frequency scanning technique was first presented in [46]. Many publications are focused on the simulation-based frequency scanning of the PESs:

1. In [48], a frequency dependent model for an LCC-HVDC converter is proposed. The frequency scan obtained by EMT simulation illustrates a great match with analytical model. The Stability of the overall system is analyzed using the GNC.
2. In [49], the Sub-Synchronous Control Interaction (SSCI) of a Line Commutated Converter (LCC) connected to a series compensated ac system is studied. The system is divided into two subsystems of the LCC plus ac filters and the ac system. The frequency response of each subsystem is first obtained by a frequency scanning and the GNC is applied for studying the stability of the sub-synchronous control interactions.
3. In [50], four methods for analyzing the small-signal stability of a grid inverter system are presented. The frequency scanning results are compared with analytical modeling and frequency analysis simulator results. It is shown that, the results from these methods are consistent.
4. In [51], the sequence impedance model of the single-phase converters is obtained using harmonic linearization technique. It is shown that the frequency

scan results for the input impedance of a single phase rectifier agrees with the theoretical modeling impedance. The Stability of the overall system is observed using the GNC.

5. In [45], The stability analysis of a power system containing several a Static Synchronous Compensator (STATCOM) systems in proximity is presented. The DQ-based impedance of a STATCOM is obtained an GNC is applied to study the stability of the overall system. Authors show accurate results in terms of anticipating the stability of the interactions between the STATCOMs.
6. The frequency scanning of a grid-connected inverter system is presented in [52]. Simulation and experimental results are presented for the stability analysis of the overall system. It is shown that the the frequency scanning results can be used to accurately predict the stability of the inverter system.
7. In [34], the stability of the interactions in a grid-connected Voltage Source Converter (VSC) system is presented. The frequency scanning technique is used to obtain the DQ impedance of the VSC. It is illustrated that the results from frequency scanning match with the ones from analytical modeling.
8. In [53], the stability of the interactions between a STATCOM and its ac grid is presented. In this study, the frequency response of the STATCOM and ac grid are obtained using the frequency scanning techniques and the GNC is applied to predict the stability of the interactions.
9. In [54], the stability of ac systems with constant power loads is studied. The DQ impedance of the voltage source inverter and converters are obtained and

the GNC is applied to study the stability of the interactions.

10. In [55], the frequency scanning technique is applied to two modular multilevel converters (MMC) in a back-to-back configuration for further stability analysis of the interactions. In this study the frequency scanning is performed via a voltage perturbation for one MMC and a current perturbation for the other MMC. Two cases are studied, where a weak ac grid and a strong ac grid lead to instability and stability of the overall system, respectively.
11. In [56], the frequency scanning of an HVDC system is obtained and used for screening the adverse interactions between the grid and the HVDC converter. It is shown that the frequency scanning method can be used for controller optimization.
12. In [57], the sequence admittance model of a STATCOM is obtained by analytical calculations and frequency scanning. It is shown that the frequency scanning results match with the analytical calculations.

1.8.1 Research Gaps

Although several studies on predicting the small signal stability of the grid-connected PESs exists in literature, there is not enough discussions on how to perform frequency scanning in different domains. Moreover, the relationship between the different domains needs further exploring and explaining in details. In addition, the frequency scanning results can predict the stability of the interactions using different methods. These methods need to be discussed more in details and the advantages and disadvantages of each method can be of one's interest.

1.8.2 Thesis Objectives

The main objectives of this thesis are:

1. Performing the frequency scanning techniques in different domains and using different variables.
2. Studying the relationship between the different domains and transformation between the domains.
3. Analyzing the stability of the interactions in a grid-connected PES using the frequency scanning results.
4. Using the eigenlocus stability approach for gain margin calculation and stabilizing the interactions by increasing the strength of the ac system.
5. Discussing approximate stability screening technique based on the positive and negative sequence impedance/admittance as an approach for stability screening.

1.9 Thesis Organization

An overview of the next chapters are as follows:

1. In chapter 2, the frequency scanning techniques in different domains and using different variables are presented. Case studies are provided to compare the results in each domain. Moreover, the relationship between the different variables is presented and the transformation matrices between the domains are derived. This chapter also, looks into the problem of frequency interference and how this problem is solved.
2. In chapter 3, the stability of the interactions in a grid-connected PES is studied using the results from frequency scanning. The generalized Nyquist criterion, the stability analysis with individual eigen-loci and generalized inverse Nyquist criterion are presented as methods for screening the stability of the interactions. Case studies are provided to validate the results from each stability criteria.
3. In chapter 4, some applications of frequency scanning techniques are presented and followed by case studies.
4. In chapter 5, an approximate stability screening method is presented and compared with the results obtained from generalized Nyquist criterion. Case studies are provided to verify the results of this method.
5. In chapter 6, the main conclusions of this work are presented and followed by some suggestion of future work.

Chapter 2

Frequency Scanning Techniques

2.1 Introduction

The small-signal stability of the grid-connected the power electronic systems (PESs) is becoming more important since PESs are being increasingly used in modern power systems. small-signal stability analysis is usually performed using an EMT-based time-domain simulation [24], [27], [46], [58] or analytical modeling [24], [27], [58].

Using an EMT-based time-domain simulation to study the behaviour of PESs is advantageous since detailed modeling of the system in EMT simulation is possible. Because such simulation can be time-consuming, analytical modeling techniques such as small-signal methods have been developed. Small-signal methods can be divided into two different groups: 1) State-space based analysis and 2) Impedance-based analysis. Note that, since obtaining an accurate analytical model of PESs is not always possible, frequency scanning techniques can be used instead to obtain the frequency response of the PESs and analyze the stability of the interaction.

Frequency scanning technique can be used to numerically obtain the frequency response of a system using an EMT simulation program. This technique is done by injecting a wide-band small-amplitude voltage/current signal into the simulation model of the system in the time domain. In this technique, the overall system is divided into the source and load subsystems, where each independent subsystem must be stable before the frequency scan. In this chapter, the frequency scanning technique is discussed in detail.

2.2 Frequency Scanning of PESs

An EMT simulation program is used for modeling the combined and individual systems. Next, the operation point is set by the main source of the system, and the system can then be linearized around the operating point using frequency scanning technique: After the system reaches a steady-state stage, a voltage/current signal which has a small magnitude is injected at the input of the PES in the time-domain simulation model. The voltage/current signal injection can be modeled as a new source and in series/parallel with the main source based on the superposition rule [16].

The signal injection procedure is illustrated in Figure 2.1. The admittance of a PES can be obtained by the shunt voltage injection illustrated in Figure 2.1(a). This admittance is defined by $Y_{PES}(j\omega) = \frac{\Delta I(j\omega)}{\Delta V_0(j\omega)}$, where $\Delta V_0(j\omega)$ and $\Delta I(j\omega)$ are obtained by applying Fast Fourier Transform (FFT) to the voltage injection ($\Delta v_0(t)$) and the resulted current change ($\Delta i(t)$), respectively.

The impedance of a PES can be obtained by the series current injection illustrated

in Figure 2.1(b). This impedance is defined by $Z_{PES}(j\omega) = \frac{\Delta V(j\omega)}{\Delta I_0(j\omega)}$, where $\Delta I_0(j\omega)$ and $\Delta V(j\omega)$ are obtained by applying FFT to the current injection ($\Delta i_0(t)$) and the resulted voltage change ($\Delta v(t)$) respectively.

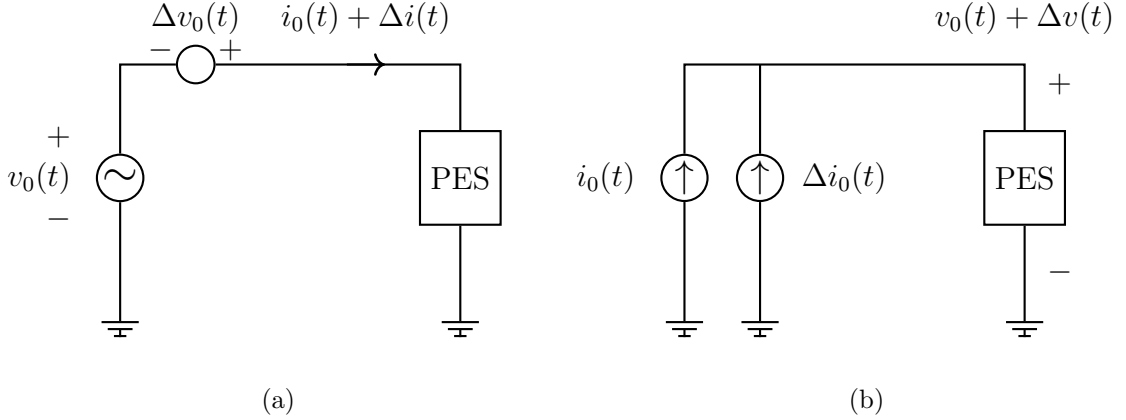


Figure 2.1: Frequency scanning via (a) voltage injection and (b) current injection [27].

Consider the admittance scan, where the voltage multi-tone signal¹ is applied at the input and the current is measured. The FFT of the current signal is a smooth function of frequency and directly proportional to the admittance, i.e. $I(j\omega) = a \times Y(j\omega)$. If a sufficiently small frequency increment f_d is used, the resulting graph for $Y(j\omega)$ can be directly used for further processing without any additional interpolation or curve fitting.

Frequency scanning techniques can be used to extract the frequency response of the PES. The small-amplitude signal injection accounts for the linearity of the extracted model. The choice of injection variables, along with the system model, determines the time-invariability. These matters are thoroughly discussed in the following sections.

¹The multi-tone signal is discussed in Section 2.3.2

2.3 Voltage Injection Versus Current Injection

Either voltage or current injection can be used for the determination of the frequency response of the network or PES. However, sometimes one is more convenient than the other. Normally for shunt connected devices such as STATCOMs, SVCs and HVDCs we use voltage, and for series connected devices such as TCSCs and SSSCs we use current. Regardless, in order to obtain the frequency scan by simulation, the subsystem whose scan is being obtained must have a stable simulation.

2.3.1 Single-Tone Injection

In this approach, the system is perturbed by a single frequency signal each time. The response of the system is captured to obtain the impedance at the injection frequency. This procedure is repeated until all the frequencies of the desired range are injected [23], [27]. Since one signal is injected at a time, the maximum amplitude of the injection signal can be relatively larger. The drawback of this method is that since in each simulation run, the system needs to reach the steady-state before the frequency response can be captured, the single-frequency injection can be time-consuming. A multi-tone signal injection is an alternative solution.

2.3.2 Multi-Tone Injection

In an LTI system, the superposition rule is always obeyed and, therefore, a wide-band signal can be superimposed on the system. In the multi-tone injection approach, the system is perturbed by a wide-band signal with a small amplitude in the desired frequency range for obtaining the frequency response of the system [23], [27], [46]. Some examples of wide-band signals are discussed in [59]. Multi-tone signal injection is a time-saving method. However, since a wide-band signal is injected at a time, the maximum amplitude of the injection signal should be relatively smaller in this method.

It is difficult to obtain impedance or admittance frequency response results experimentally, because of the difficulty of generating the multi-tone signal in the laboratory, and the resulting noise in the measurements. Even though the simulation model may not represent the real world PES precisely, the waveforms obtained are clean and allow a better determination of the impedance or admittance frequency response.

The general form of a *multi-sine* signal is illustrated in Equation 2.1 and can be used as a wide-band signal.

$$u_1(t) = a \sum_{l=l_0}^N \sin(2\pi f_d l t + \delta_l) \quad (2.1)$$

Where 'a' is the amplitude of the multi-sine. The amplitude of the resultant multi-sine signal is limited with a proper choice of δ_l , whereas setting $\delta_l = 0$ results in voltage (or current spikes). Note that f_d is the frequency interval between each two consecutive frequency components since each component of the multi-sine has a frequency, which is a multiplication of f_d . This means that f_d is the parameter for changing the scan resolution. Moreover, it can be concluded that the multi-sine $u_1(t)$ is a periodic signal

with a time period of $t_d = \frac{1}{f_d}$ [16].

The Simplest form of a multi-sine can be obtained by considering $\delta_l = 0$. A small magnitude for multi-sine is suitable since it allows for the linearization of the system around the operation point. However, a small magnitude multi-sine signal can result in a small signal to noise ratio, because the natural response of the system cannot reach zero in a finite time simulation run. Therefore, in some cases, when a multi-sine disturbance is injected, the natural response of the system can become comparable to the steady-state response of the system. This small signal to noise ratio can lead to a distorted frequency scanning result, hence decreasing the accuracy of the frequency scan and inaccurate results [27]. Although increasing the simulation time, can lower the natural response of the system, it can be significantly time-consuming for large/complex systems.

A multi-sine signal with a larger magnitude can be used instead to address this issue. However, such multi-sine has larger spikes, which may disturb the current operation point of the system or even lead to a change in the operation point [27]. In such circumstances, a linearized model of the system cannot be obtained. As a result, there is a trade-off between the accuracy of the frequency scanning, the duration of the simulation run and the magnitude of the multi-sine [27].

A multi-sine with $\delta_l = 0$ and $a = 0.002kV$ is illustrated in Figure 2.2(a). From the figure, it can be seen that this multi-sine is not uniform, and the value of the signal is very small compared to noise, and therefore, signal to noise ratio is small. If the magnitude of the multi-sine is ten times larger ($a = 0.02kV$) as illustrated in Figure 2.2(b), the signal is still very small and comparable to noise. Moreover, this

new signal has spikes that are ten times larger, and such large spikes may disturb the operation point of the system.

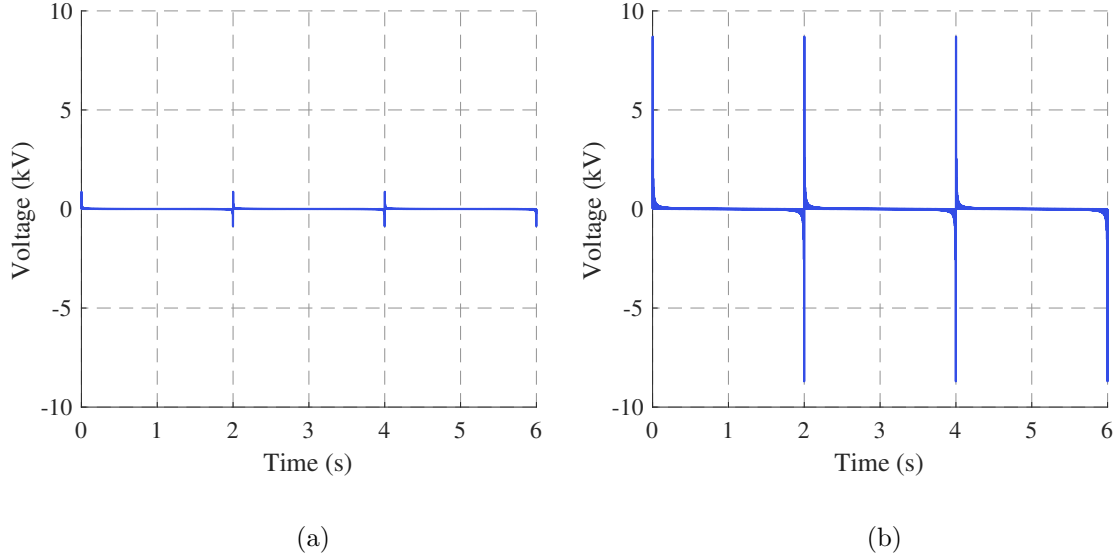


Figure 2.2: Multi-sine from 0.5 Hz to 300 Hz with $\delta_l = 0, \forall l$ (a) $a = 0.002\text{ kV}$ and (b) $a = 0.02\text{ kV}$. Note that $l_0 = 0.5$, $N = 300$ and $f_d = 0.5\text{ Hz}$ for both multi-sines.

A Schroeder multi-sine can be used with the phase angle δ_l defined as [59], to make sure that the magnitude of the multi-sine is small:

$$\delta_l = -\frac{(l - l_0)(l - l_0 + 1)}{(N - l_0 + 1)}\pi \quad (2.2)$$

A Schroeder multi-sine with δ_l as shown in Equation 2.2 and $a = 0.002\text{ kV}$ is illustrated in Figure 2.3(a). The Schroeder has a more uniform shape compared to the multi-sine $u_1(t)$ with $\delta_l = 0$. Even if a larger magnitude multi-sine is chosen ($a = 0.02\text{ kV}$), the overall shape of the Schroeder multi-sine remains uniform as illustrated in Figure 2.3(b). Therefore, the value of δ_l can make a significant difference in the overall shape of the multi-sine.

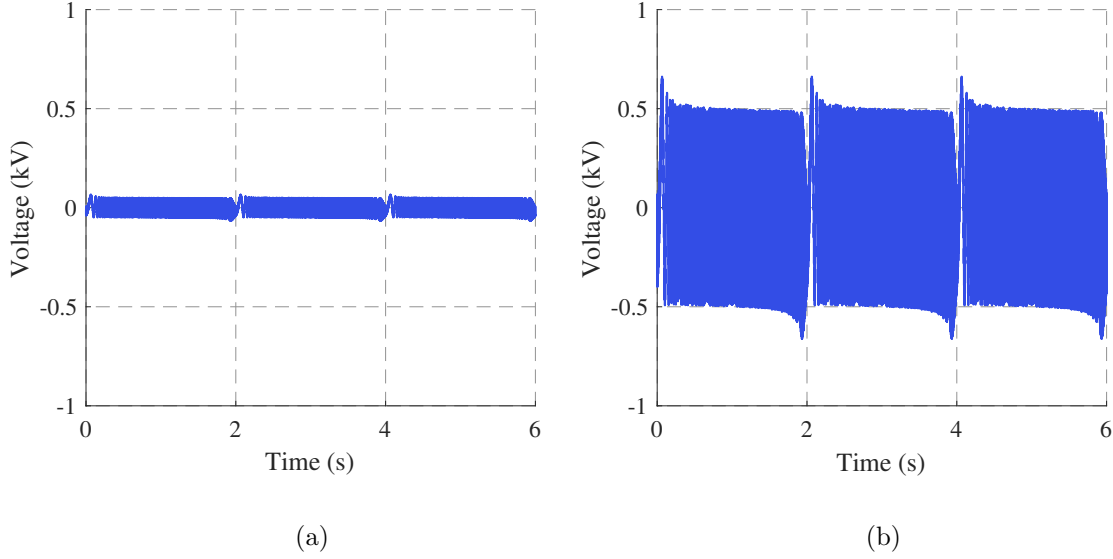


Figure 2.3: Schroeder multi-sine from 0.5 Hz to 300 Hz with $\delta_l = -\frac{(l-l_0)(l-l_0+1)}{(N-l_0+1)}\pi$, $\forall l$ (a) $a = 0.002\text{ kV}$, $\forall l$ and (b) $a = 0.02\text{ kV}$, $\forall l$. Note that $l_0 = 0.5$, $N = 300$ and $f_d = 0.5\text{ Hz}$ for both multi-sines.

The multi-sine $u_1(t)$ with $\delta_l = 0$ has a smaller amplitude everywhere except for large spikes at discrete instances. As discussed before, this can be problematic for frequency scanning purposes. The Schroeder multi-sine has a more uniform waveform with maximum magnitudes, which are about ten times smaller than the magnitudes of the multi-sine $u_1(t)$ with $\delta_l = 0$. Therefore, the Schroeder multi-sine is more suitable for small-magnitude signal injection.

Another multi-sine signal which is shown in Equation 2.3 is used in [46] for frequency scanning.

$$u_2(t) = a \sum_{l=l_0}^N \sin(2\pi f_d t + \delta'_l) \quad (2.3)$$

Similarly, 'a' is the amplitude of the multi-sine, and the amplitude of the resultant signal is limited with a proper choice of δ_l , whereas setting δ_l results in voltage (or current spikes). The frequency gap between each two frequency components is defined

by f_d which means that f_d is the parameter for changing the scan resolution of the frequency scanning. Again, the multi-sine $u_2(t)$ is a periodic signal with a time period of $t_d = \frac{1}{f_d}$. The phase angle δ'_l is defined as [46]:

$$\delta'_l = \frac{\pi}{180} l^2 \quad (2.4)$$

A multi-sine with $\delta'_l = 0$ and $a = 0.02kV$ is illustrated in Figure 2.4(a). From the figure, it can be observed that this multi-sine has a small value everywhere except for certain times when a large spike occurs. This means that most of the energy of this signal exists in a large spike and at a short duration. As explained before, such large spikes may lead to a change in the operation point. Therefore the phase angle δ'_l shown in Equation 2.4(b) is introduced to determine the magnitude of each component in the signal and distribute the energy of the large spike, thus the multi-sine signal more uniform.

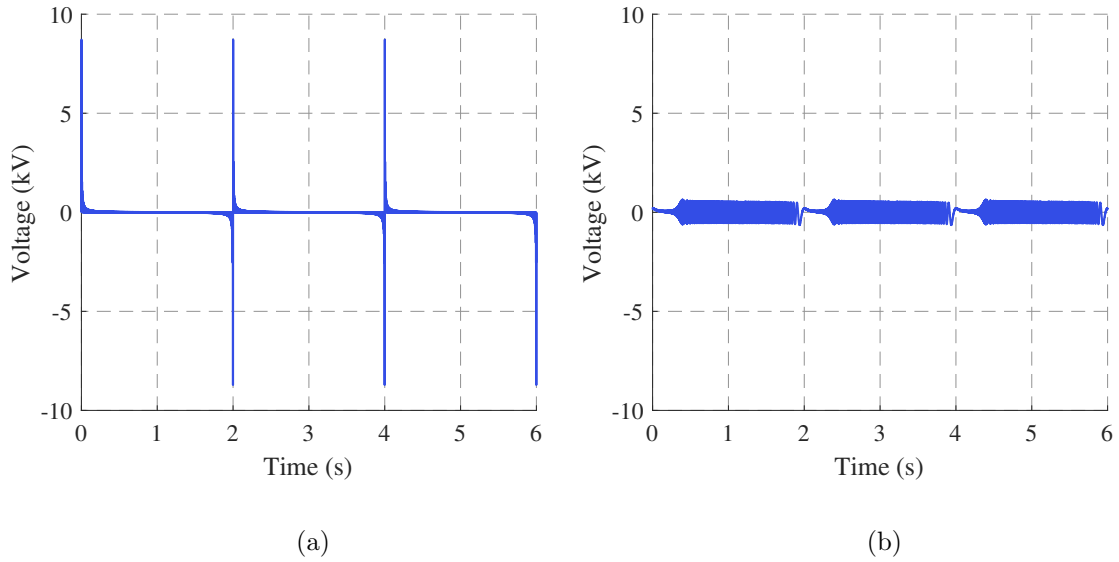


Figure 2.4: Multi-sine from 0.5 Hz to 300 Hz with $a = 0.02kV$, (a) $\delta'_l = 0, \forall l$ and (b) $\delta'_l = \frac{\pi}{180} n^2, \forall l$. Note that $l_0 = 0.5$, $N = 300$ and $f_d = 0.5\text{ Hz}$ for both multi-sines.

Both multi-sines $u_1(t)$ and $u_2(t)$ have uniform wave-forms when δ_l and δ'_l are not set to zero. This makes such multi-sines suitable for frequency scanning purposes. In this thesis, the Schroeder multi-sine is used for signal injection in all frequency scanning studies.

2.4 Selecting an Injection Domain

The choice of the injection domain can play an important role in whether or not a time-invariant model of the system can be extracted. The signal injection can be done in different domains such as:

1. Phase/Sequence Domain
2. DQ Domain
3. $\alpha\beta$ Domain

It is important to highlight that all of these domains are equivalents of one another. Therefore, the variables in each domain can be transformed into other domains using a specific transformation matrix.

The frequency scanning is done by injecting a multi-sine signal into the system in any domain. However, the scan results can be accurate or not based on whether the system can be modeled as an LTI system in that specific domain. In the following sections, the frequency scanning in each domain is presented with some examples, and the advantages/disadvantages of using each domain are discussed.

2.5 Frequency Scanning Using Phase Variables

The procedure of performing frequency scanning using the phase variables is illustrated in Figure 2.5. The multi-sine signal is injected in the a , b and c channels separately via 3 independent simulation runs. The voltages and currents of the three-phase system are captured at the point of injection for the duration of the simulation run. These signals are then transformed into the frequency domain using anti-aliasing filter, down sampling and FFT. The frequency-domain signals are then ready for calculating the impedance/admittance matrix of the PES ($Y_{abc}(j\omega)$) which is shown in Equation 2.5.

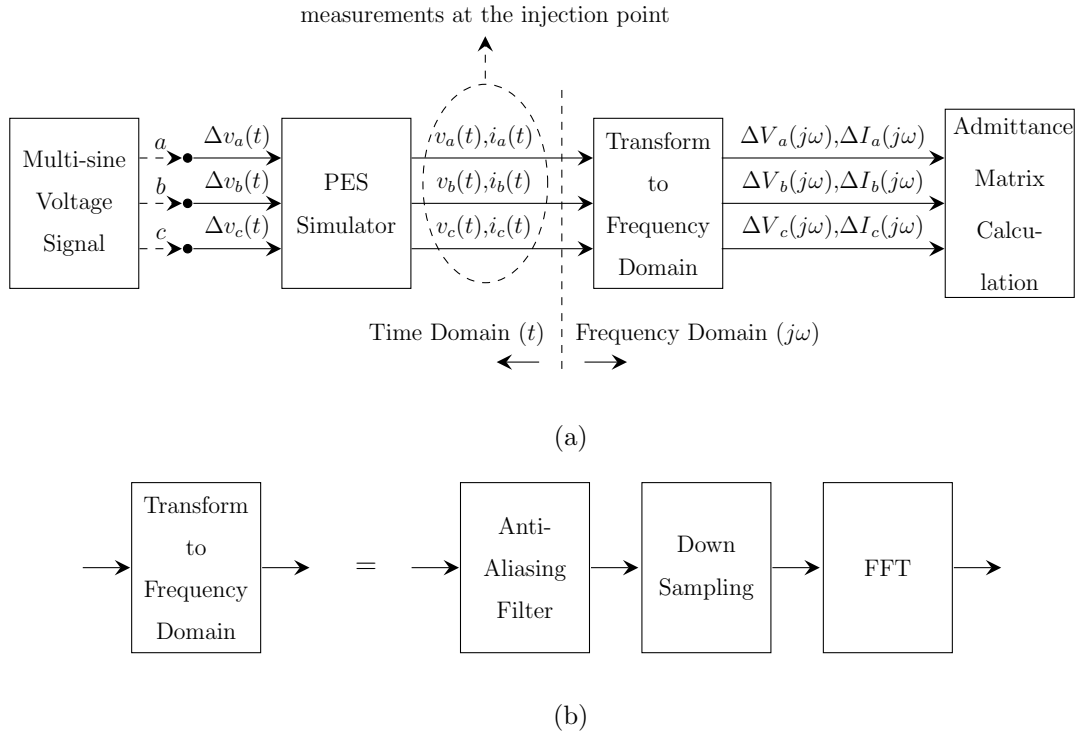


Figure 2.5: (a) Procedure of performing frequency scanning based on phase variables for a PES and (b) Transformation to frequency domain.

Note that the procedure of multi-sine voltage injection illustrated in Figure 2.5, extracts the admittance of the system. If the impedance of the system is desired, a multi-sine current injection can be used instead.

$$\begin{aligned}
 Z_{abc}(j\omega) &= \begin{bmatrix} Z_{aa}(j\omega) & Z_{ab}(j\omega) & Z_{ac}(j\omega) \\ Z_{ba}(j\omega) & Z_{bb}(j\omega) & Z_{bc}(j\omega) \\ Z_{ca}(j\omega) & Z_{cb}(j\omega) & Z_{cc}(j\omega) \end{bmatrix} \\
 Y_{abc}(j\omega) &= \begin{bmatrix} Y_{aa}(j\omega) & Y_{ab}(j\omega) & Y_{ac}(j\omega) \\ Y_{ba}(j\omega) & Y_{bb}(j\omega) & Y_{bc}(j\omega) \\ Y_{ca}(j\omega) & Y_{cb}(j\omega) & Y_{cc}(j\omega) \end{bmatrix}
 \end{aligned} \tag{2.5}$$

It is important to highlight that when transforming to the frequency domain, the steady-state values of each signal are subtracted. Therefore, the admittance is defined by the ratio of the injected current to the resulting change in the voltage ($\Delta I/\Delta V$). When injecting in one channel, other channels are set to zero. Therefore, by injecting in channel a , the first column of Y_{abc} can be calculated from the captured signals as illustrated below:

$$\begin{aligned}
 Y_{aa}(j\omega) &= \Delta I_a(j\omega)/\Delta V_a(j\omega) \\
 Y_{ba}(j\omega) &= \Delta I_b(j\omega)/\Delta V_a(j\omega) \\
 Y_{ca}(j\omega) &= \Delta I_c(j\omega)/\Delta V_a(j\omega)
 \end{aligned} \tag{2.6}$$

Other elements of $Y_{abc}(j\omega)$ are calculated similarly by injecting into channels b and c :

$$\begin{aligned}
 Y_{ab}(j\omega) &= \Delta I_a(j\omega)/\Delta V_b(j\omega) \\
 Y_{bb}(j\omega) &= \Delta I_b(j\omega)/\Delta V_b(j\omega) \\
 Y_{cb}(j\omega) &= \Delta I_c(j\omega)/\Delta V_b(j\omega)
 \end{aligned} \tag{2.7}$$

$$\begin{aligned}
Y_{ac}(j\omega) &= \Delta I_a(j\omega) / \Delta V_c(j\omega) \\
Y_{bc}(j\omega) &= \Delta I_b(j\omega) / \Delta V_c(j\omega) \\
Y_{cc}(j\omega) &= \Delta I_c(j\omega) / \Delta V_c(j\omega)
\end{aligned} \tag{2.8}$$

2.6 Frequency Scanning Using Sequence Variables

The sequence domain, which is also known as the symmetric component domain [60], can be used for frequency scanning applications. The procedure of sequence based frequency scanning is illustrated in Figure 2.6.

The multi-sine signal is injected with a positive, a negative and a zero sequence separately via 3 independent simulation runs. Because the simulators use phase variables, a sequence to phase transformation, as shown in Equation 2.9, is required to convert the sequence-based multi-sine signal to a three-phase signal. The resulting three-phase signal is then ready for injection to the system. The voltages and currents of the three-phase system are captured at the point of injection for the duration of the simulation run. These signals are then transformed into the frequency domain using anti-aliasing filter, down sampling and FFT.

The impedance/admittance matrix of the PES ($Y_{PN0}(j\omega)$) which is a 3×3 matrix is shown in Equation 2.10. The zero sequence can be neglected if the system configuration makes it impossible for it to flow, e.g., if there is a Δ -connected transformer winding or an ungrounded Y transformer winding. This is usually the case in most PESs. In such circumstances the impedance/admittance matrix of the PES ($Y_{PN}(j\omega)$) will be a 2×2 matrix. Note that the procedure of multi-sine voltage injection illustrated in Figure 2.6, extracts the admittance of the system. If the impedance

of the system is desired, a multi-sine current injection can be used instead.

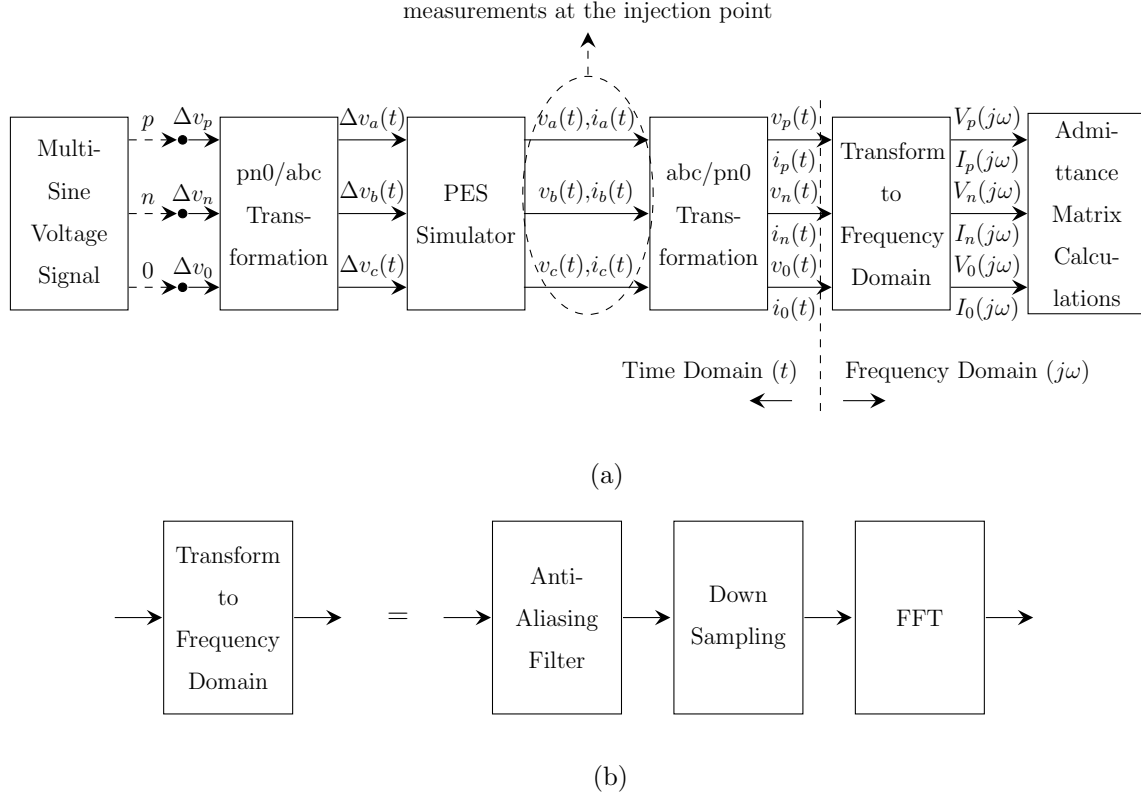


Figure 2.6: (a) Procedure of performing frequency scanning based on sequence variables for a PES and (b) Transformation to frequency domain.

$$\begin{aligned}
 \begin{bmatrix} x_a(j\omega) \\ x_b(j\omega) \\ x_c(j\omega) \end{bmatrix} &= k_1 \begin{bmatrix} 1 & 1 & 1 \\ \alpha^2 & \alpha & 1 \\ \alpha & \alpha^2 & 1 \end{bmatrix} \begin{bmatrix} x_p(j\omega) \\ x_n(j\omega) \\ x_0(j\omega) \end{bmatrix} \\
 \begin{bmatrix} x_p(j\omega) \\ x_n(j\omega) \\ x_0(j\omega) \end{bmatrix} &= k_2 \begin{bmatrix} 1 & \alpha & \alpha^2 \\ 1 & \alpha^2 & \alpha \\ 1 & 1 & 1 \end{bmatrix} \begin{bmatrix} x_a(j\omega) \\ x_b(j\omega) \\ x_c(j\omega) \end{bmatrix}
 \end{aligned} \tag{2.9}$$

Where $\alpha = e^{\frac{2\pi}{3}j}$ or $\alpha = 1\angle 120^\circ$. Note that for peak value, root-mean-square

value, and power-invariant property, $k_1 = \{1, \sqrt{2}, \frac{1}{\sqrt{3}}\}$ and $k_2 = \{\frac{1}{3}, \frac{1}{3\sqrt{2}}, \frac{1}{\sqrt{3}}\}$, respectively.

$$\begin{aligned}
 Z_{PN0}(j\omega) &= \begin{bmatrix} Z_{pp}(j\omega) & Z_{pn}(j\omega) & Z_{p0}(j\omega) \\ Z_{np}(j\omega) & Z_{nn}(j\omega) & Z_{n0}(j\omega) \\ Z_{0p}(j\omega) & Z_{0n}(j\omega) & Z_{00}(j\omega) \end{bmatrix} \\
 Y_{PN0}(j\omega) &= \begin{bmatrix} Y_{pp}(j\omega) & Y_{pn}(j\omega) & Y_{p0}(j\omega) \\ Y_{np}(j\omega) & Y_{nn}(j\omega) & Y_{n0}(j\omega) \\ Y_{0p}(j\omega) & Y_{0n}(j\omega) & Y_{00}(j\omega) \end{bmatrix}
 \end{aligned} \tag{2.10}$$

It is important to highlight that when transforming to the frequency domain, the steady-state values of each signal are subtracted. Therefore, the admittance is defined by the ratio of the injected current to the resulting change in the voltage ($\Delta I/\Delta V$). In the first simulation run, the positive sequence is injected into the system, and the first column of $Y_{PN0}(j\omega)$ can be calculated as:

$$\begin{aligned}
 Y_{pp}(j\omega) &= \Delta I_p(j\omega)/\Delta V_p(j\omega) \\
 Y_{np}(j\omega) &= \Delta I_n(j\omega)/\Delta V_p(j\omega) \\
 Y_{0p}(j\omega) &= \Delta I_0(j\omega)/\Delta V_p(j\omega)
 \end{aligned} \tag{2.11}$$

Similarly, the second and third columns of $Y_{PN0}(j\omega)$ can be calculated using negative and zero sequence injections:

$$\begin{aligned}
 Y_{pn}(j\omega) &= \Delta I_p(j\omega)/\Delta V_n(j\omega) \\
 Y_{nn}(j\omega) &= \Delta I_n(j\omega)/\Delta V_n(j\omega) \\
 Y_{0n}(j\omega) &= \Delta I_0(j\omega)/\Delta V_n(j\omega)
 \end{aligned} \tag{2.12}$$

$$\begin{aligned}
Y_{p0}(j\omega) &= \Delta I_p(j\omega) / \Delta V_0(j\omega) \\
Y_{n0}(j\omega) &= \Delta I_n(j\omega) / \Delta V_0(j\omega) \\
Y_{00}(j\omega) &= \Delta I_0(j\omega) / \Delta V_0(j\omega)
\end{aligned} \tag{2.13}$$

2.7 Relationship Between Phase and Sequence Variables

The sequence frequency response can also be obtained by applying the sequence transformation to the admittance matrix calculated from the phase frequency scanning. For this matter, Equation 2.14 can be applied. Note that this equation is derived for a power invariant transformation. The proof for this equation is given in Appendix C.

$$\begin{aligned}
Y_{abc}(j\omega) &= T_{pn0} Y_{pn0}(j\omega) T_{pn0}^{-1} \\
Y_{pn0}(j\omega) &= T_{pn0}^{-1} Y_{abc}(j\omega) T_{pn0}
\end{aligned} \tag{2.14}$$

Where,

$$\begin{aligned}
T_{pn0} &= \begin{bmatrix} 1 & 1 & 1 \\ \alpha^2 & \alpha & 1 \\ \alpha & \alpha^2 & 1 \end{bmatrix} \\
T_{pn0}^{-1} &= \begin{bmatrix} 1 & \alpha & \alpha^2 \\ 1 & \alpha^2 & \alpha \\ 1 & 1 & 1 \end{bmatrix}
\end{aligned} \tag{2.15}$$

2.7.1 Case Study: Sequence-Based Frequency Scanning of a Transmission Network

Figure 2.7 illustrates a balanced $500kV$ transmission line operating with fundamental frequency of $50Hz$. A $100Mvar$ shunt reactor is connected to the midpoint of the transmission network. The transmission line is modeled using the frequency dependent phase model presented in PSCAD [61]. The sequence-based frequency scanning of this system is illustrated in Figure 2.8. The multi-sine current injection has a magnitude of $0.5A$. The frequency scanning range is from $0.5Hz$ to $400Hz$ with $f_d = 0.5Hz$. From Figure 2.8, it can be observed that there is a parallel resonance at $250Hz$ in the network. Moreover, the positive and negative sequence impedance are identical, i.e. $Z_{pp}(j\omega) = Z_{nn}(j\omega)$ and there is no coupling between the positive and negative sequence, i.e. $Z_{pn}(j\omega) = 0$ and $Z_{np}(j\omega) = 0$.

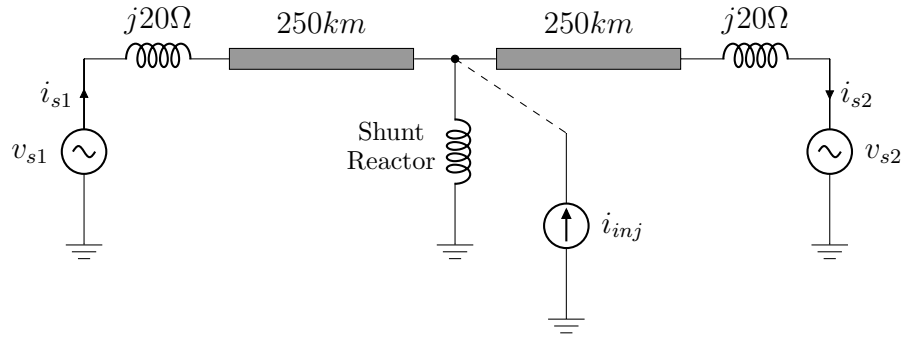


Figure 2.7: The transmission network system under study (the single phase equivalent circuit).

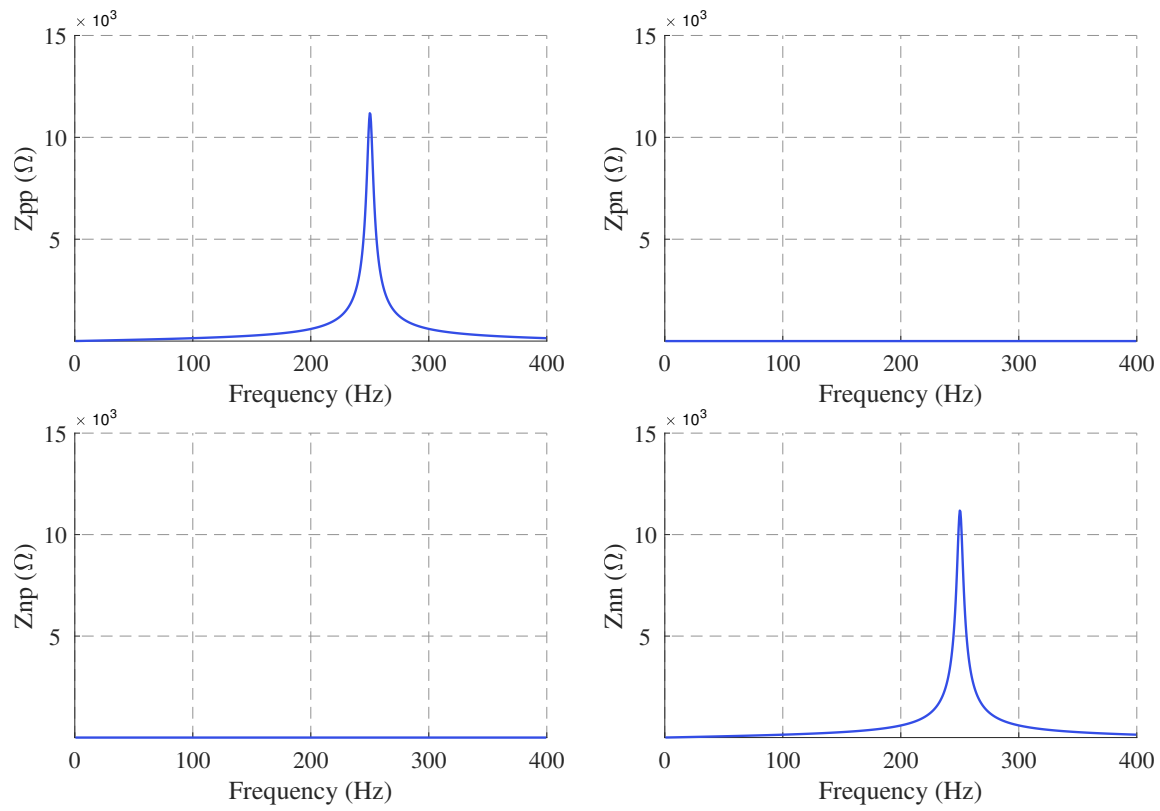


Figure 2.8: Sequence-based frequency scanning of a transmission network.

2.7.2 Case Study: Sequence-Based Frequency Scanning of a STATCOM

A ± 200 MVar STATCOM operating with a Type-I controller [27], is illustrated in Figure 2.9. This STATCOM is connected to an ac network with the operating frequency of 50Hz .

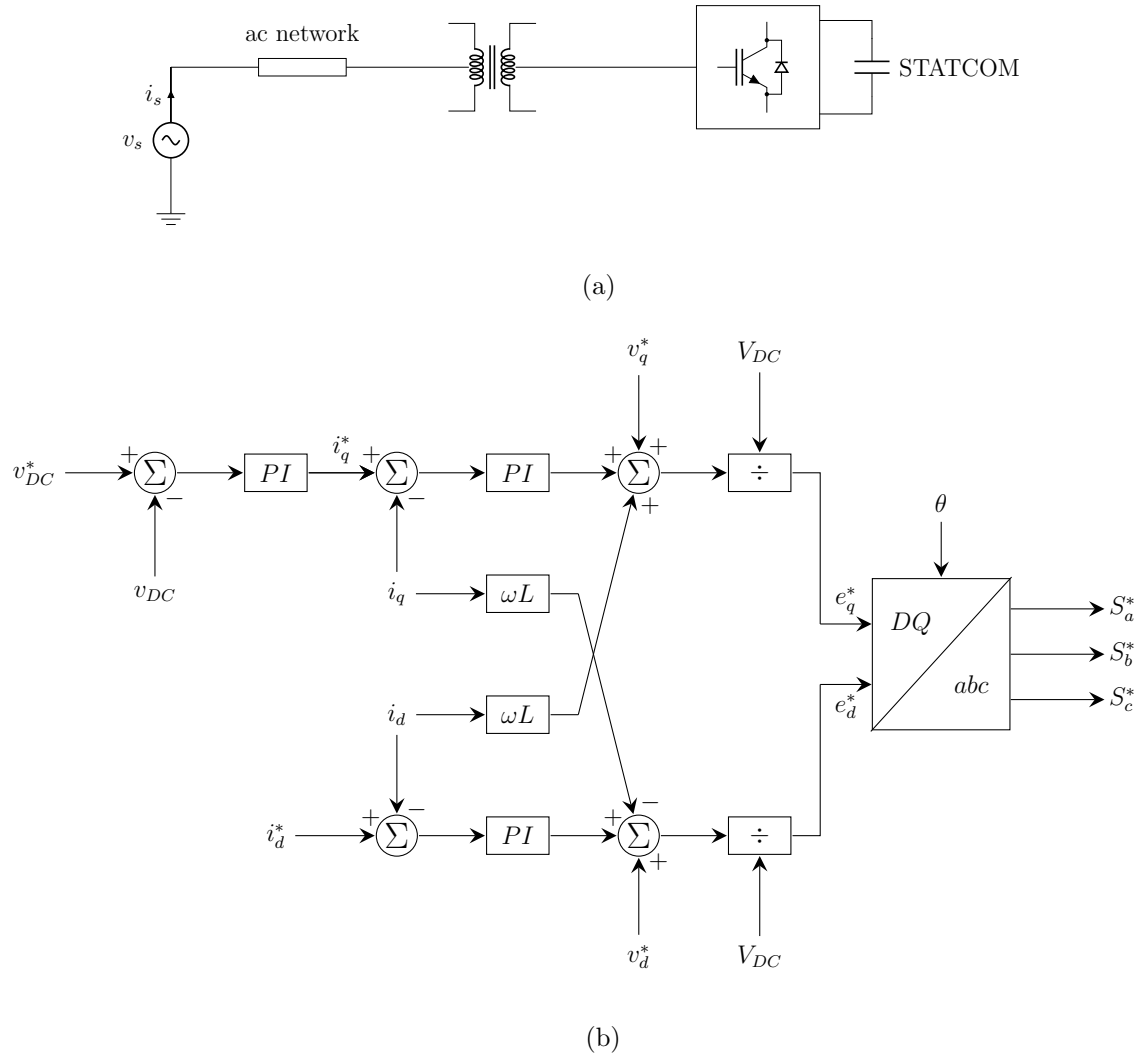


Figure 2.9: (a) STATCOM model under study (the single phase equivalent circuit) and (b) Type-I controller.

The sequence-based frequency scanning of this STATCOM is illustrated in Figure 2.10. The multi-sine voltage injection has a magnitude of $0.4kV$, and the frequency scanning range is from $0.5Hz$ to $400Hz$ with $f_d = 0.5Hz$. It can be observed that the frequency scanning results are distorted. This distortion is due to a frequency coupling between the positive and negative sequences. The coupling between the positive and negative sequences can be observed from the frequency scanning results: $Y_{pn}(j\omega) \neq 0$ and $Y_{np}(j\omega) \neq 0$.

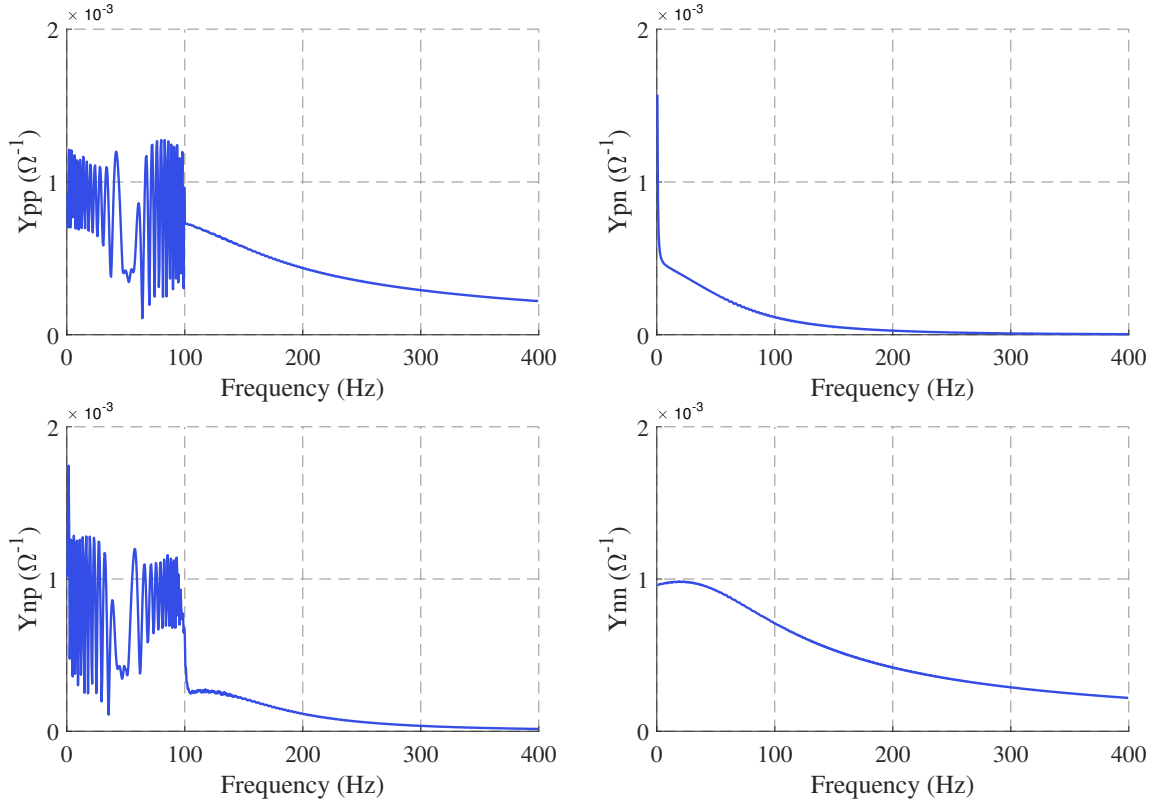


Figure 2.10: Frequency scanning of a STATCOM operating with a Type-I controller using sequence variables.

The sequence admittance which is obtained by the phase frequency scanning is illustrated in Figure 2.11. The multi-sine voltage injection has a magnitude of $0.5kV$, and the frequency scanning range is from $0.5Hz$ to $400Hz$ with $f_d = 0.5Hz$. Again, it can be observed that $Y_{pn}(j\omega) \neq 0$ and $Y_{np}(j\omega) \neq 0$. Therefore, the frequency scanning results are distorted due to the coupling between the positive and negative sequences.

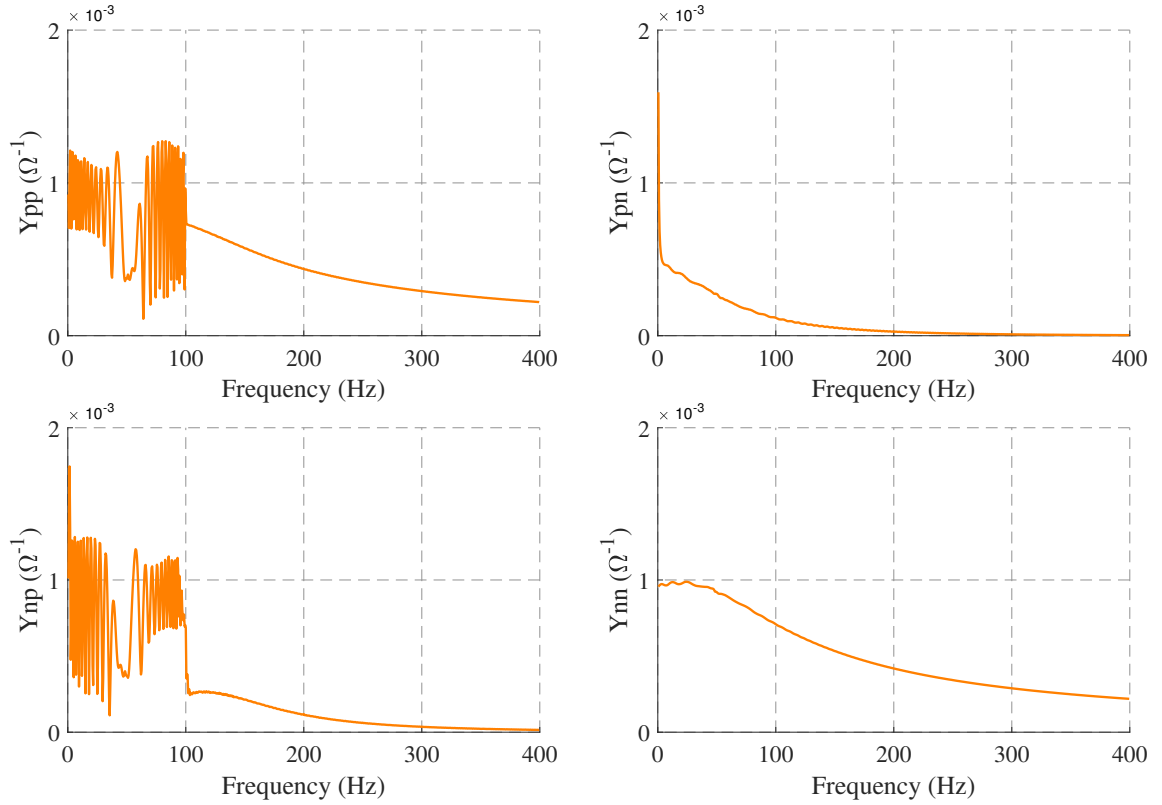


Figure 2.11: The sequence frequency response of a STATCOM operating with a Type-I controller obtained from the phase frequency scanning.

The results of frequency scanning using sequence and phase variables are compared in Figure 2.12. It is illustrated that the sequence frequency response obtained from the two methods match closely. However, both results are distorted and inaccurate. Therefore, the phase/sequence variables are not suitable choices for accurate scanning in some cases due to the reasons explained in the following section.

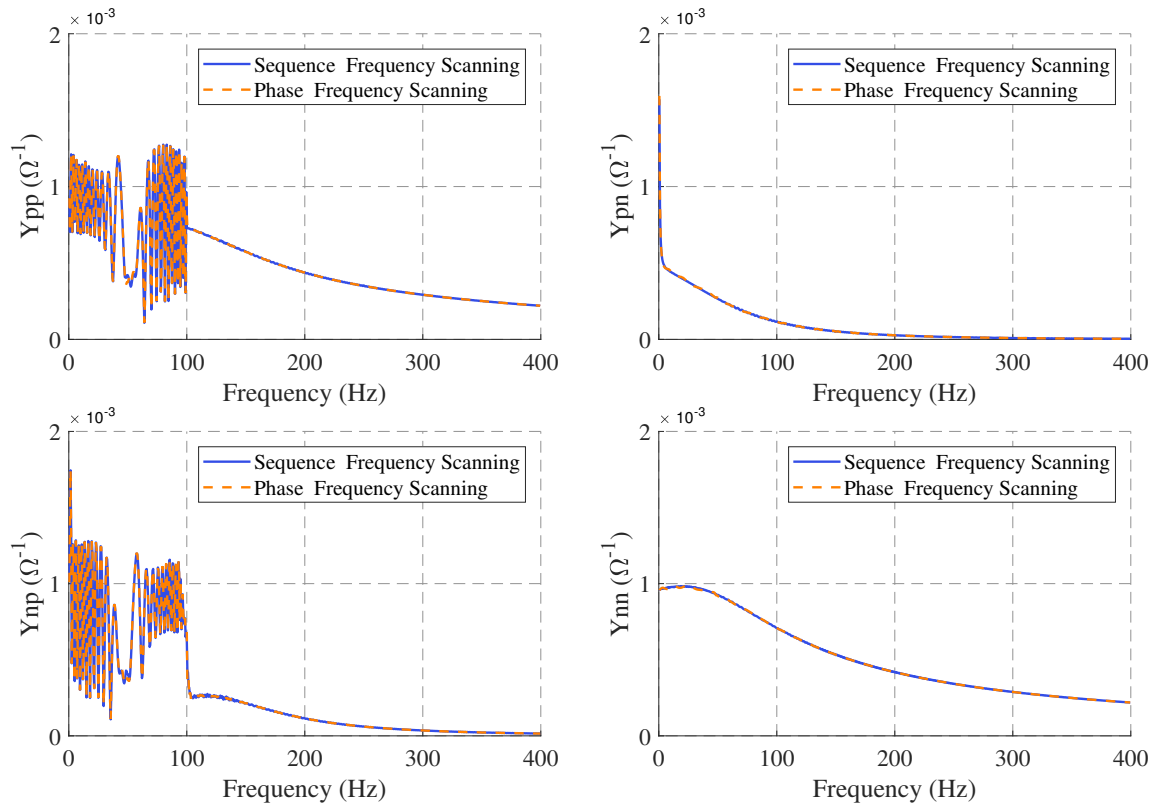


Figure 2.12: Comparison between sequence and phase frequency scanning results from the STATCOM.

2.7.3 Advantages and Disadvantages of Phase/Sequence-based Frequency Scanning

Since most power systems are modeled using phase variables, the frequency scanning using the phase variables is usually straightforward. Besides, the phase and sequence variable are interdependent, meaning that they can be converted to one another using the transformation matrix given in Equation 2.9. However, the phase/sequence-based frequency scanning can only be applied to passive systems, filters, transmission networks, etc. Nevertheless, the model of the PESs using phase/sequence variables is usually time-variant because of the switching behaviour of the converters. If the system is time-variant, the frequency response of the system can be distorted due to the frequency coupling phenomenon: *Frequency Interference* [57] also named as *mirror frequency coupling (MFC)* [23].

2.7.4 Mirror Frequency Coupling

Due to the fundamental component of the switching function, there is a frequency coupling between the positive sequence component at f and the negative sequence component at $f - 2f_0$. This phenomenon is called *frequency interference* or *mirror frequency coupling* [49], [57], [60].

Injection of a small positive sequence voltage at frequency f and at the ac side will result in a voltage at frequency $f - f_0$ at the dc side of the system, where f_0 is the fundamental frequency of the system [62]. This voltage will cause a current at the same frequency $f - f_0$. This current will then be reflected on the ac side and it will produce two current perturbations: 1) a positive sequence current at frequency

f and 2) a negative sequence current at frequency $f - 2f_0$. This process is illustrated in figure 2.13.

Note that, for $f < 2f_0$ the voltage injection at frequency f will result in positive sequence currents of f and $2f_0 - f$. This is because the negative sequence current at $f - 2f_0$ has a negative value, which can be transferred into a positive value at the same frequency of $|f - 2f_0|$ in the positive sequence.

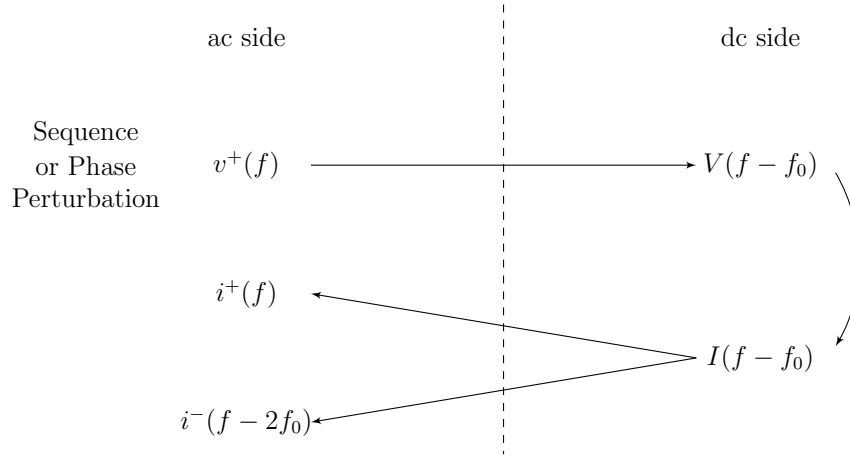


Figure 2.13: Coupling between the ac and dc sides of the system and frequency interference in the phase/sequence domains.

2.7.5 Case Study: Frequency Coupling Phenomena in a Transmission Network

Figure 2.14, illustrates the positive sequence line voltage and line current of the transmission network shown in Figure 2.7. It can be observed that a voltage is injected at $40Hz$, and the current has only a $40Hz$ component. Hence, no MFC exists. It is important to highlight that since the injection is done in a single frequency, the energy of that injection is higher, thus larger spikes are observed.

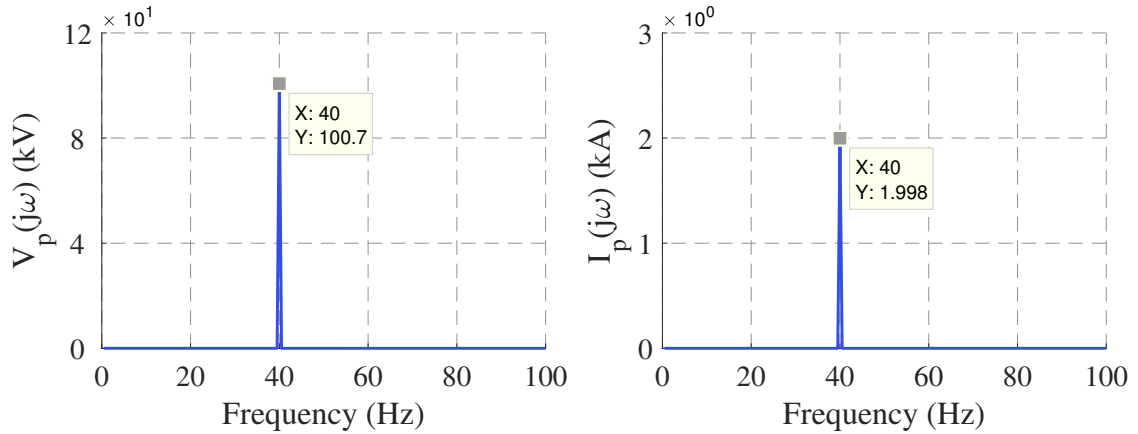


Figure 2.14: Positive sequence voltage injection and the resulting positive sequence current of a transmission line. No MFC is observed.

2.7.6 Case Study: Frequency Coupling Phenomena in a STATCOM

Figure 2.15, illustrates the positive sequence line voltage and line current of the STATCOM shown in Figure 2.9. It can be observed that a voltage is injected at 40Hz and the current has two frequency components: a 40Hz and a 60Hz component. These two components are equal to f and $|f - 2f_0|$. Hence, MFC exists.

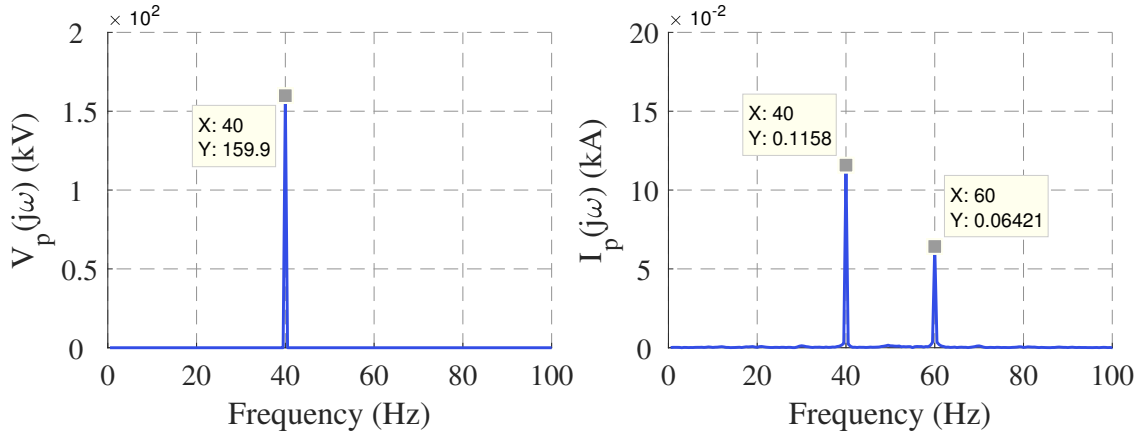


Figure 2.15: Positive sequence voltage injection and the resulting positive sequence current of a STATCOM. MFC is observed

It can be concluded that for the systems containing passive elements such as a transmission network, the model of the system using the phase/sequence variables is time-invariant. Therefore, MFC does not exist, and the phase/sequence-based frequency scanning can be used to obtain an accurate frequency response. However, for PESs containing switching power electronics such as a STATCOM, the model of such systems in the phase/sequence domain is not time-invariant due to the switching actions of the power electronic devices. Therefore, in such systems, MFC does exist, and the phase/sequence-based frequency scanning cannot be used to obtain an

accurate frequency response. In such circumstances, the synchronous reference frame (SRF) or the DQ frame can be used to transform the time domain variables to the DQ variables and possibly eliminate the frequency coupling to obtain an accurate scan.

2.8 Solution for Distorted frequency Scanning

There are a few solutions for taking care of the MFC, which occurs when using the phase/sequence variable based frequency scanning. One method for smoothing the results is to apply averaging techniques to the distorted parts of the signal. Another method is dividing the scan range into smaller ranges and perform multiple scans until the desired frequency range is covered. This method was first introduced by [57]:

Injecting a positive sequence signal at frequency f results in a positive sequence component at f a negative sequence component at $f - 2f_0$. Consequently, two situations can occur:

1. $f < 2f_0$: In this situation, the negative sequence component ($f - 2f_0$), lies at a negative frequency. This means that a positive sequence component exist at $2f_0 - f$ ². The proof for this is illustrated in Appendix A. What this means is that the sequence component at $2f_0 - f$ has resulted from two perturbations: 1) positive sequence injection at frequency f and 2) positive sequence injection at frequency $2f_0 - f$. As a result, if the frequency scanning range is set to include only f or $2f_0 - f$, the frequency coupling between these components will be avoided. This can be achieved by dividing $f < 2f_0$ region, into two smaller

² $I_n(j\omega) = I_p^*(j\omega)$

regions of $f < f_0$ and $f_0 \leq f < 2f_0$.

2. $f > 2f_0$: In this situation, the negative sequence component $(f - 2f_0)$, lies at a positive frequency. This means that any positive sequence component has resulted from only one perturbation. Therefore, in this frequency range, MFC does not exist, and the entire range can be used for frequency scanning without any divisions.

Consequently, by dividing the desired range of the scanning into two regions of $f < f_0$ and $f \geq f_0$, the frequency coupling is avoided, and the frequency scanning results will not be distorted.

Next, an example for dividing the range of frequency scanning is illustrated, and it is shown that using this method, the frequency scanning results are smooth, and the frequency interference is avoided properly.

2.8.1 Case Study: Sequence-Based Frequency Scanning of a STATCOM Obtained by Dividing the Frequency Range

Figure 2.16, illustrates the frequency scanning results of the STATCOM shown in Figure 2.9. The multi-sine voltage injection has a magnitude of $0.4kV$, and the frequency scanning range is from $0.5Hz$ to $400Hz$ with $f_d = 0.5Hz$. Note that two independent scans from $0.5Hz$ to $49.5Hz$, and $50Hz$ to $400Hz$ are performed. It is observed that, by properly dividing the frequency scanning range into smaller parts, the frequency interference can be avoided, and a smooth frequency response using the sequence/phase variables can be obtained.

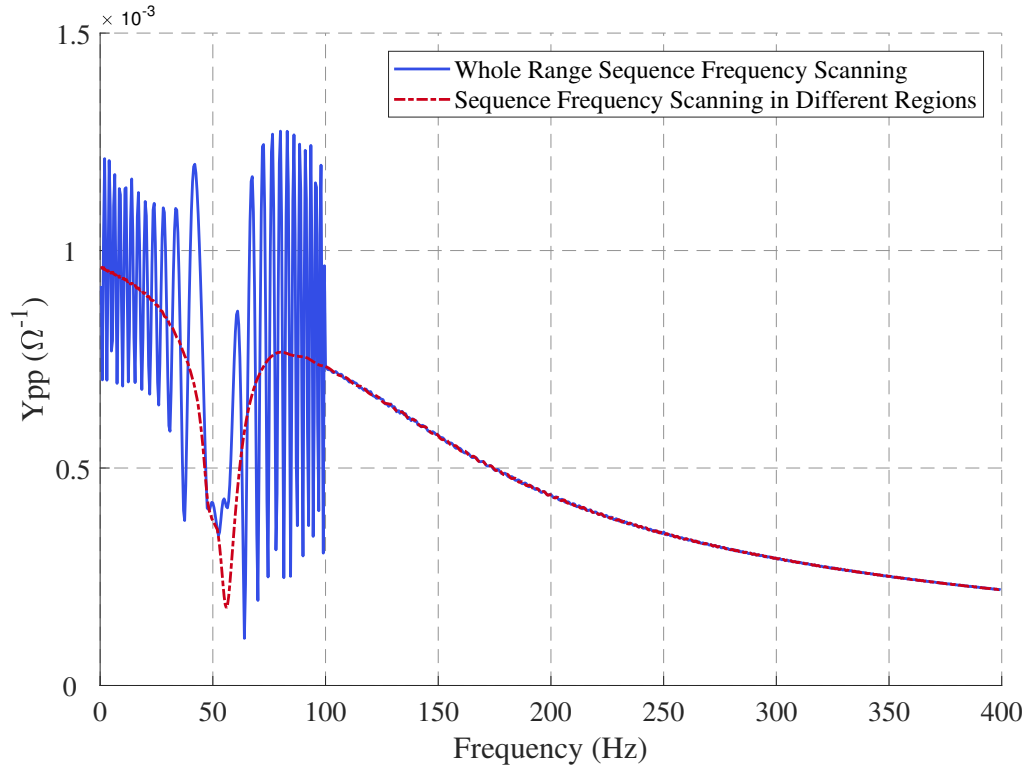


Figure 2.16: The sequence-based frequency scanning of a STATCOM using two independent scans: 1) from $0.5Hz$ to $49.5Hz$ 2) from $50Hz$ to $400Hz$.

From the discussion above, it can be concluded that obtaining the accurate frequency scanning results using sequence/phase variables is not possible by performing one scan. However, DQ-based frequency scanning can be used to obtain accurate frequency scanning results by scanning the whole frequency range at once. This technique is explained in the following section.

2.9 Frequency Scanning Using DQ Variables

For most PESs operating at balanced condition with negligible lower order harmonics, a DQ transformation can be used to obtain a time-invariant model of the system [8], [16]. Therefore, DQ variables are suitable for modeling such PESs. The procedure of Performing a DQ-based frequency scanning is illustrated in Figure 2.17.

The multi-sine signal is injected separately via 3 independent simulation runs in the d , q and 0 channels. Because the simulators use phase variables, a DQ transformation, as shown in Equation 2.16, is required to convert the DQ-based multi-sine signal to a three-phase signal. The resulting three-phase signal is then used for injection to the system. The voltages and currents of the three-phase system are captured at the point of injection for the duration of the simulation run. These signals are then transformed into the frequency domain using anti-aliasing filter, down sampling and FFT.

The impedance/admittance matrix of the PES ($Y_{DQ0}(j\omega)$) which is a 3×3 matrix is shown in Equation 2.17. The zero sequence can be neglected if the system configuration makes it impossible for it to flow, e.g., if there is a delta-connected transformer winding or an ungrounded Y transformer winding. This is usually the

case in most PESs. In such circumstances, the impedance/admittance matrix of the PES ($Y_{DQ}(j\omega)$) will be a 2×2 matrix. Note that the procedure of multi-sine voltage injection illustrated in Figure 2.17, extracts the admittance of the system. If the impedance of the system is desired, a multi-sine current injection can be used instead.

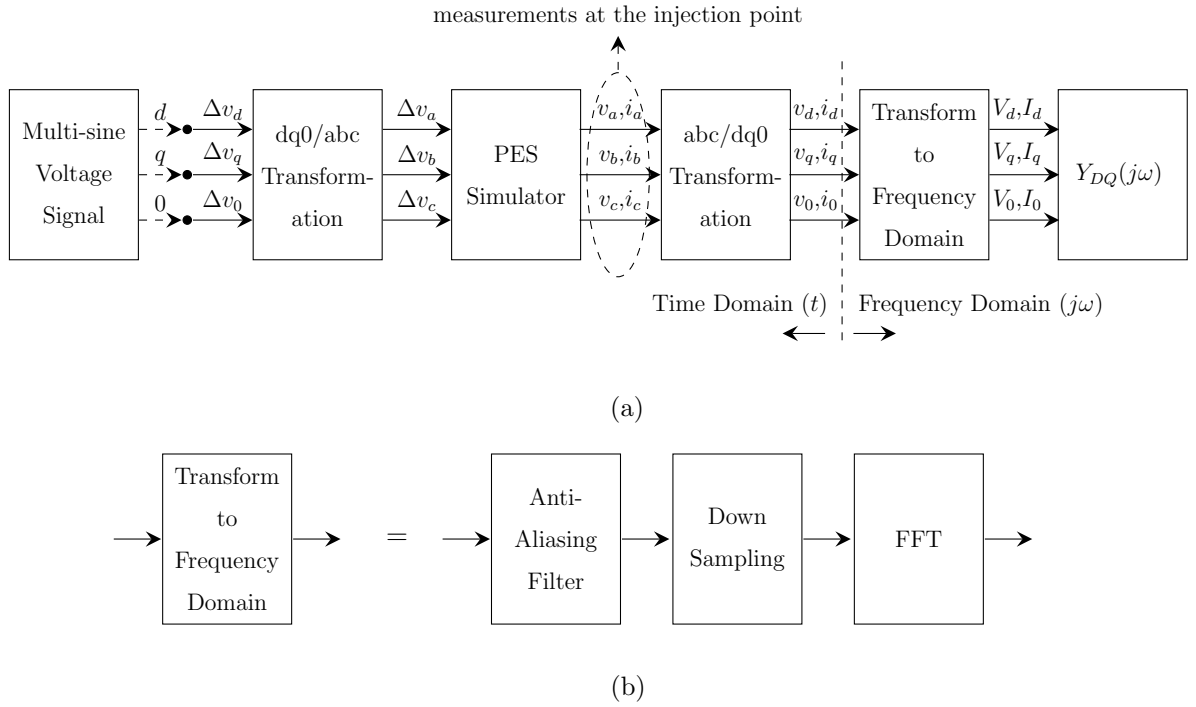


Figure 2.17: (a) Procedure of performing DQ-based frequency scanning for a PES and (b) Transformation to frequency domain.

For a three-phase ac network operating at balanced condition, with negligible lower order harmonics, the synchronous reference frame (SRF) or the DQ frame can be used to transform the time domain variables to the DQ variables [63]:

$$\begin{aligned}
 \begin{bmatrix} x_a(t) \\ x_b(t) \\ x_c(t) \end{bmatrix} &= k_1 \begin{bmatrix} \cos(\theta) & \sin(\theta) & \frac{1}{\sqrt{2}} \\ \cos(\theta - \frac{2\pi}{3}) & \sin(\theta - \frac{2\pi}{3}) & \frac{1}{\sqrt{2}} \\ \cos(\theta + \frac{2\pi}{3}) & \sin(\theta + \frac{2\pi}{3}) & \frac{1}{\sqrt{2}} \end{bmatrix} \begin{bmatrix} x_d(t) \\ x_q(t) \\ x_0(t) \end{bmatrix} \\
 \begin{bmatrix} x_d(t) \\ x_q(t) \\ x_0(t) \end{bmatrix} &= k_2 \begin{bmatrix} \cos(\theta) & \cos(\theta - \frac{2\pi}{3}) & \cos(\theta + \frac{2\pi}{3}) \\ \sin(\theta) & \sin(\theta - \frac{2\pi}{3}) & \sin(\theta + \frac{2\pi}{3}) \\ \frac{1}{\sqrt{2}} & \frac{1}{\sqrt{2}} & \frac{1}{\sqrt{2}} \end{bmatrix} \begin{bmatrix} x_a(t) \\ x_b(t) \\ x_c(t) \end{bmatrix}
 \end{aligned} \tag{2.16}$$

Where θ , the transformation angle, is given by $\theta = \omega_0 t + \delta$, and ω_0 is the fundamental frequency of the system. In PESs, the angle θ is usually taken as the angle of the PCC bus as determined by the phase-locked loop (and the angle δ is 0 degrees). Note that for peak value, root-mean-square value, and power-invariant property, $k_1 = \{1, \sqrt{2}, \sqrt{\frac{2}{3}}\}$ and $k_2 = \{\frac{2}{3}, \frac{\sqrt{2}}{3}, \sqrt{\frac{2}{3}}\}$. respectively.

$$\begin{aligned}
 Z_{DQ0}(j\omega) &= \begin{bmatrix} Z_{dd}(j\omega) & Z_{dq}(j\omega) & Z_{d0}(j\omega) \\ Z_{qd}(j\omega) & Z_{qq}(j\omega) & Z_{q0}(j\omega) \\ Z_{0d}(j\omega) & Z_{0q}(j\omega) & Z_{00}(j\omega) \end{bmatrix} \\
 Y_{DQ0}(j\omega) &= \begin{bmatrix} Y_{dd}(j\omega) & Y_{dq}(j\omega) & Y_{d0}(j\omega) \\ Y_{qd}(j\omega) & Y_{qq}(j\omega) & Y_{q0}(j\omega) \\ Y_{0d}(j\omega) & Y_{0q}(j\omega) & Y_{00}(j\omega) \end{bmatrix}
 \end{aligned} \tag{2.17}$$

It is important to highlight that when transforming to the frequency domain,

the steady-state values of each signal are subtracted. Therefore, the admittance is defined by the ratio of the injected current to the resulting change in the voltage ($\Delta I/\Delta V$). When injecting in one channel, other channels are set to zero. In the first simulation run, the multi-sine signal is injected into the d channel, and the first column of $Y_{DQ0}(j\omega)$ can be calculated as:

$$\begin{aligned} Y_{dd}(j\omega) &= \Delta I_d(j\omega)/\Delta V_d(j\omega) \\ Y_{qd}(j\omega) &= \Delta I_q(j\omega)/\Delta V_d(j\omega) \\ Y_{0d}(j\omega) &= \Delta I_0(j\omega)/\Delta V_d(j\omega) \end{aligned} \tag{2.18}$$

Similarly, the second and third columns of $Y_{DQ0}(j\omega)$ can be calculated by injecting the multi-sine signal into the q and 0 channels, respectively:

$$\begin{aligned} Y_{dq}(j\omega) &= \Delta I_d(j\omega)/\Delta V_q(j\omega) \\ Y_{qq}(j\omega) &= \Delta I_q(j\omega)/\Delta V_q(j\omega) \\ Y_{0q}(j\omega) &= \Delta I_0(j\omega)/\Delta V_q(j\omega) \\ Y_{d0}(j\omega) &= \Delta I_d(j\omega)/\Delta V_0(j\omega) \\ Y_{q0}(j\omega) &= \Delta I_q(j\omega)/\Delta V_0(j\omega) \\ Y_{00}(j\omega) &= \Delta I_0(j\omega)/\Delta V_0(j\omega) \end{aligned} \tag{2.19}$$

$$\tag{2.20}$$

Applying the DQ transformation to the time-domain variables creates two coupled dc systems operating at a dc equilibrium point [63]. By applying this transformation, the time-varying variables in the time domain model become dc quantities in the DQ model. Hence, the DQ model of the system becomes time-invariant, and the system can then be linearized around the dc equilibrium operating point using conventional

methods [30], [45], [63].

Applying the DQ frame can be advantageous since DQ variables can be frequency decoupled [60]. This means the mirror frequency coupling explained in Section 2.7.4, will not be an issue in the DQ frame. Moreover, using a DQ frame enables us to control the active and reactive powers independently [64]. Note that although modeling the system using DQ variables can be beneficial for obtaining the frequency scanning of most PESs, this method cannot be applied to systems with significant lower order harmonics, negative-sequence controllers, etc [27].

2.9.1 Case Study: DQ-Based Frequency Scanning of a Transmission Network

The DQ-based frequency scanning of the transmission network shown in Figure 2.7, is illustrated in Figure 2.18. The multi-sine current injection has a magnitude of $0.5A$, and the frequency scanning range is from $0.5Hz$ to $300Hz$ with $f_d = 0.5Hz$. The scan results are not distorted, which indicates the absence of MFC. Moreover, $Z_{dq}(j\omega) = Z_{qd}(j\omega) \neq 0$, which indicates there is an equal coupling between d and q components.

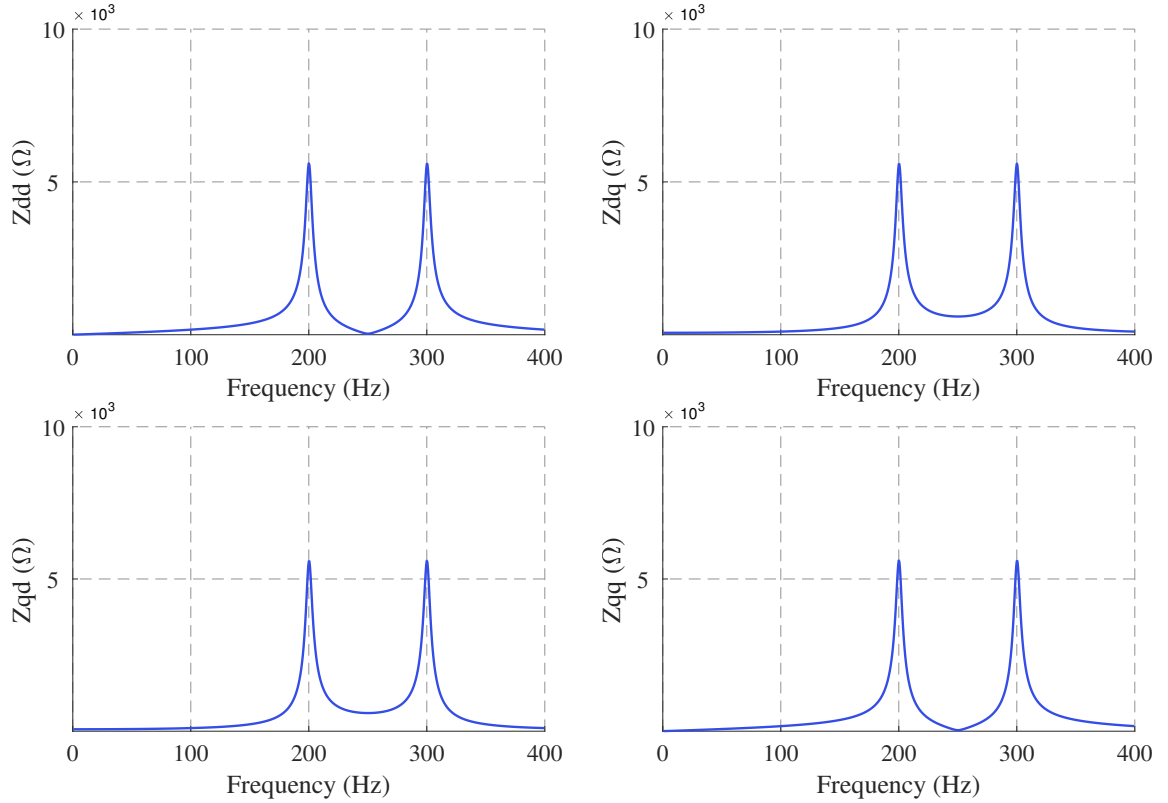


Figure 2.18: DQ-based frequency scanning of a transmission network

Figure 2.19, illustrates the line voltages and line currents of the transmission network shown in Figure 2.7 in the DQ domain. It can be observed that a voltage is injected at $40Hz$, and the current has only a $40Hz$ component. Hence, no MFC exists.

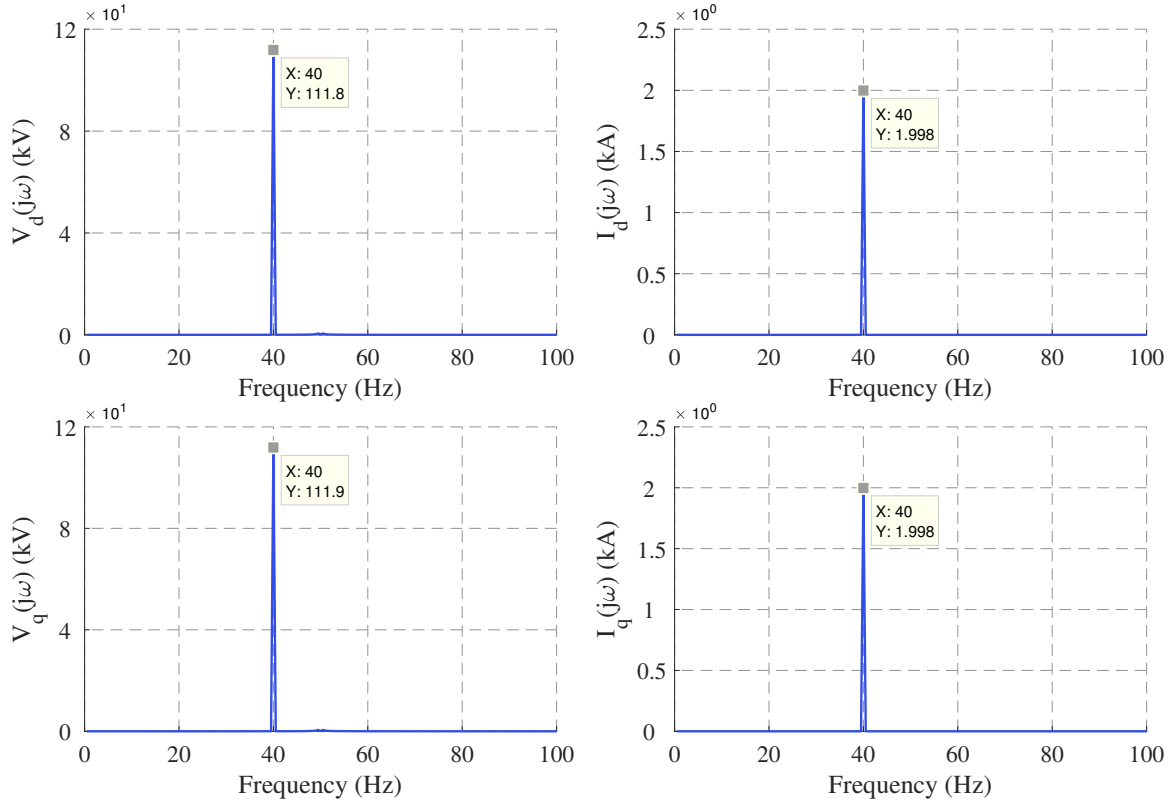


Figure 2.19: D and Q voltage injection and the resulting D and Q currents of a transmission line. No MFC is observed.

2.9.2 Case Study: DQ-Based Frequency Scanning of a STATCOM

The DQ-based frequency scanning of the STATCOM shown in Figure 2.9, is illustrated in Figure 2.20. The multi-sine voltage injection has a magnitude of $0.4kV$, and the frequency scanning range is from $0.5Hz$ to $400Hz$ with $f_d = 0.5Hz$. Since MFC does not exist, the scan results are not distorted.

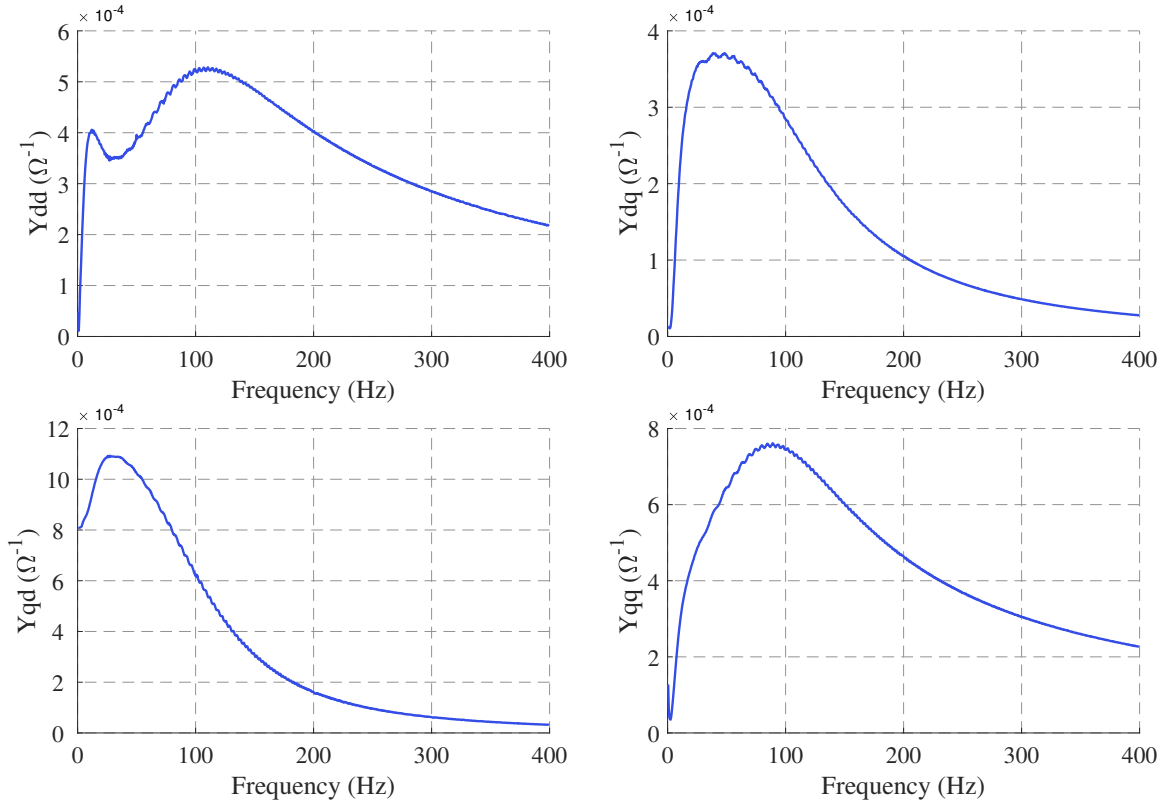


Figure 2.20: DQ-based frequency scanning of a STATCOM

Figure 2.21, illustrates the line voltages and line currents of the STATCOM shown in Figure 2.9 in the DQ domain. It can be observed that a voltage is injected at $40Hz$, and the current has only one frequency component at a $40Hz$. Hence, MFC does not

exist, and the DQ variables make a suitable choice for accurate frequency scanning.

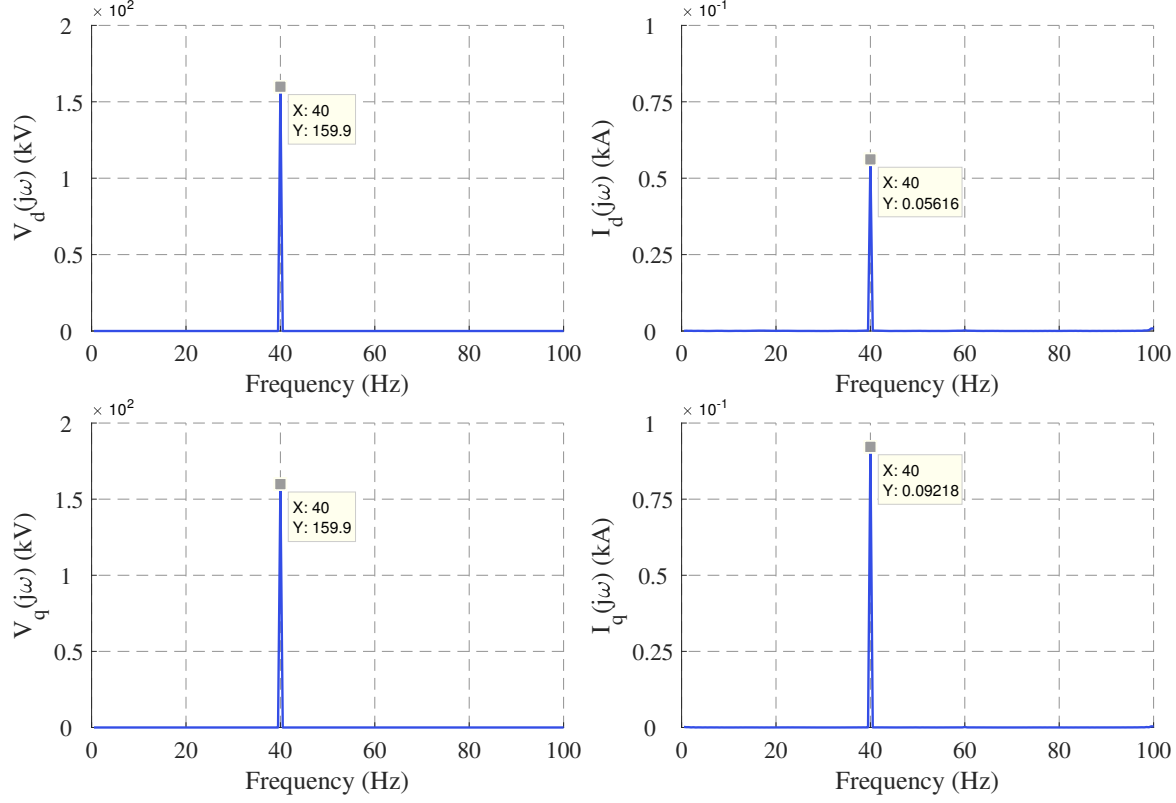


Figure 2.21: D and Q voltage injection and the resulting D and Q currents of a STATCOM. No MFC is observed

2.9.3 Absence of Frequency Interference Using DQ-Based Frequency Scanning

In section 2.7.4, it was discussed that there is a frequency coupling between the positive and negative sequences, which results in a distorted frequency scanning. In section 2.8, DQ-based frequency scanning was introduced as a solution for getting a smooth frequency response since no frequency coupling exists between the frequency components.

A voltage perturbation via d and q variables at frequency f must first be converted into sequence/phase variables for injection into the system. Therefore, the DQ voltage injection at frequency f is first transformed into a positive and a negative voltage at frequencies $f + f_0$ and $f - f_0$, respectively. Note that f_0 is the fundamental frequency of the system. These voltage perturbations will result in a voltage at frequency f on the dc side of the system. This dc side voltage will then create current at the same frequency f . This current is then reflected back on the ac side which produces a positive and a negative current at frequencies $f + f_0$ and $f - f_0$, respectively. Transforming these two current signals back to the DQ domain shows a DQ current at frequency f only.

As a result, the DQ voltage injection at frequency f will result in a DQ current at frequency f . Thus, no frequency coupling is observed when using DQ-based frequency scanning, and the scanning results will not be distorted.

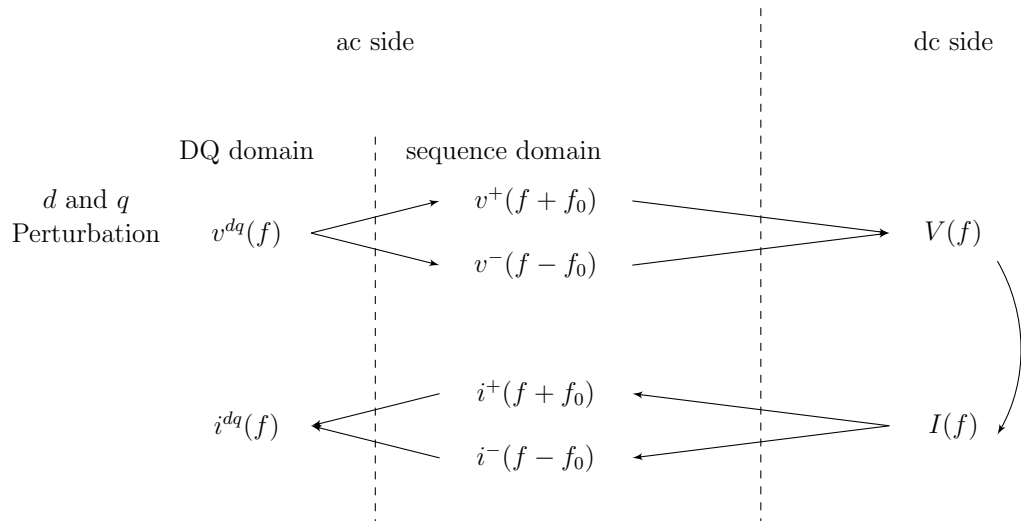


Figure 2.22: Coupling between the ac and dc sides of the system and frequency interference in DQ domain.

2.9.4 Relationship Between Sequence and DQ Variables

As illustrated, the DQ variables are suitable for the frequency scanning of PESs containing switching power electronics. Since the DQ frame enables the decoupling of the phases, one can convert the sequence variables to DQ variables in order to obtain the frequency scanning of a system. By using Equation 2.9 and Equation 2.16, sequence to DQ domain transformation can be obtained [27] as illustrated in Equation 2.21. This method is also referred to as the *Modified Sequence Domain (MSD)* [60].

$$\begin{bmatrix} x_d(j\omega_{dq}) \\ x_q(j\omega_{dq}) \end{bmatrix} = \frac{1}{\sqrt{2}} \begin{bmatrix} 1 & 1 \\ j & -j \end{bmatrix} \begin{bmatrix} x_p(j\omega_p) \\ x_n(j\omega_n) \end{bmatrix} \quad (2.21)$$

Where,

$$\omega_{dq} = \omega_p - \omega_0 \quad (2.22)$$

$$\omega_{dq} = \omega_n + \omega_0$$

Note that $\omega_s = 2\pi f_0$ and f_0 is the fundamental frequency of the system. The proof for these equations is given in Appendix B. It is important to highlight that the Equation 2.21 is obtained assuming that the "q" axis is lagging the "d" axis. For situations when the "q" axis is leading the "d" axis, sequence to DQ transformation can be obtained as illustrated in Equation 2.23.

$$\begin{bmatrix} x_d(j\omega_{dq}) \\ x_q(j\omega_{dq}) \end{bmatrix} = \frac{1}{\sqrt{2}} \begin{bmatrix} 1 & j \\ 1 & -j \end{bmatrix} \begin{bmatrix} x_p(j\omega_p) \\ x_n(j\omega_n) \end{bmatrix} \quad (2.23)$$

Equation 2.22 proves that when the sequence domain variables are transformed into DQ domain variables, a phase shift exists. Therefore, for each frequency, two

frequency components in the DQ Domain exist due to the positive and negative frequency components. Because of the coupling between the positive and negative sequences, these frequency components are distant by twice the fundamental frequency. This phenomenon is illustrated in Figure 2.8 and Figure 2.18, where the resonant frequency of the transmission network in the sequence domain, $f = 250Hz$, is mapped into two frequencies in the DQ domain, $f = 200Hz$ and $f = 300Hz$ and the gap between these two frequencies are equal to $2f_0 = 100Hz$.

Similarly by using Equation 2.9 and Equation 2.16, DQ to sequence transformation can be obtained [60] as illustrated in Equation 2.24.

$$\begin{bmatrix} x_p(j\omega_p) \\ x_n(j\omega_n) \end{bmatrix} = \frac{1}{\sqrt{2}} \begin{bmatrix} 1 & -j \\ 1 & j \end{bmatrix} \begin{bmatrix} x_d(j\omega_{dq}) \\ x_q(j\omega_{dq}) \end{bmatrix} \quad (2.24)$$

Where,

$$\omega_p = \omega_{dq} + \omega_0 \quad (2.25)$$

$$\omega_n = \omega_{dq} - \omega_0$$

Note that $\omega_s = 2\pi f_0$ and f_0 is the fundamental frequency of the system. It is important to highlight that some frequency components in the DQ domain belong to the positive sequence while the other ones belong to the negative sequence. If a frequency component follows a positive /negative sequence behaviour when transformed, it belongs to the positive/negative sequence.

It is possible to obtain the sequence admittance of a PES based on the DQ domain admittance from the equations explained in this section. A sequence admittance matrix can be obtained from the DQ admittance matrix, and vice versa, as illustrates

in Equation 2.26 [60].

$$\begin{aligned} Y_{PN} &= TY_{DQ}T^{-1} \\ Y_{DQ} &= T^{-1}Y_{PN}T \end{aligned} \tag{2.26}$$

Where,

$$\begin{aligned} T &= \frac{1}{\sqrt{2}} \begin{bmatrix} 1 & -j \\ 1 & j \end{bmatrix} \\ T^{-1} &= \frac{1}{\sqrt{2}} \begin{bmatrix} 1 & 1 \\ j & -j \end{bmatrix} \end{aligned} \tag{2.27}$$

Figure 2.23, illustrates the impedance matrix $Y_{PN}(j\omega)$ obtained from two methods: 1) sequence frequency scanning and 2) DQ-based frequency scanning and then applying Equation 2.26. It is observed that a frequency shift of $50Hz$ exists between the two methods. Figure 2.24, illustrates that the positive sequence admittance obtained from sequence and DQ-based frequency scans are matching.

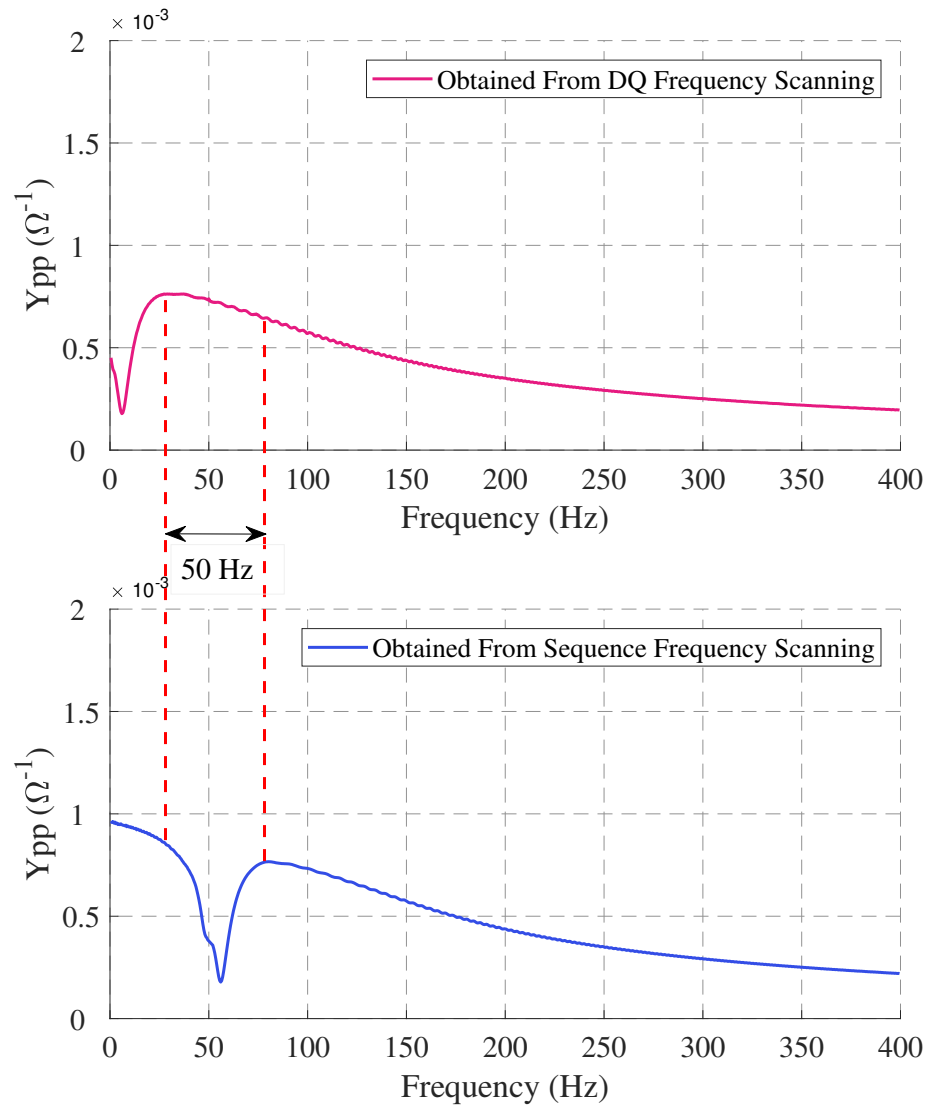


Figure 2.23: Frequency shift between Sequence and DQ-based frequency scanning

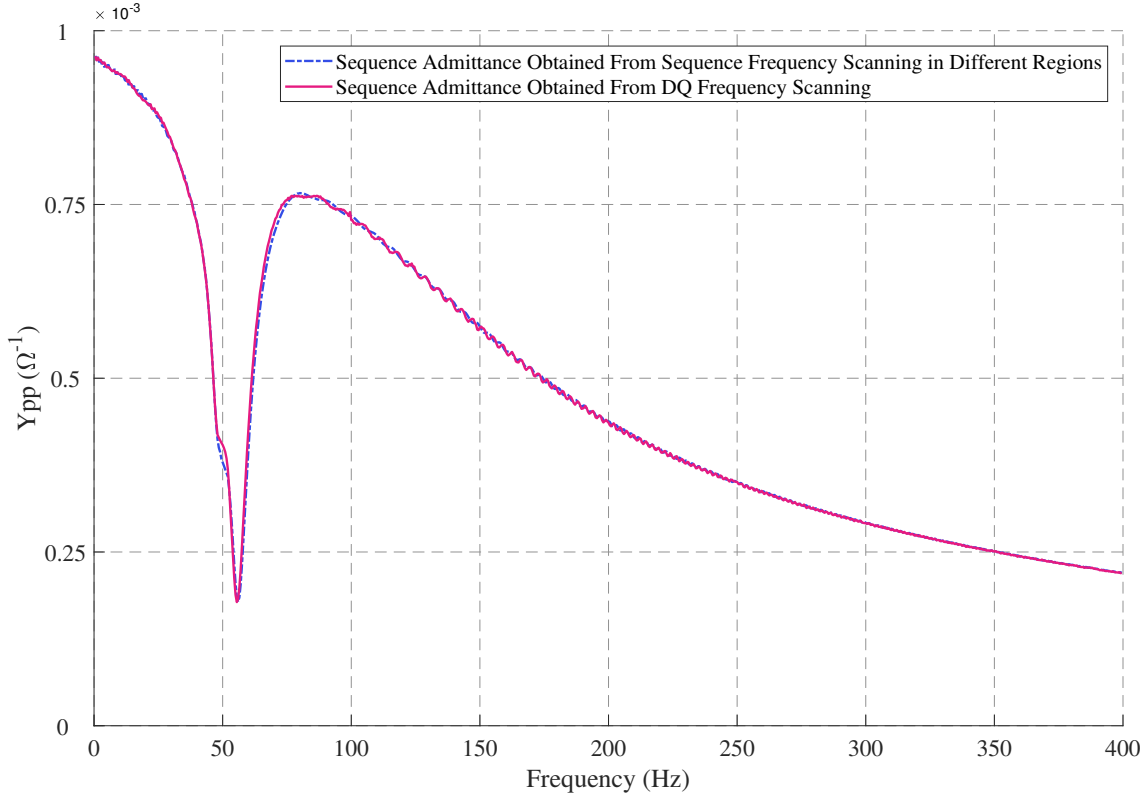


Figure 2.24: Comparison between the positive sequence admittance obtained from Sequence and DQ-based frequency scanning

2.10 $\alpha\beta$ -Based Frequency Scanning

The procedure of Performing an $\alpha\beta$ -based frequency scanning is illustrated in Figure 2.25. The multi-sine signal is injected in the α , β and 0 channels separately via 3 independent simulation runs. Because the simulators use phase variables, an $\alpha\beta 0$ transformation, also known as Clarke's transformation as shown in Equation 2.28, is required to convert the $\alpha\beta 0$ based multi-sine signal to a three-phase signal. Note that Clarke's transformation is a constant transformation of the phase variables. The resulting three-phase signal is then used for injection to the system. The voltages and

currents of the three-phase system are captured at the point of injection for the duration of the simulation run. These signals are then transformed into the frequency domain using anti-aliasing filter, down sampling and FFT. The impedance/admittance matrix of the PES ($Y_{\alpha\beta 0}(j\omega)$) which is a 3×3 matrix is shown in Equation 2.29. The zero sequence can be neglected if the system configuration makes it impossible for it to flow, e.g., if there is a delta-connected transformer winding or an ungrounded Y transformer winding. This is usually the case in most PESs. In such circumstances the impedance/admittance matrix of the PES ($Y_{\alpha\beta}(j\omega)$) will be a 2×2 matrix. Note that the procedure of multi-sine voltage injection illustrated in Figure 2.25, extracts the admittance of the system. If the impedance of the system is desired, a multi-sine current injection can be used instead.

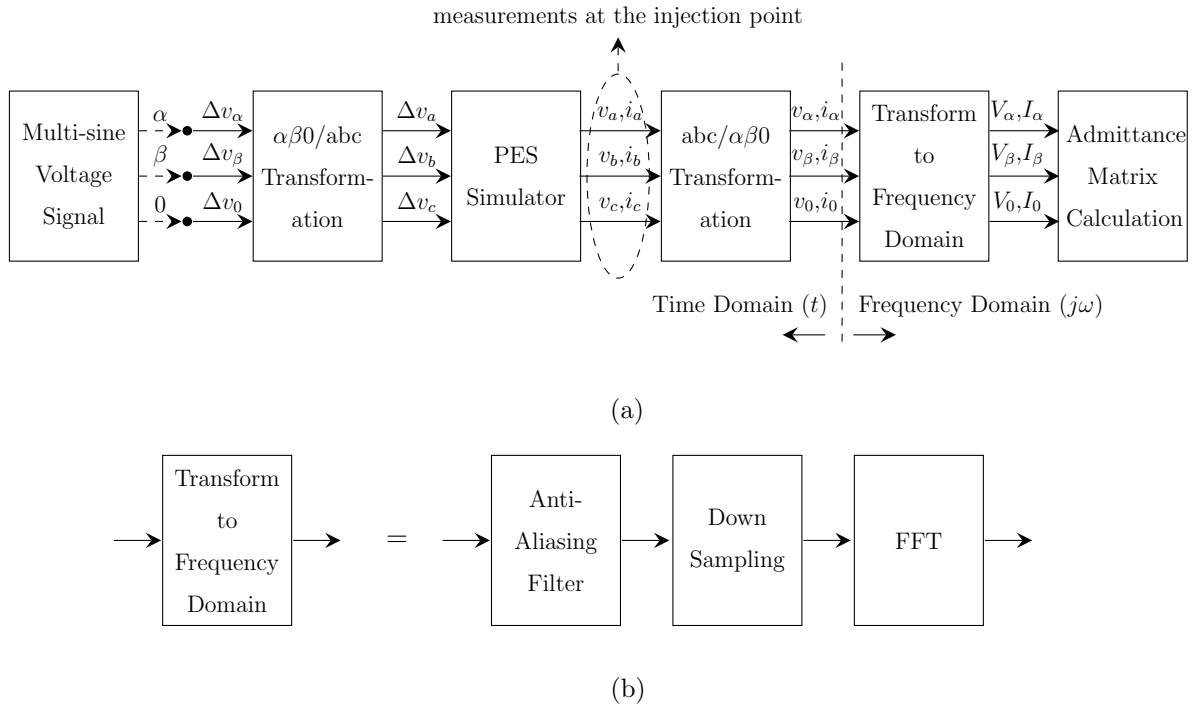


Figure 2.25: (a) Procedure of performing $\alpha\beta$ -based frequency scanning for a PES and (b) Transformation to frequency domain.

$$\begin{aligned}
\begin{bmatrix} x_a \\ x_b \\ x_c \end{bmatrix} &= k_1 \begin{bmatrix} 1 & 0 & \frac{1}{\sqrt{2}} \\ -\frac{1}{2} & \frac{\sqrt{3}}{2} & \frac{1}{\sqrt{2}} \\ -\frac{1}{2} & -\frac{\sqrt{3}}{2} & \frac{1}{\sqrt{2}} \end{bmatrix} \begin{bmatrix} x_\alpha \\ x_\beta \\ x_0 \end{bmatrix} \\
\begin{bmatrix} x_\alpha \\ x_\beta \\ x_0 \end{bmatrix} &= k_2 \begin{bmatrix} 1 & -\frac{1}{2} & -\frac{1}{2} \\ 0 & \frac{\sqrt{3}}{2} & -\frac{\sqrt{3}}{2} \\ \frac{1}{\sqrt{2}} & \frac{1}{\sqrt{2}} & \frac{1}{\sqrt{2}} \end{bmatrix} \begin{bmatrix} x_a \\ x_b \\ x_c \end{bmatrix}
\end{aligned} \tag{2.28}$$

Note that for peak value, root-mean-square value, and power-invariant property, $k_1 = \{1, \sqrt{2}, \sqrt{\frac{2}{3}}\}$ and $k_2 = \{\frac{2}{3}, \frac{\sqrt{2}}{3}, \sqrt{\frac{2}{3}}\}$. respectively.

$$\begin{aligned}
Z_{\alpha\beta 0}(j\omega) &= \begin{bmatrix} Z_{\alpha\alpha}(j\omega) & Z_{\alpha\beta}(j\omega) & Z_{\alpha 0}(j\omega) \\ Z_{\beta\alpha}(j\omega) & Z_{\beta\beta}(j\omega) & Z_{\beta 0}(j\omega) \\ Z_{0\alpha}(j\omega) & Z_{0\beta}(j\omega) & Z_{00}(j\omega) \end{bmatrix} \\
Y_{\alpha\beta 0}(j\omega) &= \begin{bmatrix} Y_{\alpha\alpha}(j\omega) & Y_{\alpha\beta}(j\omega) & Y_{\alpha 0}(j\omega) \\ Y_{\beta\alpha}(j\omega) & Y_{\beta\beta}(j\omega) & Y_{\beta 0}(j\omega) \\ Y_{0\alpha}(j\omega) & Y_{0\beta}(j\omega) & Y_{00}(j\omega) \end{bmatrix}
\end{aligned} \tag{2.29}$$

It is important to highlight that when transforming to the frequency domain, the steady-state values of each signal are subtracted. Therefore, the admittance is defined by the ratio of the injected current to the resulting change in the voltage ($\Delta I/\Delta V$). When injecting in one channel, other channels are set to zero. In the first simulation run, the multi-sine signal is injected into the α channel and the first column of

$Y_{\alpha\beta 0}(j\omega)$ can be calculated as:

$$\begin{aligned}
 Y_{\alpha\alpha}(j\omega) &= I_{\alpha}(j\omega)/V_{\alpha}(j\omega) \\
 Y_{\beta\alpha}(j\omega) &= I_{\beta}(j\omega)/V_{\alpha}(j\omega) \\
 Y_{0\alpha}(j\omega) &= I_0(j\omega)/V_{\alpha}(j\omega)
 \end{aligned} \tag{2.30}$$

Similarly, the second and third columns of $Y_{\alpha\beta 0}(j\omega)$ can be calculated by injecting the multi-sine signal into the β and 0 channels, respectively:

$$\begin{aligned}
 Y_{\alpha\beta}(j\omega) &= I_{\alpha}(j\omega)/V_{\beta}(j\omega) \\
 Y_{\beta\beta}(j\omega) &= I_{\beta}(j\omega)/V_{\beta}(j\omega) \\
 Y_{0\beta}(j\omega) &= I_0(j\omega)/V_{\beta}(j\omega)
 \end{aligned} \tag{2.31}$$

$$\begin{aligned}
 Y_{\alpha 0}(j\omega) &= I_{\alpha}(j\omega)/V_0(j\omega) \\
 Y_{\beta 0}(j\omega) &= I_{\beta}(j\omega)/V_0(j\omega) \\
 Y_{00}(j\omega) &= I_0(j\omega)/V_0(j\omega)
 \end{aligned} \tag{2.32}$$

2.10.1 Case Study: $\alpha\beta$ -Based Frequency Scanning of a STATCOM

The $\alpha\beta$ -based frequency scanning of the STATCOM shown in Figure 2.9, is illustrated in Figure 2.26. The multi-sine voltage injection has a magnitude of $0.4kV$, and the frequency scanning range is from $0.5Hz$ to $400Hz$ with $f_d = 0.5Hz$.

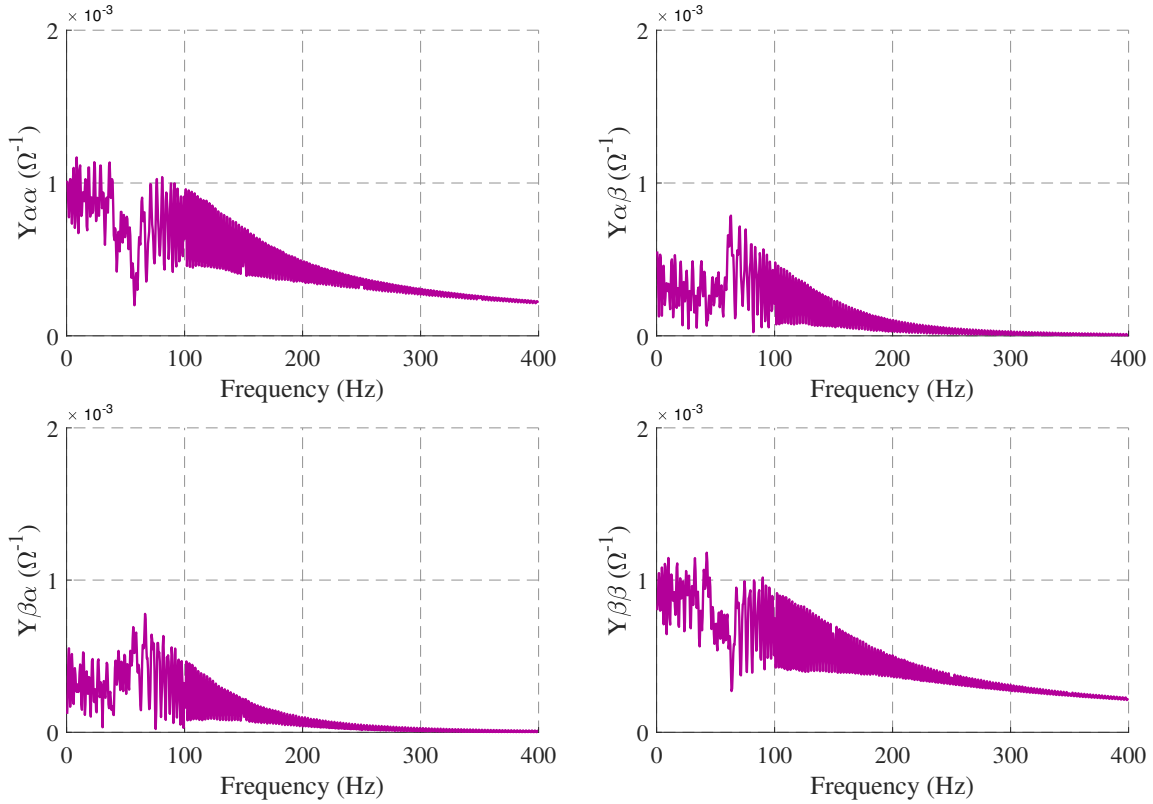


Figure 2.26: $\alpha\beta$ -based frequency scanning of a STATCOM

It can be observed that the scan results are distorted due to the frequency coupling between the positive and negative sequences. Consequently, the frequency scanning using $\alpha\beta$ variables is not suitable for PESs with switching power electronics, such as STATCOM. Note that this frequency coupling can be avoided by performing frequency scanning in regions, as discussed in 2.8.

2.11 Conclusion

In this chapter, the frequency scanning technique performed using phase/sequence variables, DQ variables and $\alpha\beta$ variables were introduced. For PESs using power electronic switching devices, such as STATCOMs, the frequency scanning using phase/sequence variables and $\alpha\beta$ variables is distorted and not accurate due to the coupling between the positive and negative sequences or MFC. DQ variables are a suitable choice for the frequency scanning of converter-based PESs. It was also discussed that all of the presented domains are equivalent to one another, and the variables in each domain can be transformed into other domains using a proper transformation matrix.

The stability analysis of the interactions between a PES and its grid is discussed in the next chapter. The stability analysis techniques are presented and compared using simulations.

Chapter 3

Stability Analysis of PES-Grid Interactions

3.1 Introduction

The frequency scanning technique discussed in the previous chapter is a useful tool for studying the interactions between the grid and the power electronic system (PES). Several techniques, such as Generalized Nyquist Criterion (GNC), can be applied to obtain the stability of the grid-connected PESs. For stability screening purposes, the overall system is first modeled as two independent subsystems, and the frequency scanning of each subsystem is obtained. The grid-connected PES is then modeled as a closed-loop system so that GNC or any frequency domain stability criteria can be used to analyze the stability of the overall system. The DQ-based frequency scanning had several advantages over other types of frequency scanning methods, as discussed in the previous chapter. Thus, the interactions between a PES and its grid is analyzed

using the DQ-based scanning. This procedure is discussed in detail in the following sections of this chapter.

3.2 Interaction Study of Grid-connected PESs

A grid-connected PES is illustrated in Figure 3.1. For interaction studies, the small signal equivalent model is often used, where the overall grid-connected PES is first divided into two independent subsystems, as illustrated in Figure 3.2. The small signal model of each system can then be obtained via perturbing the system with a small-amplitude current or voltage signal as illustrated in the following sections. The model of the two independent subsystems is then combined to obtain the overall model of the system.

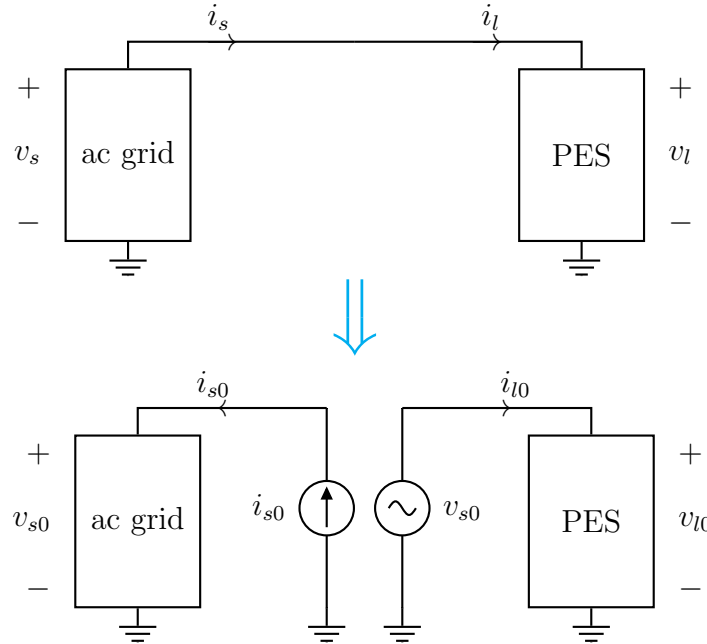


Figure 3.1: A PES connected to a grid and the independent models of the ac grid and PES.

3.2.1 Perturbation Via Current Signal

A current signal perturbation is illustrated in Figure 3.2. The frequency scanning technique can be applied to obtain the frequency response of each subsystem for the desired frequency range. In case of a current perturbation, the impedance matrix of the grid ($Z_{grid}(j\omega)$) and the admittance matrix of PES ($Y_{PES}(j\omega)$) can be calculated using the frequency scanning results. Note that a stable simulation for the configuration in Figure 3.1 exists.

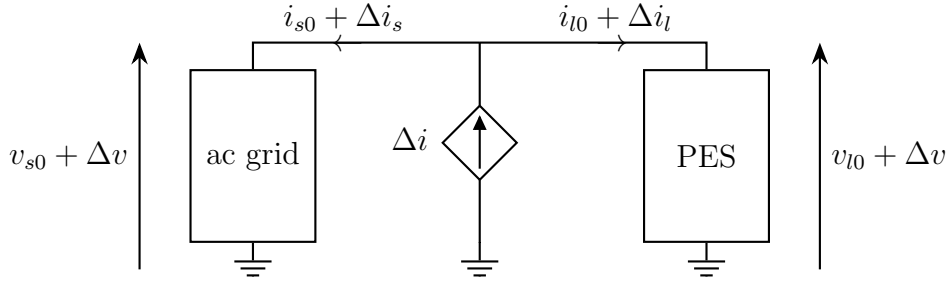


Figure 3.2: Small signal current perturbation

For a current signal injection, the closed-loop model which represents the grid-connected PES is illustrated in Figure 3.3.

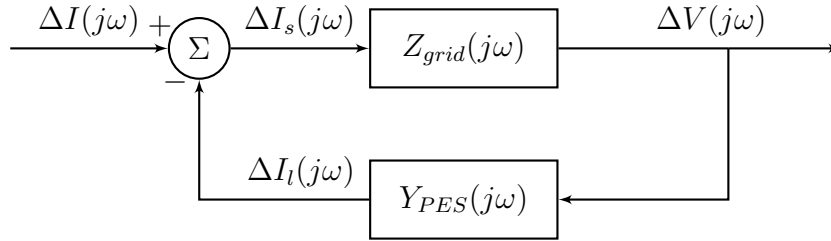


Figure 3.3: The closed-loop model of the combined system using the small signal models of ac grid and PES models, when a current perturbation is applied.

The closed-loop transfer function of the overall system illustrated in Figure 3.3 can be written as:

$$T(j\omega) = \frac{\Delta V(j\omega)}{\Delta I(j\omega)} = (D_1(j\omega))^{-1} Z_{grid}(j\omega) \quad (3.1)$$

Where,

$$D_1(j\omega) = I + Z_{grid}(j\omega) Y_{PES}(j\omega) \quad (3.2)$$

It is important to highlight that the inverse forms of the small-signal models of the ac grid and PES can also be used when obtaining the closed-loop model, as illustrated in Figure 3.4.

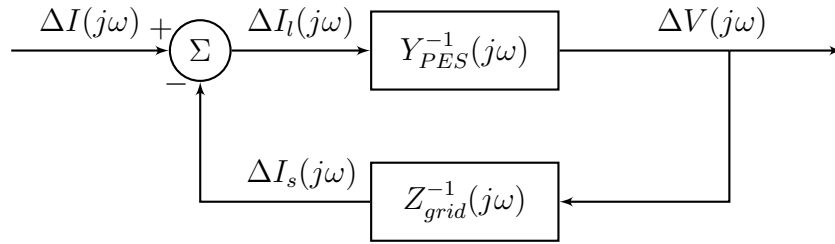


Figure 3.4: The closed-loop model of the combined system using the inverse small signal models of the ac grid and PES, when a current perturbation is applied.

The closed-loop transfer function of the overall system illustrated in Figure 3.4 can be written as:

$$T(j\omega) = \frac{\Delta V(j\omega)}{\Delta I(j\omega)} = (D'_1(j\omega))^{-1} Y_{PES}^{-1}(j\omega) \quad (3.3)$$

Where,

$$D'_1(j\omega) = I + Y_{PES}^{-1}(j\omega) Z_{grid}^{-1}(j\omega) \quad (3.4)$$

Assuming the impedance matrix of the ac grid ($Z_{grid}(j\omega)$) and the admittance matrix of the PES ($Y_{PES}(j\omega)$) represent the stable subsystems for a current signal injection, the stability of $Y_{PES}^{-1}(j\omega)$ with current perturbation is not guaranteed due to the locations of the zeros of the original subsystem. The reason is that, the open-loop system ($Y_{PES}^{-1}(j\omega)Z_{grid}^{-1}(j\omega)$) may have right half-plane (RHP) poles although Y_{PES} and Z_{grid} have only left half-plane (LHP) poles due to the fact that Y_{PES} may have RHP zeros, because it may be non-passive.

3.2.2 Perturbation Via Voltage Signal

A voltage signal perturbation is illustrated in Figure 3.5. The frequency scanning technique can be applied to obtain the frequency response of each subsystem for the desired frequency range. When a voltage perturbation is applied, the impedance matrix of the grid ($Z_{grid}(j\omega)$) and the admittance matrix of the PES ($Y_{PES}(j\omega)$) can be calculated using the frequency scanning results. Again, notice that a stable simulation for the configuration in Figure 3.1 exists.

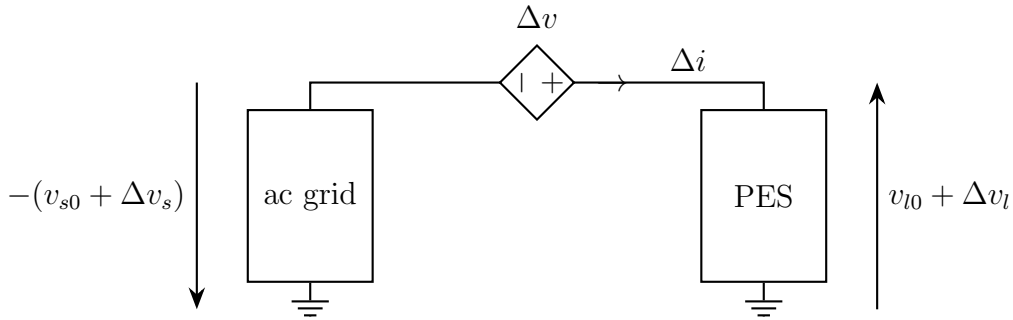


Figure 3.5: Small signal voltage perturbation

For a voltage signal injection, the closed-loop model which represents the grid-connected PES is illustrated in Figure 3.6.

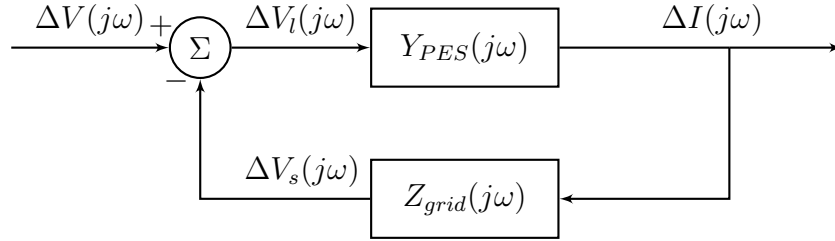


Figure 3.6: The closed-loop model of the combined system using the small signal models of ac grid and PES models, when a voltage perturbation is applied.

The closed-loop transfer function of the overall system illustrated in Figure 3.6 can be written as:

$$T(j\omega) = \frac{\Delta I(j\omega)}{\Delta V(j\omega)} = (D_2(j\omega))^{-1} Y_{PES}(j\omega) \quad (3.5)$$

Where,

$$D_2(j\omega) = I + Y_{PES}(j\omega) Z_{grid}(j\omega) \quad (3.6)$$

The inverse forms of the small-signal models of the ac grid and PES can also be used when obtaining the closed-loop model, as illustrated in Figure 3.7.

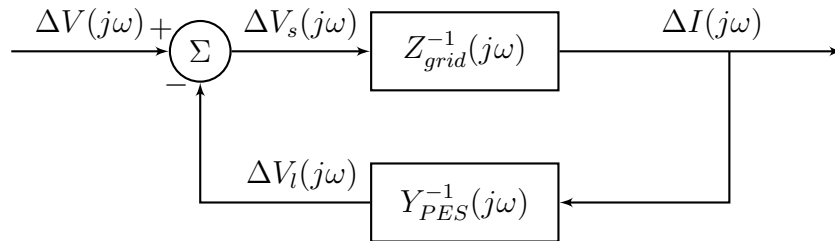


Figure 3.7: The closed-loop model of the combined system using the inverse small signal models of ac grid and PES models, when a voltage perturbation is applied.

The closed-loop transfer function of the overall system illustrated in Figure 3.7 can be written as:

$$T(j\omega) = \frac{\Delta I(j\omega)}{\Delta V(j\omega)} = (D'_2(j\omega))^{-1} Z_{grid}^{-1}(j\omega) \quad (3.7)$$

Where,

$$D'_2(j\omega) = I + Z_{grid}^{-1}(j\omega) Y_{PES}^{-1}(j\omega) \quad (3.8)$$

Assuming the impedance matrix of the ac grid ($Z_{grid}(j\omega)$) and the admittance matrix of the PES ($Y_{PES}(j\omega)$) are both stable subsystems, the stability of $Y_{PES}^{-1}(j\omega)$ with voltage perturbation is not guaranteed since Y_{PES} may have RHP zeros, because it may be non-passive.

As mentioned in Section 2.3, applying the current perturbation or the voltage perturbation depends on the inherent input of a system, which can be determined using the state-space equations of the system.

3.2.3 Equivalence Between the Current Perturbation and the Voltage Perturbation for Stability Screening

It can be shown that a voltage perturbation has the same results as a current perturbation when screening the stability of the interactions. Consider the closed-loop model illustrated in Figure 3.3. The state-space equations of the grid as PES can be calculated as:

$$\begin{aligned}\dot{X}_S &= A_S X_S + B_S U_S, & Y_S &= C_S U_S \\ \dot{X}_L &= A_L X_L + B_L U_L, & Y_L &= C_L U_L\end{aligned}\tag{3.9}$$

Where the state matrix pair $\{A_S, B_S, C_S\}$ and $\{A_L, B_L, C_L\}$ represent the model of the grid and PES respectively. From Figure 3.3, it is understood that $U_S = \Delta I - Y_L$ and $U_L = Y_S$. Therefore, the following equation can be obtained:

$$\begin{bmatrix} \dot{X}_S \\ \dot{X}_L \end{bmatrix} = \begin{bmatrix} A_S & -B_S C_L \\ B_L C_S & A_L \end{bmatrix} \begin{bmatrix} X_S \\ X_L \end{bmatrix} + \begin{bmatrix} B_S \\ 0 \end{bmatrix} \Delta I\tag{3.10}$$

The same pair of state-space matrix illustrated in Equation 3.9 can be used when a voltage perturbation is applied. From Figure 3.6 it is understood that $U_S = Y_L$ and $U_L = \Delta V - Y_S$. Therefore, the following equation can be obtained:

$$\begin{bmatrix} \dot{X}_S \\ \dot{X}_L \end{bmatrix} = \begin{bmatrix} A_S & B_S C_L \\ -B_L C_S & A_L \end{bmatrix} \begin{bmatrix} X_S \\ X_L \end{bmatrix} + \begin{bmatrix} 0 \\ B_L \end{bmatrix} \Delta V\tag{3.11}$$

For stability screening purposes, GNC or eigenlocus stability approach are used for the closed-loop transfer function of the overall system.

The eigenlocus stability approach investigates the movement of all eigenvalues of the closed-loop transfer function as a function of frequency and then applies the

Nyquist Criterion. The closed-loop eigenvalues can be obtained from the characteristic polynomial.

For a current perturbation, the characteristic polynomial can be calculated as:

$$\det(\lambda I - \begin{bmatrix} A_S & -B_S C_L \\ B_L C_S & A_L \end{bmatrix}) = 0 \quad (3.12)$$

$$(\lambda I - A_S)(\lambda I - A_L) + (B_S C_L)(B_L C_S) = 0$$

For a voltage perturbation, the characteristic polynomial can be calculated as:

$$\det(\lambda I - \begin{bmatrix} A_S & B_S C_L \\ -B_L C_S & A_L \end{bmatrix}) = 0 \quad (3.13)$$

$$(\lambda I - A_S)(\lambda I - A_L) + (B_S C_L)(B_L C_S) = 0$$

From these two equations, it is obvious that the characteristic polynomial is the same for both current and voltage perturbation. Consequently, the voltage perturbation gives the same stability results as the current perturbation. Hence, the stability is preserved.

3.3 Stability Analysis Criterion

The closed-loop transfer function of the overall system, illustrated in Section 3.2, can be used to determine the stability of the interactions between the PES and its grid.

In Section 3.2, it was shown that a grid-connected PES could be described as in Equation 3.2, Equation 3.4, Equation 3.6 and Equation 3.8. Note that ΔV and ΔI are D-Q vector quantities. Assume for the moment that the network external to the PES is passive and so the stability information can be determined from $D_1(j\omega)$. In general, admittance or impedance formulations are possible (i.e. Equation 3.2 and Equation 3.6), giving $D_1(j\omega)$ and $D_2(j\omega)$. Let us refer to this part of the transfer function generically as $D(j\omega)$ ¹, which is a 2×2 matrix.

The eigenvalues of $D(j\omega)$ are λ_1 and λ_2 . These eigenvalues are frequency-dependent, and they change as ω traverses from $-\infty$ to $+\infty$. The loci of these eigenvalues are called eigen-loci, and they are used to determine the stability of the interactions. Note that these eigenvalues are not the eigenvalues of the system but of the 2×2 transfer matrix. No matter what the order of network or PES, if only one PES is present, $D(j\omega)$ will always be of dimension 2×2 .

In the discussion to follow, different "Nyquist" contours plots are considered, which plot whether the imaginary part versus the real part of $\det(D(j\omega))$ (Generalized Nyquist) or the imaginary versus the real parts of the eigenvalues of $D(j\omega)$, as the frequency ω is varied from $-\infty$ to $+\infty$.

¹For simplicity, let us consider $D(j\omega) = I + Z_{grid}(j\omega)Y_{PES}(j\omega)$

Considering the system illustrated in Figure 3.8:

1. Generalized Nyquist Stability Criterion (GNC)
2. Eigenlocus Stability Analysis ¹

could be applied to access the stability of the system. Note that GNC is applied to $\det(D(j\omega))$, whereas the eigenlocus stability approach uses the eigen-loci of the $D(j\omega)$ to determine the stability of the system.² These methods are discussed and compared in the following sections. Note that, as mentioned in Section 3.2.1 and Section 3.2.2, the inverse models shown in Equation 3.4 and Equation 3.8 may be unstable since the PESs are non-passive. This issue may create difficulty applying the stability analysis techniques when using the inverse model for the PESs. Consequently, if it is known that $Y_{PES}(j\omega)$ is unstable and $Y_{PES}^{-1}(j\omega)$ is stable, GNC or the eigenlocus stability analysis can be applied to determine the stability of the system.

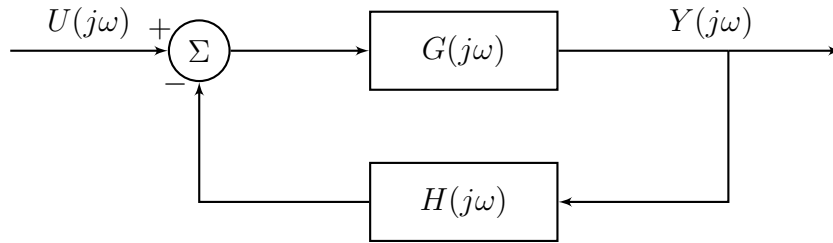


Figure 3.8: The closed-loop transfer function of the overall system.

¹Note that, the eigenlocus stability analysis discussed in this thesis is different from the state-space based eigenvalue analysis.

²In eigenlocus stability approach, the number of net encirclement is equal to the sum of the encirclement of all eigen-locus.

3.4 Generalized Nyquist Stability Criterion

Assuming that $G(j\omega)$ and $H(j\omega)$ illustrated in Figure 3.8 are independently stable systems, the closed-loop system will be stable if the Nyquist contour of $\Delta(j\omega)$ given in Equation 3.14, does not encircle the origin of the complex plane as ω traverses from $-\infty$ to $+\infty$ [27], [35], [65].

$$\Delta(j\omega) = \det D(j\omega) \quad (3.14)$$

Where,

$$D(j\omega) = I + G(j\omega)H(j\omega) \quad (3.15)$$

Note that, for the inverse models of the subsystems, $D(j\omega) = I + G^{-1}(j\omega)H^{-1}(j\omega)$.

3.5 Eigenlocus Stability Analysis

Stability analysis based on GNC is very simple because it requires calculating only the determinant of $D(j\omega)$. Although more time consuming, it is possible to analyze the stability of the system by monitoring the individual eigen-loci of $D(j\omega)$ instead of the easier approach of calculating the determinant of $D(j\omega)$ [66].

Consider the system illustrated in Figure 3.8. The eigen-loci of the MIMO system can be calculated by solving Equation 3.16.

$$\det(\lambda I - D(j\omega)) = 0 \quad (3.16)$$

The closed-loop system will be stable if the net number of counterclockwise encirclement of the eigen-loci of $D(j\omega)$ around the origin is equal to the total number

of RHP poles of the open-loop system $G(j\omega)H(j\omega)$. Note that the number of net encirclement is equal to the sum of the encirclement of all eigen-locus.

Alternatively, the eigen-loci of $G(j\omega)H(j\omega)$ can be used to determine the stability of a system. The eigen-loci of $G(j\omega)H(j\omega)$ are the eigen-loci of $D(j\omega)$ shifted to the left of the real axis by 1.0. In this case the encirclement around $(-1, 0)$ is observed instead.

3.6 Encirclement of a Contour around the Origin or $(-1, 0)$

The closed-loop transfer function of the overall system shown in Figure 3.8 is given by:

$$Tf(j\omega) = \left(I + G(j\omega)H(j\omega) \right)^{-1} G(j\omega) \quad (3.17)$$

For any given system, using either of the stability criterion, the following equation determines the number of RHP poles of the closed-loop system:

$$Z = P + N \quad (3.18)$$

Where, Z is the number of the RHP zeros of $I + G(j\omega)H(j\omega)$ (i.e. the number of RHP poles of the closed-loop system), P is the number of the RHP poles of $I + G(j\omega)H(j\omega)$ or $G(j\omega)H(j\omega)$ (i.e. the number of the RHP poles of the open-loop system) and N is the number of net encirclement around the origin or the point

$(-1, 0)$. Note that, N is considered positive and negative for clockwise and counter-clockwise encirclement, respectively.

Note that in Equation 3.18, the number of net encirclement can be calculated using GNC or eigenlocus approach. Hence, the number of RHP poles of the closed-loop system (Z) can be determined if the number of the RHP poles of the open-loop system (P) is known. If the open-loop system is unstable, the number of the unstable poles should be known, otherwise applying the stability criterion cannot determine if the closed-loop system is stable.

Note that, when using GNC for the stability analysis of single input single output (SISO) systems, the encirclement of the Nyquist contour $1 + G(j\omega)H(j\omega)$ around the origin is equal to the encirclement of the Nyquist contour $G(j\omega)H(j\omega)$ around the point $(-1, 0)$, since $\det(1 + G(j\omega)H(j\omega)) = 1 + G(j\omega)H(j\omega)$. However, this statement may not be true for the multiple input multiple output (MIMO) systems. When using GNC for the stability analysis of MIMO systems, the encirclement of the Nyquist contour $\det(I + G(j\omega)H(j\omega))$ around the origin is used for stability screening.

If the eigenlocus approach is used for the stability analysis of MIMO systems, it can be shown that the encirclement of an eigenlocus contour of $I + G(j\omega)H(j\omega)$ around the origin is equal to the encirclement of the corresponding eigenlocus contour of $G(j\omega)H(j\omega)$ around the point $(-1, 0)$. In this thesis, for examples using GNC and the eigenlocus approach, the number of net encirclement around the origin and the number of net encirclement around the point $(-1, 0)$, are calculated respectively.

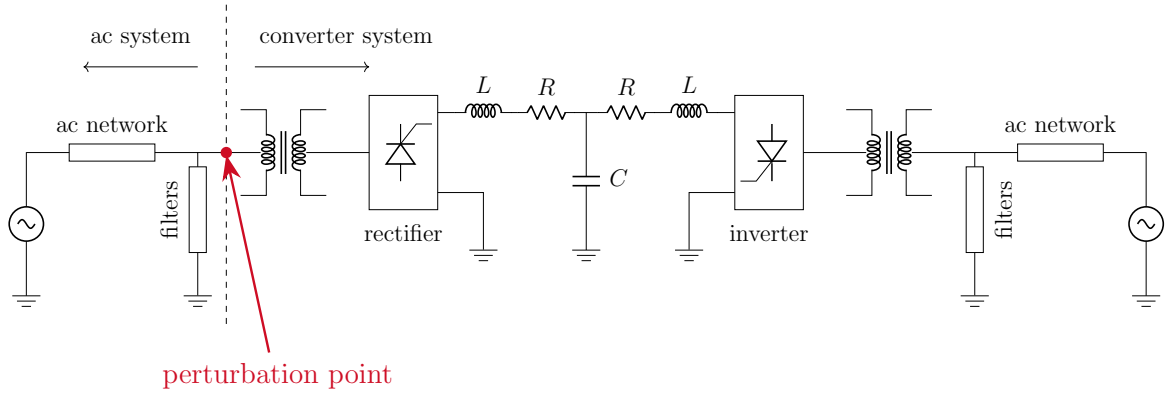
3.7 Case Study: Stability Analysis of the CIGRE-HVDC Benchmark Model

The CIGRE-HVDC benchmark model illustrated in Figure 3.9, is used for stability screening. This model is a monopolar HVDC system, rated at $1000MW$ and operating dc-link voltage of $500kV$. The operating frequency of the rectifier ac network and the inverter ac network is $50Hz$.

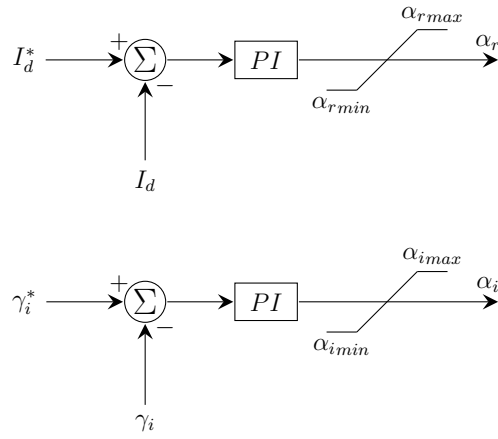
Two cases are created by changing the proportional gain (K_p) of the dc-link current controller at rectifier side. In the first case $K_p = 1.0 \text{ rad/p.u.}$ and in the second case $K_p = 3.0 \text{ rad/p.u.}$ The frequency scanning technique is then used to analyze the adverse interaction between the ac grid and the converter system at the rectifier side.

The impedance matrix of the ac grid ($Z_{grid}(j\omega)$) and the admittance matrix of the HVDC system ($Y_{PES}(j\omega)$) at the rectifier side are required for further analysis of the interactions. To do so, the model of the ac system and the converter system are obtained using DQ-based frequency scanning. After the models are obtained, the stability of the combined system is determined using GNC and the eigenlocus stability approach.

Note that the system under study, is a balanced three-phase system, and the zero sequence can be neglected. Therefore, both $Z_{grid}(j\omega)$ and $Y_{PES}(j\omega)$ are 2×2 matrices for the phase/sequence and the DQ domain models.



(a)



(b)

Figure 3.9: (a) CIGRE-HVDC benchmark model under study (the single phase equivalent circuit) and (b) α controller at the rectifier side and γ controller at the inverter side. Note that subscripts r and i represent the rectifier and the inverter, respectively.

3.7.1 Case 1: Stable Case ($K_p = 1.0 \text{ rad/p.u.}$)

The contour of $\Delta(j\omega)$ for the CIGRE-HVDC system is illustrated in Figure 3.10. The origin of the complex plane is shown with a red dot. Since no encirclement around origin exist, according to GNC, the combined system is stable.

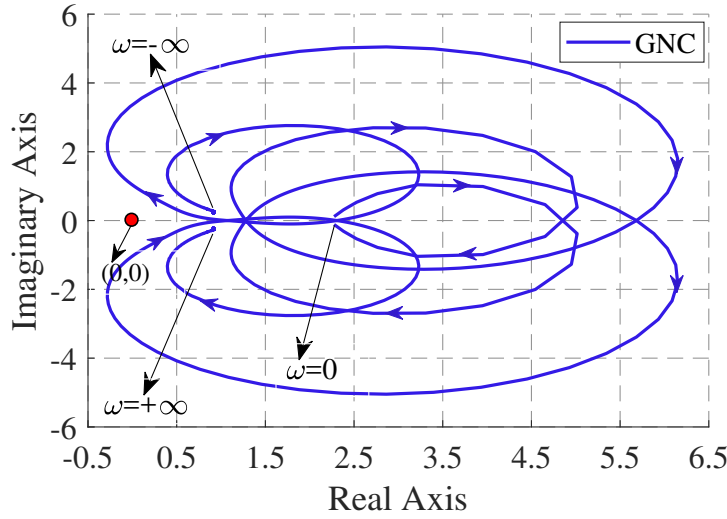
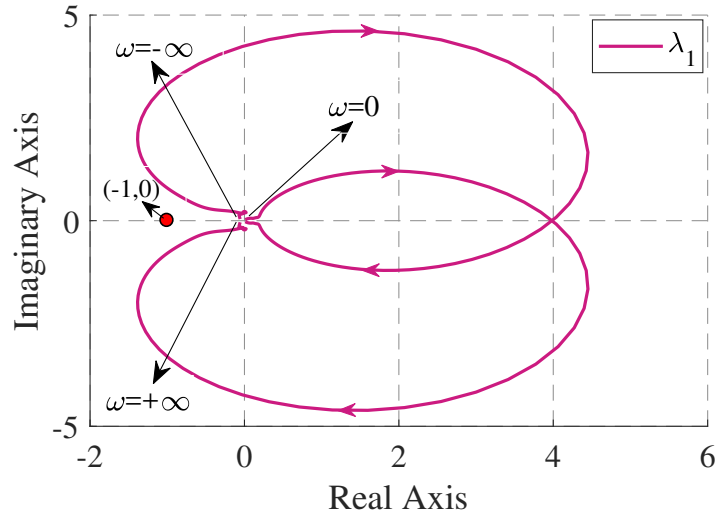
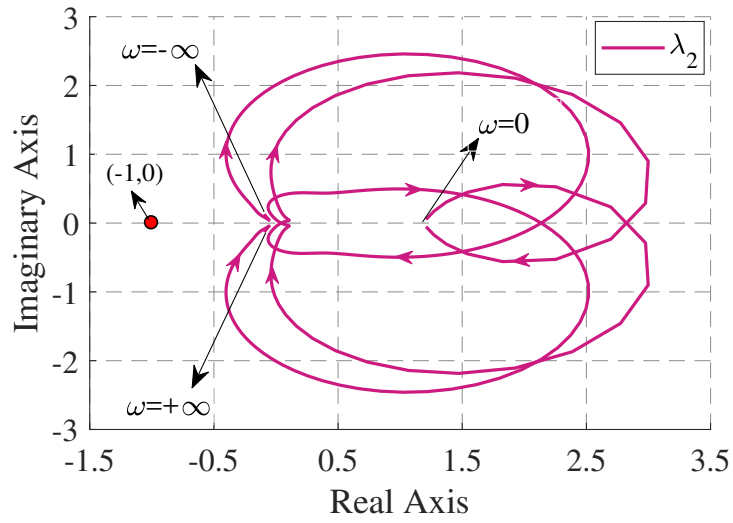


Figure 3.10: Contour of $\Delta(j\omega)$ for the stable case.

As discussed earlier, $Z_{grid}(j\omega)Y_{HVDC}(j\omega)$ can be used for eigenlocus stability approach. The eigen-loci contours ($\lambda_1(j\omega)$ and $\lambda_2(j\omega)$) of $Z_{grid}(j\omega)Y_{HVDC}(j\omega)$ are illustrated in Figure 3.11(a) and Figure 3.11(b) respectively. Since no encirclement of these eigen-loci contours around the origin exists, the combined system is stable.



(a)



(b)

Figure 3.11: Contours of a) $\lambda_1(j\omega)$ and b) $\lambda_2(j\omega)$ for the stable case.

3.7.2 Case 2: Unstable Case ($K_p = 3.0 \text{ rad/p.u.}$)

The contour of $\Delta(j\omega)$ for the CIGRE-HVDC system is illustrated in Figure 3.10. The origin of the complex plain is shown with a red dot. Two clockwise encirclement around origin are observed. Therefore, the combined system is unstable with two unstable poles.

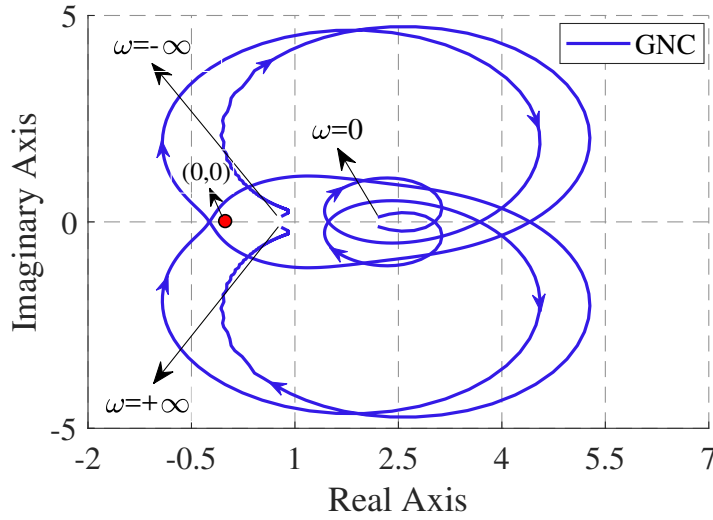
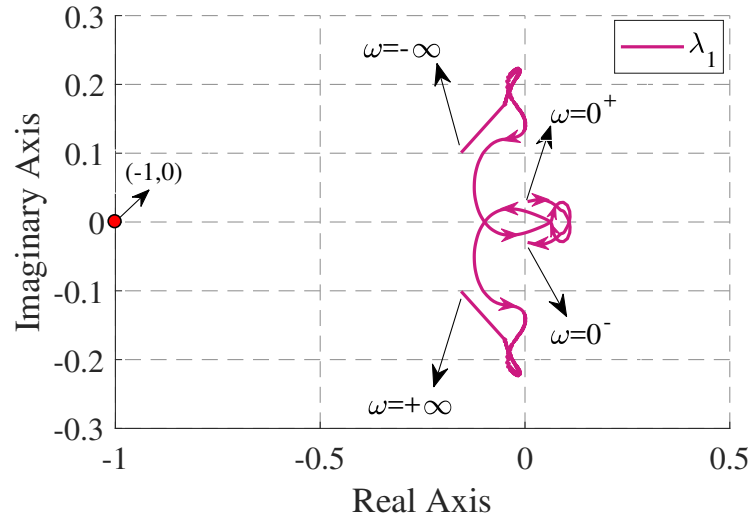
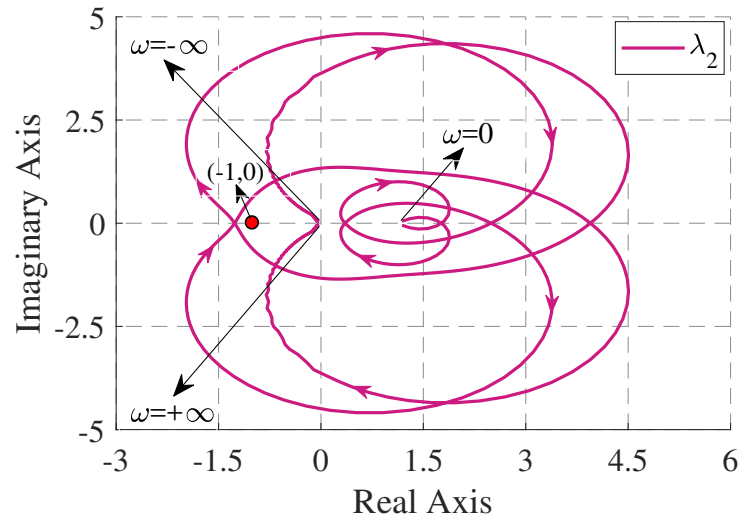


Figure 3.12: Contour of $\Delta(j\omega)$ for the unstable case.

The eigen-loci contours ($\lambda_1(j\omega)$ and $\lambda_2(j\omega)$) of $Z_{grid}(j\omega)Y_{HVDC}(j\omega)$ are illustrated in Figure 3.13(a) and Figure 3.13(b), respectively. No encirclement of $\lambda_1(j\omega)$ around -1 exists whereas, two clockwise encirclement of $\lambda_2(j\omega)$ around -1 are observed. Therefore, the combined system is unstable with two unstable poles.



(a)



(b)

Figure 3.13: Contours of a) $\lambda_1(j\omega)$ and b) $\lambda_2(j\omega)$ for the unstable case.

3.7.3 Validation by EMT Simulation

Figure 3.14 illustrates the EMT simulation result for the dc-link current response. At $t = 3.0 \text{ sec}$, K_p is changed from 1.0 rad/p.u. to 3.0 rad/p.u. and system becomes unstable. Note that the oscillation starts to grow and is limited by control non-linearity.

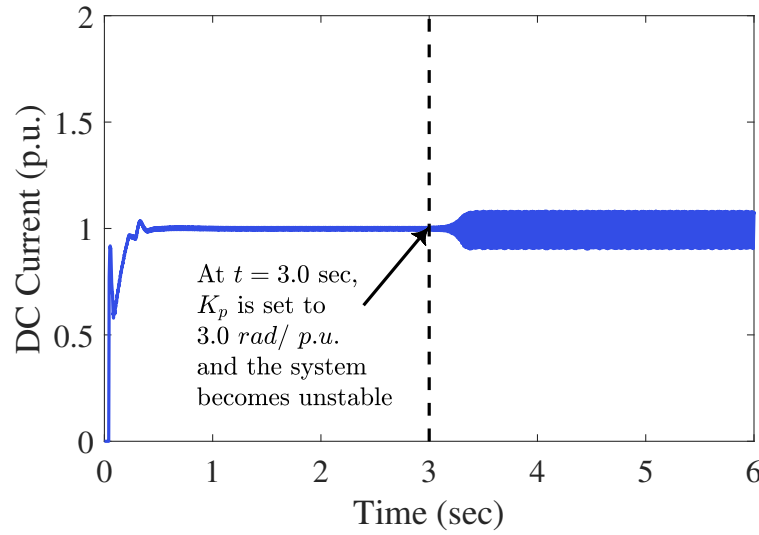


Figure 3.14: The dc-link current response of the HVDC system.

3.8 The Problem of Interchanging Eigenvalues

When calculating the eigenvalues of a system from the frequency scanning results, a sudden change in the eigenvalues which is not acceptable is often observed (because of numerical errors) as illustrated in Figure 3.15. As a result, it is important to keep track of the eigenvalues as the numerical method may make them alternatively [67].

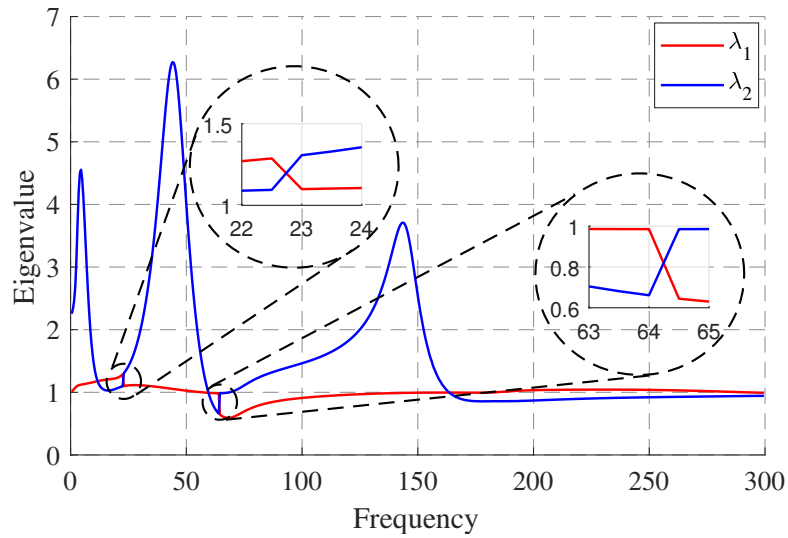


Figure 3.15: Plots of $\lambda_1(j\omega)$ and $\lambda_2(j\omega)$ (for the CIGRE-HVDC system).

To do so, consider the eigenvalues, λ_1 and λ_2 with the corresponding eigen-vectors of \vec{v}_1 and \vec{v}_2 respectively. The eigen-vectors matrix can be defined and calculated for each frequency in the frequency range of interest:

$$V(j\omega) = \begin{bmatrix} v_{11}(j\omega) & v_{12}(j\omega) \\ v_{21}(j\omega) & v_{22}(j\omega) \end{bmatrix} \quad (3.19)$$

Note that $\vec{v}_1(j\omega) = \begin{bmatrix} v_{11}(j\omega) \\ v_{21}(j\omega) \end{bmatrix}$ and $\vec{v}_2(j\omega) = \begin{bmatrix} v_{12}(j\omega) \\ v_{22}(j\omega) \end{bmatrix}$.

In order to examine whether the eigenvalues have been swapped or not in this particular case study, the dot product of one of the eigen-vectors from the current frequency with each of the eigen vectors from the next frequency is calculated and compared. The maximum of these two shows the corresponding eigen-vector (eigenvalue) to the initial eigen-vector(eigenvalue). A partial remedy to determining whether swapping has occurred is mentioned below.

Consider the eigen-vectors at frequency ω_1 and ω_2 as $V(j\omega_1) = \begin{bmatrix} \vec{v}_1(j\omega_1) & \vec{v}_2(j\omega_1) \end{bmatrix}$ and $V(j\omega_2) = \begin{bmatrix} \vec{v}_1(j\omega_2) & \vec{v}_2(j\omega_2) \end{bmatrix}$ respectively. The dot products are calculated as:

$$\begin{aligned} z_1 &= (\vec{v}_1(j\omega_1))^T \cdot \vec{v}_1(j\omega_2) \\ z_2 &= (\vec{v}_2(j\omega_1))^T \cdot \vec{v}_2(j\omega_2) \end{aligned} \tag{3.20}$$

$\max\{z_1, z_2\}$ gives the closest eigen-vector to $\vec{v}_1(j\omega_1)$. If $z_1 > z_2$, then $\vec{v}_1(j\omega_2)$ is the corresponding eigen-vector to $\vec{v}_1(j\omega_1)$, hence no eigenvalue swapping has occurred. In contrast, if $z_2 > z_1$, then $\vec{v}_2(j\omega_2)$ is the corresponding eigen-vector to $\vec{v}_1(j\omega_1)$, hence eigenvalue swapping has occurred and the eigenvalues need to be swapped again to obtain a continuous eigenvalue plot and avoid the eigenvalue swapping error. Figure 3.16 illustrates the eigenvalues of the system, when eigenvalue swapping has been addressed.

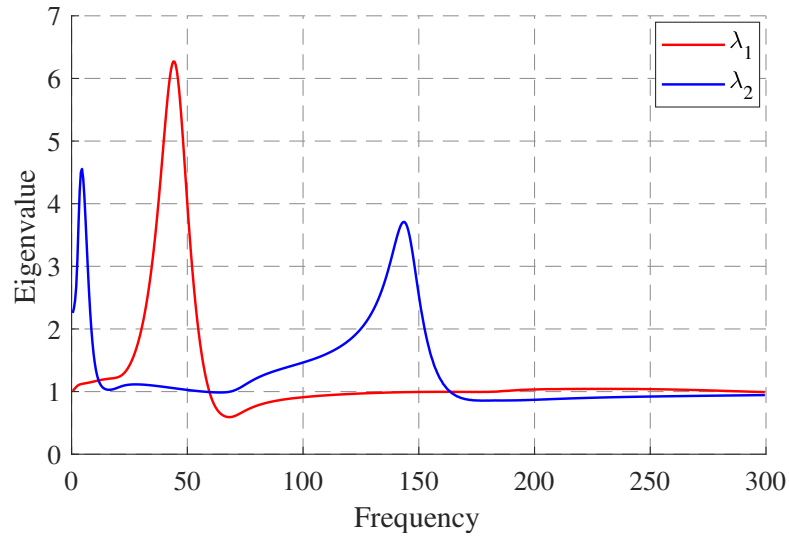


Figure 3.16: Plots of $\lambda_1(j\omega)$ and $\lambda_2(j\omega)$ when considering swapping.

This approach usually works, but it is not foolproof because when the eigenvalues are close to each other, the eigenvectors are close to one another. As a result, it may be difficult to find the closest eigenvector(s) when applying this technique.

3.9 Conclusion

It can be concluded that the stability screening results from GNC and eigenlocus stability approach agree with each other. However there are some benefits and drawbacks when using each method.

1. Encirclement are calculated once for the GNC and twice for two eigenvalues in DQ coordinates in the eigenlocus stability technique. Therefore, requiring more computational power for eigenlocus stability approach is a drawback of using this technique.
2. In the next chapter, we will show that, when dealing with the single input single output (SISO) systems, the GNC calculates the stability margin in terms of gain margin ¹. However, for multiple input and output (MIMO) systems, using the GNC makes stability margin calculations more complicated since matrix multiplication is required. Note that when changing the gain margin (k) using the eigenlocus stability approach, the stability of the new system is calculated by $kG(j\omega)H(j\omega)$. This means that one of the subsystems can be adjusted by factor k . However, when using the GNC, the stability of the new system is calculated by $k|I + G(j\omega)H(j\omega)|$. Here, the determinant makes adjusting the systems more complicated compare to the eigenlocus stability approach. In such circumstances, the stability margin can be determined by using the eigenlocus stability approach [49].

¹The gain margin specifies the factor by which the gain must be increased to bring the system to the brink of instability.

Chapter 4

Frequency Scanning Applications

4.1 Introduction

The frequency scanning results can be used for several purposes. As illustrated in Chapter 3, the frequency scanning results can be used to analyze the stability of the interactions between a Power Electronic System (PES) and the grid. Another example of using the frequency scanning results is finding the stability margin of the Multiple Input Multiple Output (MIMO) systems using the Eigenlocus stability approach. In this chapter, finding the gain margin of a Single Input Single Output (SISO) system using the Nyquist plot is first presented. The gain margin specifies the factor by which the gain must be increased to bring the system to the brink of instability. The gain margin of a MIMO system is then calculated using the individual eigen-loci contours. It is discussed that using the eigenlocus stability approach an unstable eigen locus can be transformed into a stable one. Two case studies are presented to illustrate how the calculated gain margin can play an important role in determining the stability of

the system and how to avoid instabilities.

4.2 Determining the Gain Margin Using Nyquist Stability Approach

As described above, the gain margin is the factor by which the gain must be increased to bring the system to the brink of instability. By obtaining the GNC contour or the eigen-loci contours, the stability of an arbitrary system can be calculated in terms of gain margin.

Consider the closed-loop system illustrated in Figure 4.1 with the gain K and $G(s) = \frac{(s+4)(s+6)}{(s-3)(s-5)}$.

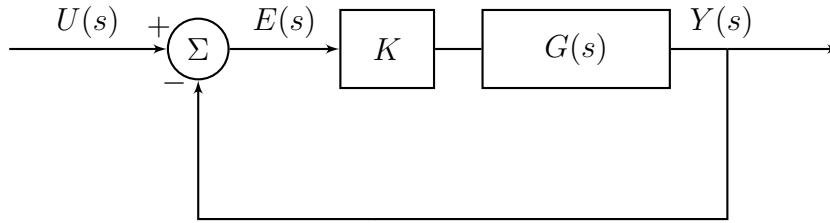


Figure 4.1: The closed-loop model of a system.

The closed-loop transfer function of this system is given by:

$$Tf(s) = \frac{KG(s)}{1 + KG(s)} \quad (4.1)$$

The Nyquist plot of the closed-loop system for $K = 1.0$ is illustrated in Figure 4.2 and can be used for calculating the gain margin of the system.

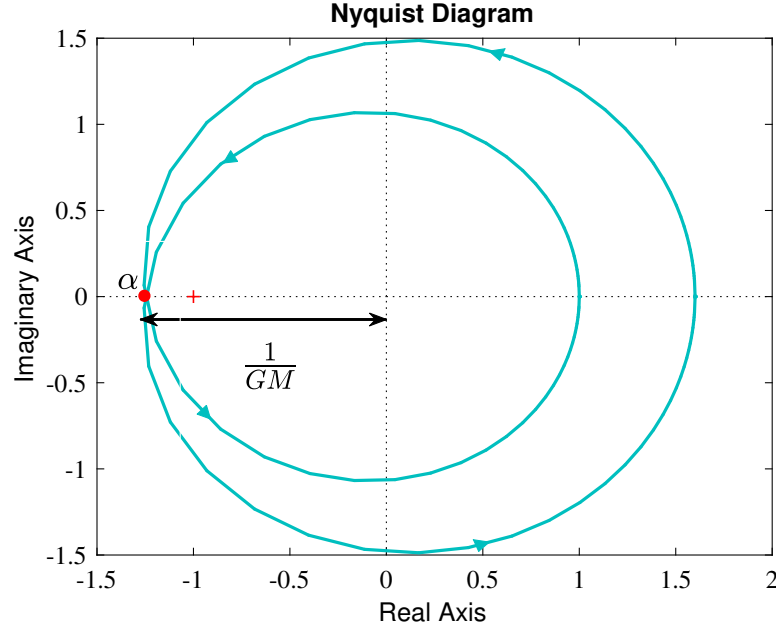


Figure 4.2: The Nyquist plot of the closed-loop system under study for $K = 1.0$.

The gain margin of the system can be calculated using [68]:

$$GM = \frac{1}{|\alpha|} \quad (4.2)$$

In decibels, the gain margin (GM) of a closed-loop system is given by:

$$GM = 20 \log_{10} |\alpha| \quad (4.3)$$

α is a negative point located on the Nyquist contour where it intersects the real axis (i.e., the closed-loop system becomes a purely real number where the phase of this system $\angle Tf(s) = 180^\circ$). Note that, if multiple negative zero-crossings exist on the contours the minimum α is considered for gain margin calculations.

Multiplying the gain of the controller by GM will move the Nyquist contour, so it just encircles $(-1, 0)$, i.e., it brings the system to the brink of instability. Here,

$\alpha = -1.25$ and the gain margin is equal to 0.8. Consequently, if the original gain of the controller (in this case $K = 1.0$) is multiplied by $GM = 0.8$, the point α will become equal to $(-1, 0)$ and the system will be at the brink of instability.

As discussed in Section 3.6, for any arbitrary system, the number of RHP poles of the closed-loop system is given by Z :

$$Z = P + N \quad (4.4)$$

Where P is the number of the RHP poles of the open-loop system, and N is the number of net encirclement around $(-1, 0)$. Note that N is considered positive and negative for clockwise and counterclockwise encirclement, respectively.

Assuming the open-loop system ($G(s)$) has P number of RHP poles, the closed-loop system will be stable if the net counterclockwise encirclements of the Nyquist contour of the system around $(-1, 0)$ is equal to P .

The open-loop transfer function of the system illustrated in Figure 4.1 for the given $G(s)$ is unstable, with two RHP poles at $s = 3$ and $s = 5$. As a result, the closed-loop system will be stable if the Nyquist contour of this system has two counterclockwise encirclements around $(-1, 0)$. Since two counterclockwise encirclements around $(-1, 0)$ are observed in Figure 4.2, the closed-loop system under study is stable for $K = 1.0$.

As mentioned earlier, $\alpha = -1.25$ and the gain margin is equal to 0.8. If the original gain of the controller (in this case $K = 1.0$) is multiplied by any factor smaller than the gain margin (in this case $GM = 0.8$), the point α will become larger than $(-1, 0)$. Note that α is a negative number. In this situation, no encirclements around $(-1, 0)$ exist, thus the system will become unstable. To illustrate this, the

Nyquist plot of the system under study for $K = 0.75$ is illustrated in Figure 4.3. As observed, there are no encirclements around $(-1, 0)$. Therefore, the closed-loop system is unstable with two RHP poles.

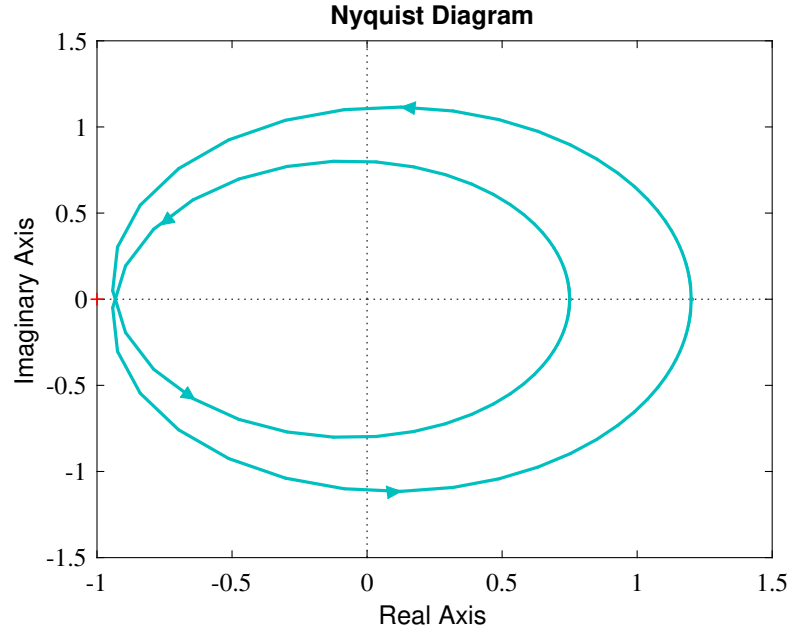


Figure 4.3: The Nyquist plot of the closed-loop system under study for $K = 0.75$.

The step response of the closed-loop transfer function for two gains of $K = 0.75$ and $K = 0.85$ is illustrated in Figure 4.4. From this figure, it is observed that the oscillations are growing for $K = 0.75$ (i.e., the system is unstable), whereas for $K = 0.85$, the oscillations are decaying (i.e., the system is stable), as expected. Note that using Figure 4.4, the frequency of oscillations for $K = 0.75$ and $K = 0.85$ are calculated as $f_{0.75} = 0.6969$ and $f_{0.85} = 0.6930 Hz$, respectively.

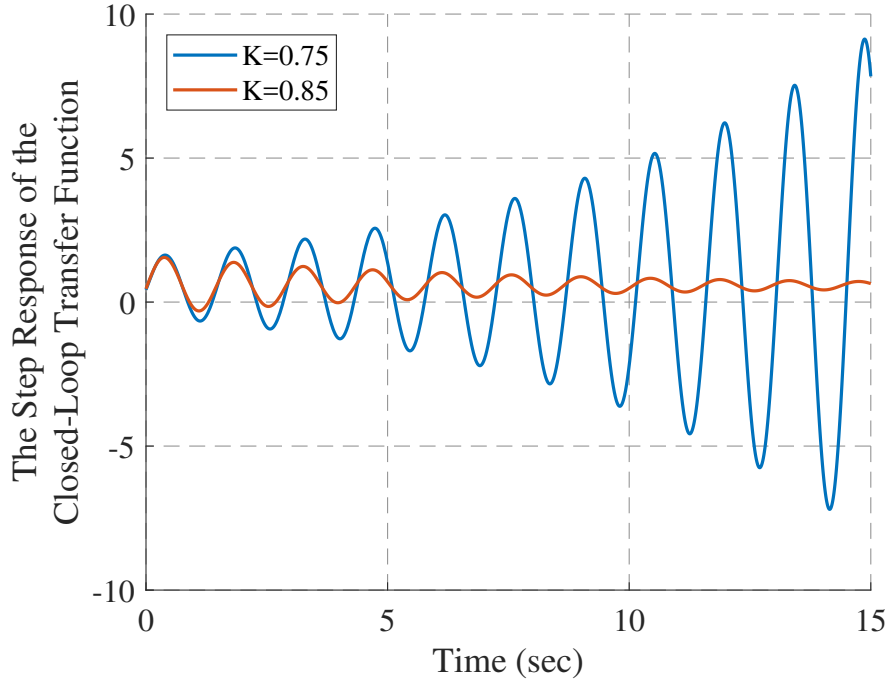


Figure 4.4: The step response of the closed-loop system under study for $K = 0.75$ and $K = 0.85$.

4.3 Finding the Gain Margin Using Eigenlocus Stability Approach

Consider the closed-loop system illustrated in Figure 4.2. As mentioned before, the Eigenlocus Stability Approach requires solving the following equation for this system:

$$\det(\lambda I - D(j\omega)) = 0 \quad (4.5)$$

Where, $D(j\omega) = I + KG(j\omega)$.

The gain margin of the closed-loop system can be calculated using the same technique illustrated in Section 4.2. It should be noticed that, since the closed-loop system has two individual eigen-loci, two gain margins are obtained. The gain margin of the closed-loop system is considered to be the maximum of these two gain margins.

Note that the gain margin here not only gives an idea of how much the gain can be increased but also defines the frequency of oscillations that would arise as a consequence of increasing the gain to this limit. Next, a case study is presented to investigate the stability of a system using the eigenlocus stability approach.

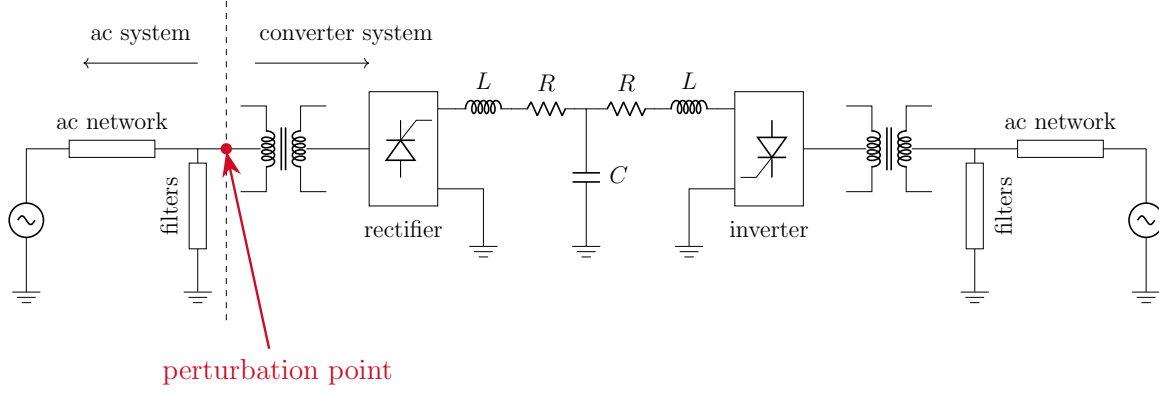
4.4 Case Study : Gain Margin Calculations for the CIGRE-HVDC Benchmark Model

The same HVDC system in Chapter 3, the CIGRE-HVDC benchmark model illustrated in Figure 4.5, is used for stability screening. This monopolar HVDC system is rated at $1000MW$ and has an operating dc-link voltage of $500kV$. The operating frequency of the rectifier ac network and the inverter ac network is $50Hz$.

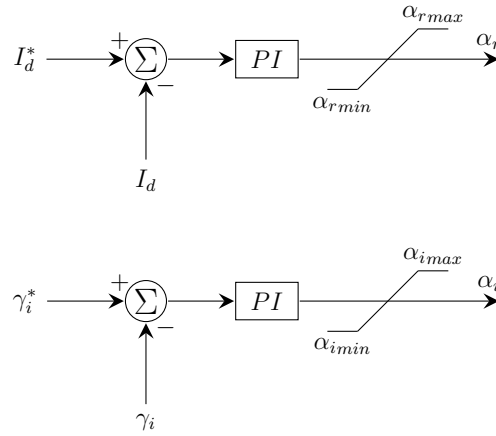
As discussed in Chapter 3, changing the proportional gain (K_p) of the dc-link current controller at the rectifier side can affect the stability of the system. It was observed that for the system was stable for $K_p = 1.0 \text{ rad/p.u.}$ and unstable for $K_p = 3.0 \text{ rad/p.u.}$ In this section, two cases are studied:

1. Case 1: Finding the maximum K_p for a stable system.
2. Case 2: Studying the impact of the strength of the ac system on stability.

For both cases, the frequency scanning technique is used to analyze the adverse interaction between the ac grid and the converter system at the rectifier side.



(a)



(b)

Figure 4.5: (a) CIGRE-HVDC benchmark model under study (the single phase equivalent circuit) and (b) α controller at the rectifier side and γ controller at the inverter side. Note that subscripts r and i represent the rectifier and the inverter, respectively.

4.4.1 Case 1: Finding the Maximum K_p for a Stable System

The frequency response of the HVDC system and the grid are obtained using DQ-based frequency scanning. By plotting the GNC for other values of K_p , it was determined that the system would be stable for $K_p < 2.4 \text{ rad/p.u.}$.

As illustrated in Figure 4.6, at $t = 3 \text{ sec}$, K_p is increased from 1.0 rad/p.u. to 3.0 rad/p.u. , and the system becomes unstable. Note that oscillation starts but is limited due to controller nonlinearities. At $t = 6 \text{ sec}$, this gain is set to 2.2 rad/p.u. (i.e., $< 2.4 \text{ rad/p.u.}$) and the system goes back to a stable state.

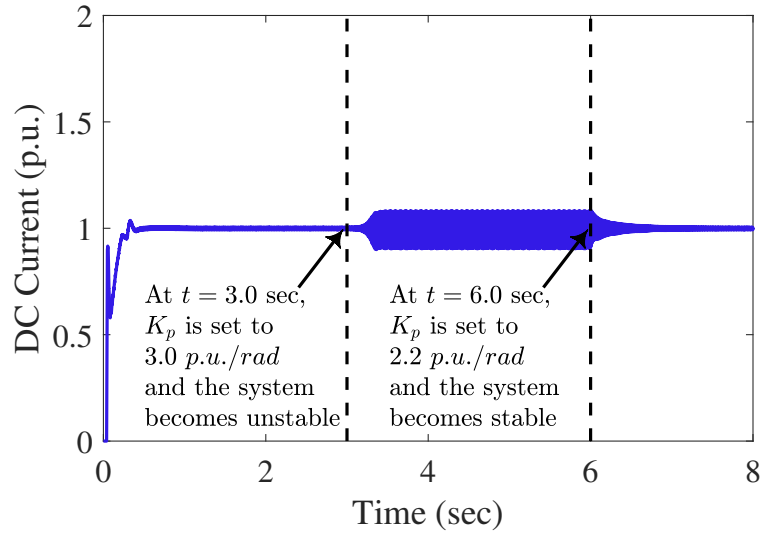


Figure 4.6: The dc-link current response of the HVDC system.

The unstable period of the signal shown in Figure 4.6 has an oscillation frequency of $f = 66.67 \text{ Hz}$, as illustrated in Figure 4.7.

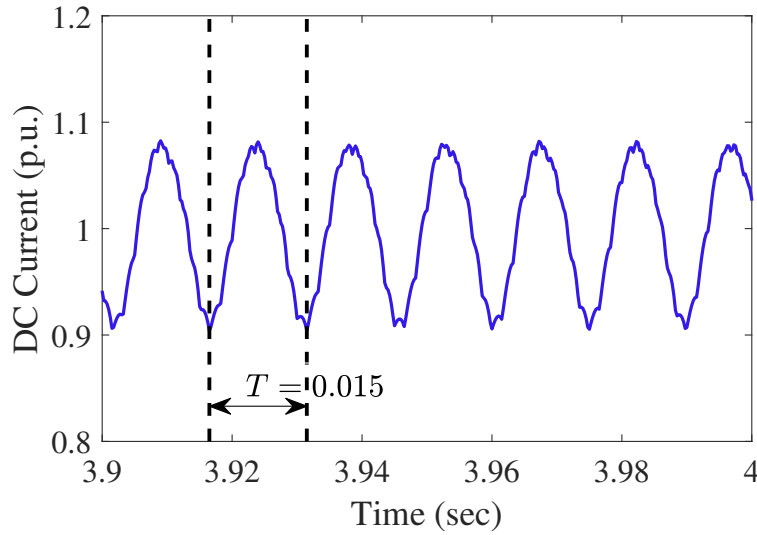


Figure 4.7: The dc-link current response of the HVDC system (Zoomed in).

In the eigenlocus based Nyquist plot, the frequency of oscillation at the critical point can be approximately determined by the value of ω at which the eigenlocus contour crossed the negative real axis. In this case, it is $f = 68\text{ Hz}$ or $\omega = 2\pi f = 408.41\text{ rad/s}$, as illustrated in Figure 4.8. It is observed that this frequency matches closely with the frequency obtained from Figure 4.6.

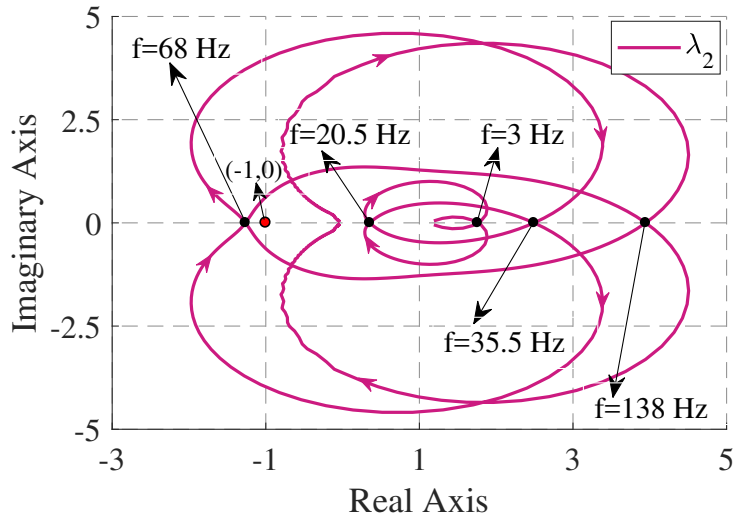


Figure 4.8: Frequency of the points where the counter of one eigenlocus of the unstable case crosses the real axis.

4.4.2 Case 2: The Impact of AC System Strength on the Stability

In this section, it is shown how the stability is impacted by the ac grid admittance/impedance. Note that from Equation 3.2, the loop gain is $Z_{grid}(j\omega)Y_{PES}(j\omega)$. Decreasing K_p to below 2.4 rad/p.u. affects $Y_{PES}(j\omega)$ and makes the system stable. However, keeping K_p constant and decreasing $Z_{grid}(j\omega)$ has the same effect on stability, which will be demonstrated in the example of this section.

Figure 4.9 shows one eigenlocus of the unstable case with $K_p = 3.0 \text{ rad/p.u.}$ for the CIGRE-HVDC Benchmark Model illustrated in Figure 4.5. From the figure, it is observed that the distance d from the point $(-1, 0)$ is equal to 0.25 (i.e., $\alpha = 1.25$), and hence the gain margin is 0.8.

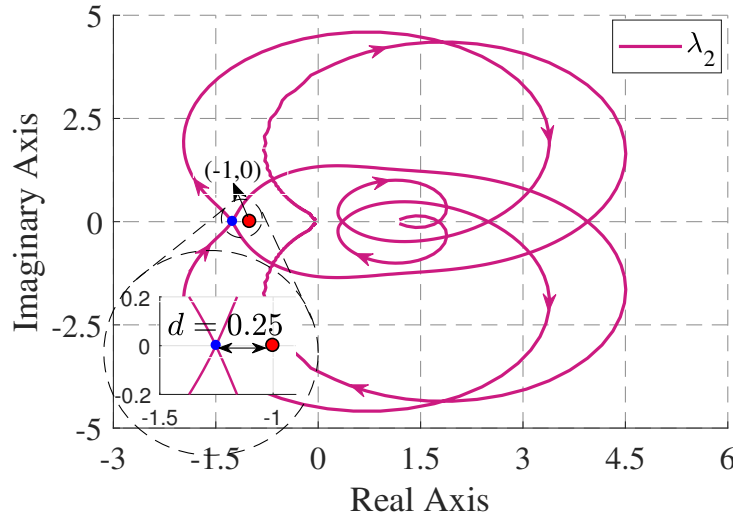


Figure 4.9: One eigenlocus of the unstable case with the original ac grid.

As a result, decreasing $Z_{grid}(j\omega)$ by a factor of 0.8 should make the system stable. Following the discussion of gain margin in Section 4.2, and with $G(j\omega) = Z_{grid}(j\omega)Y_{PES}(j\omega)$, decreasing K by a factor of GM is equivalent to decreasing $Z_{grid}(j\omega)$ by the same factor. Hence if the system impedance is smaller by the factor GM , the system will be stable.

Equation 4.6 shows the definition of the Short Circuit Ratio (SCR) [69], from which it is clear that scaling Z_{grid} by R is tantamount to scaling SCR by $\frac{1}{R}$ [49].

$$SCR = \frac{V_{ac}^2}{P_{dc}|Z_{grid}|} \quad (4.6)$$

Note that, in the HVDC system illustrated in Figure 4.5, the original SCR was 2.5. Assuming $K_p = 3.0 \text{ rad/s}$ and constant, to make the unstable system stable, the SCR should be larger than $\frac{2.5}{0.8} = 3.125$.

As illustrated in Figure 4.9, for $K_p = 3.0 \text{ rad/p.u.}$ the system is unstable, and the gain margin of the closed-loop system is calculated as 0.8. Setting $K_p = 2.4 \text{ rad/p.u.}$ or less will stabilize the system as in the previous case study. Alternatively, we may achieve a stable response by scaling the impedance of the ac network (i.e., changing the SCR).

Figure 4.10 illustrates the same eigenlocus, where the network impedance is scaled by the factor of 0.71 (i.e., < 0.8), which is stable as the point $(-1, 0)$ is not inside the locus.

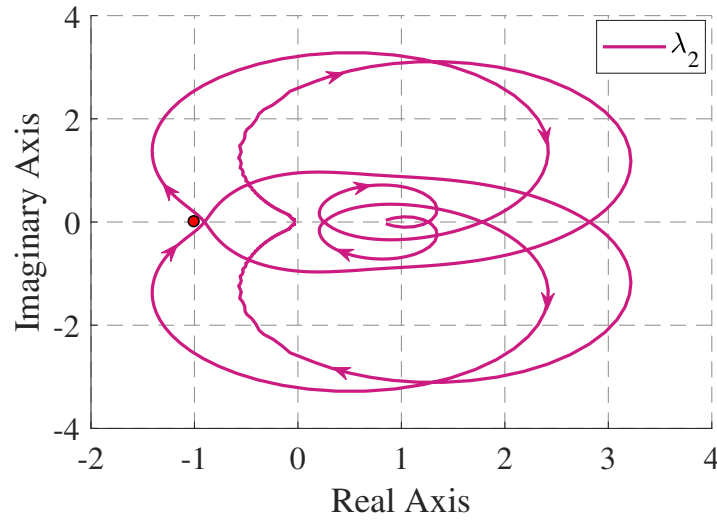


Figure 4.10: One eigenlocus of the stabilized case with the modified ac grid.

Figure 4.11, shows the EMT simulation of the CIGRE-HVDC Benchmark Model where the network impedance is scaled by the factor of 0.71 (i.e. SCR is changed to $\frac{2.5}{0.71} = 3.521$).

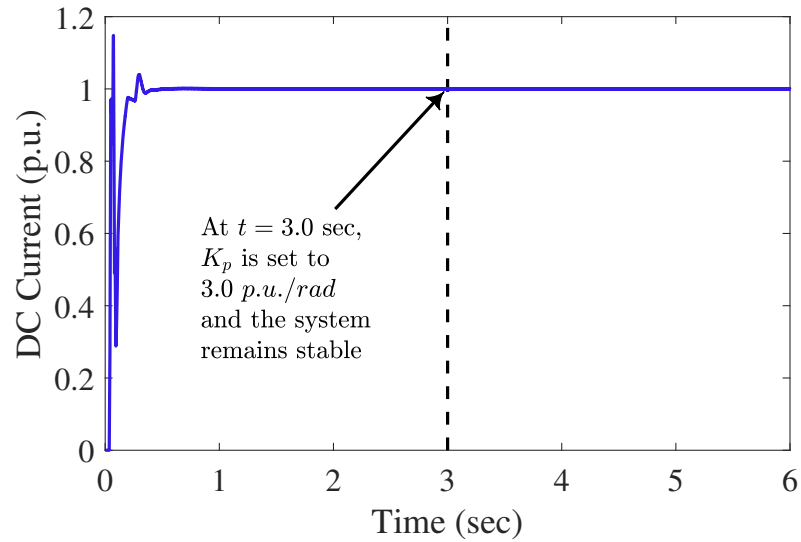


Figure 4.11: The dc-link current response of the HVDC system with scaled ac grid.

From the figure, it can be observed that the system remains stable when K_p changes from 1.0 *rad/p.u.* to 3.0 *rad/p.u.* at 3.0 *sec*, which would have caused instability with the original unscaled network impedance.

4.5 Conclusion

In this chapter, it was discussed that the Nyquist contour and the Eigenloci contours could be used to calculate the gain margin of a system. Moreover:

1. The eigenlocus stability approach gives additional information on the frequency of oscillation in the instability.
2. The gain margin can be obtained from the eigen-loci contours and used for scaling the gain K_p of the controller.
3. The strength of the ac grid defined by the SCR, impacts the stability of the system. Decreasing the ac system impedance by the factor GM can make the system stable.

Chapter 5

Grid Interaction Studies Using Sequence Domain Impedance/Admittance

5.1 Introduction

Many researchers continue to use positive/negative sequence domain analysis to investigate converter stability. In this chapter, we explore this approach and show that it can yield approximate results regarding stability. It also has the same numerical complexity as the DQ-based method discussed in Chapter 3 and Chapter 4. However, it is shown in this chapter that this approach may sometimes conclude that the system is stable when, in reality, it may not be (or vice versa). Hence this thesis discourages its use. In this technique, the sequence domain model is used for stability analysis. Two independent positive/negative sequence subsystems are obtained from

the original system. After the positive/negative sequence models of PES and grid are calculated, the approximate screening criteria are applied to check the stability of the system. Two stable and unstable interactions are simulated to validate the results from the stability screening criteria. A comparison between the Nyquist stability criterion used in Chapter 3 and the approximation stability screening technique is provided at the end of the chapter.

5.2 Stability Screening Using the Net Sequence Admittance

Consider the grid-connected PES is illustrated in Figure 5.1.

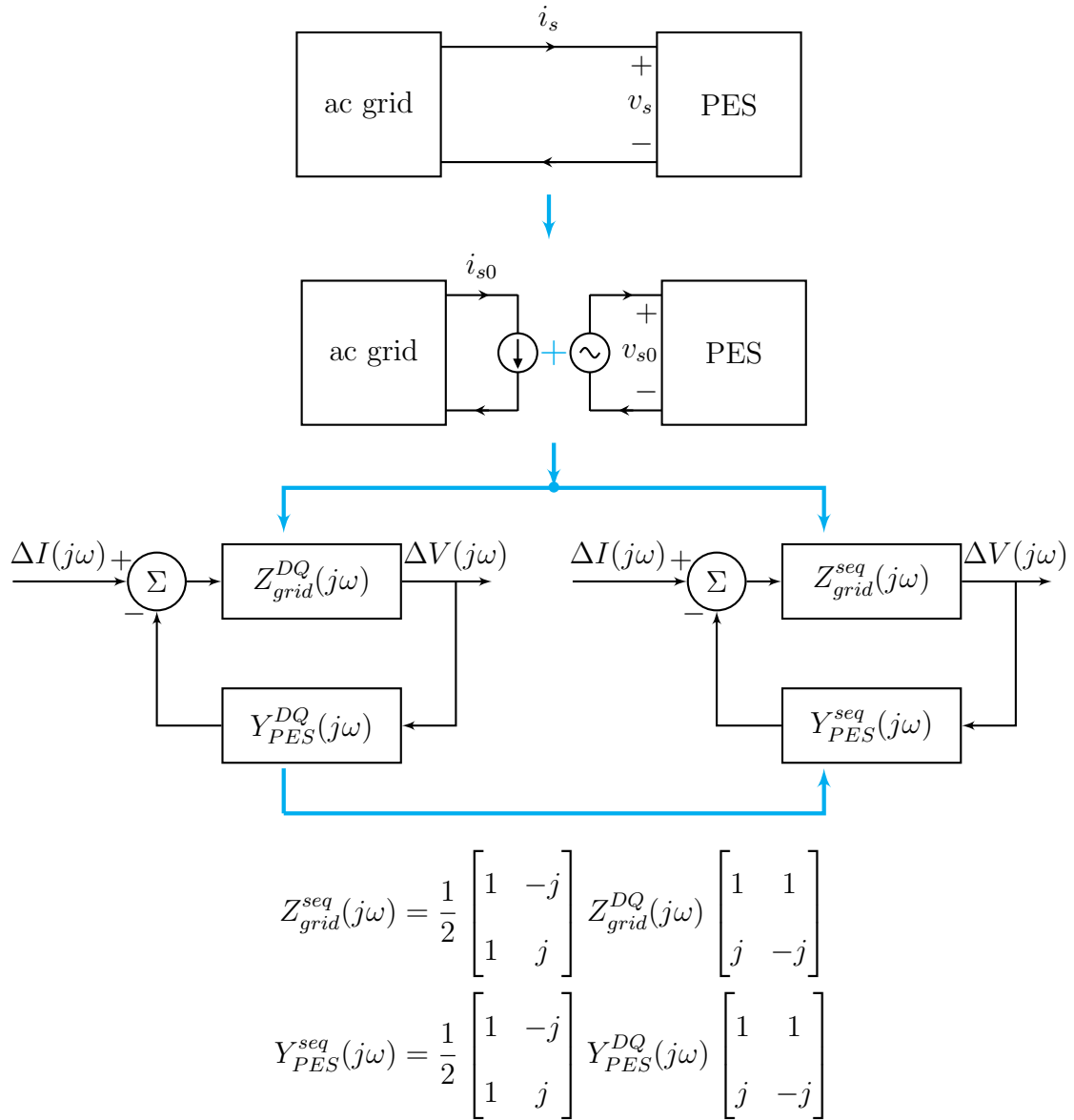


Figure 5.1: Derivation of the sequence model for the grid-connected PES.

$Z_{grid}^{seq}(j\omega)$ and $Y_{PES}^{seq}(j\omega)$ are the sequence impedance of the ac grid and the sequence admittance of the PES, respectively. These matrices are obtained using the DQ-based frequency scanning and applying the transformation matrix given in Section 2.9.4 and Equation 2.26 to get the sequence impedance/admittance. Note that the sequence domain matrices can also be obtained using the sequence-based frequency scanning technique. However, frequency interference may exist, and therefore, multiple scans can be performed by dividing the scan range into smaller ranges.

One may ask why to bother going through the DQ-based frequency scanning and not generate the sequence models $Z_{grid}^{seq}(j\omega)$ or $Y_{PES}^{seq}(j\omega)$ directly. The reader is pointed in Section 2.7.4, frequency interference may occur, requiring the scan to be done in various ranges of frequency separately. As shown in Section 2.9.3, scanning in the DQ domain does not result in frequency interference, and hence is recommended as an intermediate step even when generating the sequence impedance/admittance scan. Consequently, the stability criterion which was applied to the DQ-based frequency scanning results can be applied to the obtained sequence model as well.

The closed-loop transfer function of the overall system illustrated in Figure 5.1 is given by:

$$T_1(j\omega) = \left(I + Z_{grid}^{seq}(j\omega)Y_{PES}^{seq}(j\omega) \right)^{-1} Z_{grid}^{seq}(j\omega) \quad (5.1)$$

Since $Z_{grid}^{seq}(j\omega)$ is a passive system, $(Z_{grid}^{seq}(j\omega))^{-1}$ is stable and this transfer function can be written as:

$$T_1(j\omega) = \left((Z_{grid}^{seq}(j\omega))^{-1} + Y_{PES}^{seq}(j\omega) \right)^{-1} \quad (5.2)$$

Consider $\Delta(j\omega)$ as:

$$\Delta(j\omega) = \det\left((Z_{grid}^{seq}(j\omega))^{-1} + Y_{PES}^{seq}(j\omega)\right) \quad (5.3)$$

According to GNC discussed in section 3.4, if the open-loop system is stable (i.e., $Z_{grid}^{seq}(j\omega)Y_{PES}^{seq}(j\omega)$ is stable) and the contour of $\Delta(j\omega)$ has n encirclement around the origin of the complex plane, the transfer function of the closed-loop system will have n poles in the right hand of the complex plane. Hence the overall closed-loop system is unstable with n unstable poles.

It is important to highlight that if the contour of $\Delta(j\omega)$ has any net encirclement around the origin (i.e., the system is unstable), it indicates that $\Delta(j\omega)$ has at least one more zero crossing on the left-hand side than on the right-hand side of the real axis. Whereas, if the contour of $\Delta(j\omega)$ has no net encirclement around the origin, there will be no zero crossings on the left-hand side of the real axis or there will be equal zero crossings on the left-hand side and the right-hand side of the real axis. As a result, for any arbitrary frequency, if the imaginary part $\Im(\Delta(j\omega)) = 0$, then the system is stable if the real part $\Re(\Delta(j\omega)) > 0$ at the same frequency. As will be shown, this criteria is not always correct but could be used as a screening technique for anticipating the stability of the interactions in a grid-connected PES [27].

The impedance or admittance matrix of a balanced three-phase ac network ($Z_{grid}^{seq}(j\omega)$) at any frequency ω , is assumed to be a diagonal matrix, although there is coupling of $Z_+(\omega)$ to $Z_-(\omega - 2\omega_0)$. Here, it is assumed that there is no coupling between the positive/negative sequences in the network (i.e., $Z_{grid_{pn}}(j\omega) = Z_{grid_{np}}(j\omega) = 0$). This property of the passive ac networks is the reason for choosing the sequence impedance over the dq impedance for stability screening. On the contrary, the PES

is not a passive system, which means the off-diagonal elements exist. In this situation, if the off-diagonal elements of $Y_{PES}^{seq}(j\omega)$ are much smaller compared to the diagonal elements, $Y_{PES}^{seq}(j\omega)$ could be approximated as a diagonal matrix, as illustrated in Figure 5.2. As a result, the stability screening criteria is an approximation method.

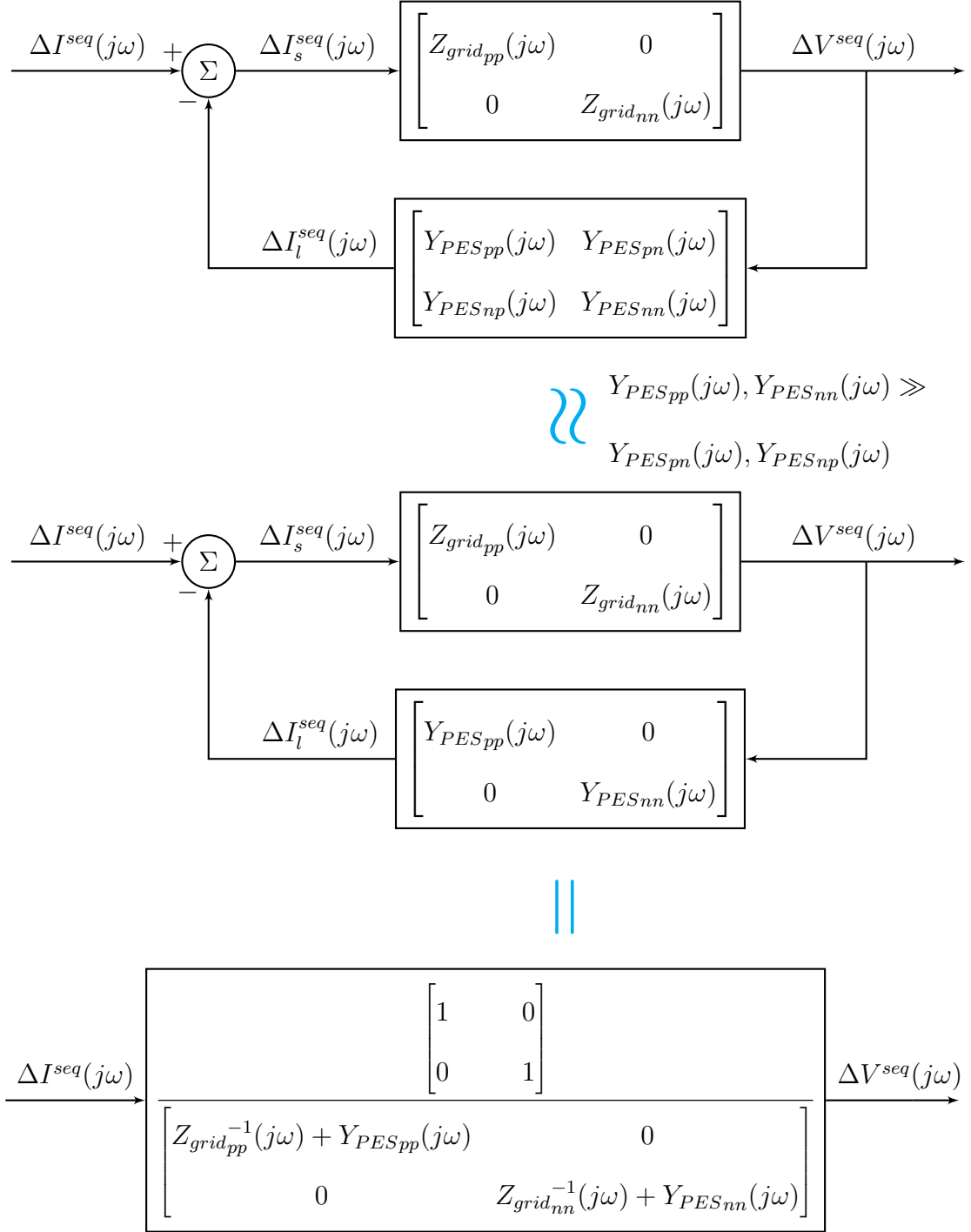


Figure 5.2: The closed-loop transfer function of the overall system

Considering the approximation illustrated in Figure 5.2, $\Delta(j\omega)$ can be simplified as:

$$\Delta(j\omega) = \left(Z_{grid_{pp}}^{-1}(j\omega) + Y_{PES_{pp}}(j\omega) \right) \left(Z_{grid_{nn}}^{-1}(j\omega) + Y_{PES_{nn}}(j\omega) \right) \quad (5.4)$$

From this equation, it can be observed that the overall system has been divided into two independent positive/negative sequence subsystems. $\Delta(j\omega)$ is the product of two terms, where each term represents a SISO subsystem. Similar to stability screening using the individual eigen-loci, discussed in Section 3.5, the total encirclement of $\Delta(j\omega)$ around the origin is equal to the sum of the encirclement of each term.

The positive/negative sequences can be separated for stability screening, using Equation 5.4. Consequently, if the condition for instability occurs in either positive or negative sequences, the system could be at the risk of instability.

If the following conditions are satisfied for a given frequency such as ω_0 , then the system is deemed to be unstable:

$$\begin{aligned} \Im \left((Z_{grid_{pp}}^{-1}(j\omega_0)) + Y_{PES_{pp}}(j\omega_0) \right) &= 0 \quad \text{and} \\ \Re \left((Z_{grid_{pp}}^{-1}(j\omega_0)) + Y_{PES_{pp}}(j\omega_0) \right) &< 0 \end{aligned} \quad (5.5)$$

or,

$$\begin{aligned} \Im \left((Z_{grid_{nn}}^{-1}(j\omega_0)) + Y_{PES_{nn}}(j\omega_0) \right) &= 0 \quad \text{and} \\ \Re \left((Z_{grid_{nn}}^{-1}(j\omega_0)) + Y_{PES_{nn}}(j\omega_0) \right) &< 0 \end{aligned} \quad (5.6)$$

Note that \Re and \Im denote the real part and the imaginary part, respectively.

It will be shown that although the above criteria work well in most cases, they are not actually correct. Hence, at the best, they should only be used for screening rather than for precise determination of stability. For precise determination of stability, further detailed simulation may be required.

The above conclusion is rationalized as follows:

For any passive ac network, $\Re(Z_{grid_{pp}}^{-1})$ and $\Re(Z_{grid_{nn}}^{-1})$ are positive at all frequencies. On the contrary, the PES is not a passive system, which results in $\Re(Y_{PES_{pp}})$ and $\Re(Y_{PES_{nn}})$ becoming positive or negative at different frequencies. Consequently, $\Re\left((Z_{grid_{pp}}(j\omega_0))^{-1} + Y_{PES_{pp}}(j\omega_0)\right)$ can become negative at certain frequencies, if $\Re(Y_{PES_{pp}}(j\omega_0))$ is negative and has a magnitude higher than $\Re(Z_{grid_{pp}}^{-1}(j\omega_0))$. Note, the same condition can occur in the negative sequence as well.

To prevent such instabilities, the controllers could be designed so that $\Re(Y_{PES_{pp}})$ and $\Re(Y_{PES_{nn}})$ are positive at all frequencies. As a result, both real parts of $Z_{grid_{pp}}^{-1}(j\omega) + Y_{PES_{pp}}(j\omega)$ and $Z_{grid_{nn}}^{-1}(j\omega) + Y_{PES_{nn}}(j\omega)$ are positive at all frequencies, which makes the system is less prone to instabilities. Next, two case studies are presented to analyze the stability of a grid-connected PES via approximate stability screening using the net sequence admittance.

5.3 Case Study: CIGRE-HVDC Benchmark Model

Stability Screening Using the Net Sequence Admittance

The same HVDC system in Chapter 3, the CIGRE-HVDC benchmark model illustrated in Figure 5.3, is used for approximate stability screening using the net sequence admittance. This monopolar HVDC system is rated at $1000MW$ and has an operating dc-link voltage of $500kV$. The operating frequency of the rectifier ac network and the inverter ac network is $50Hz$.

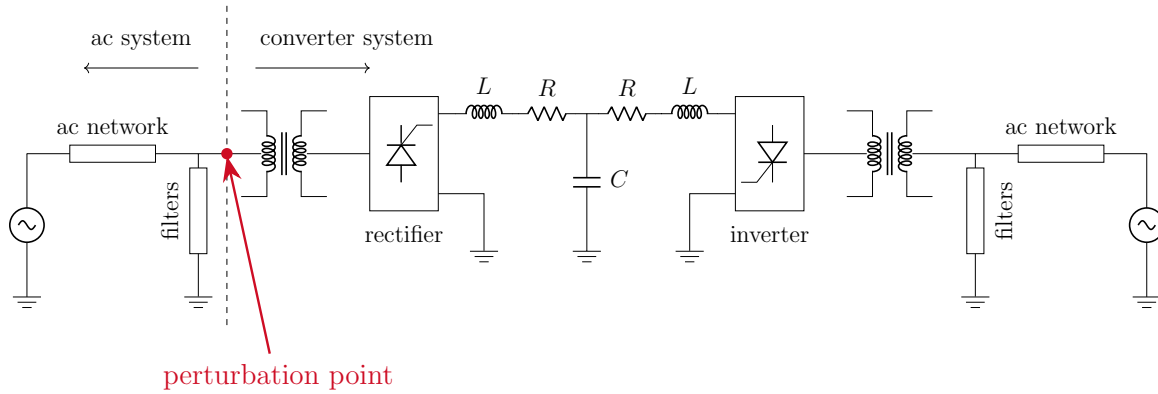


Figure 5.3: CIGRE-HVDC benchmark model under study (the single phase equivalent circuit).

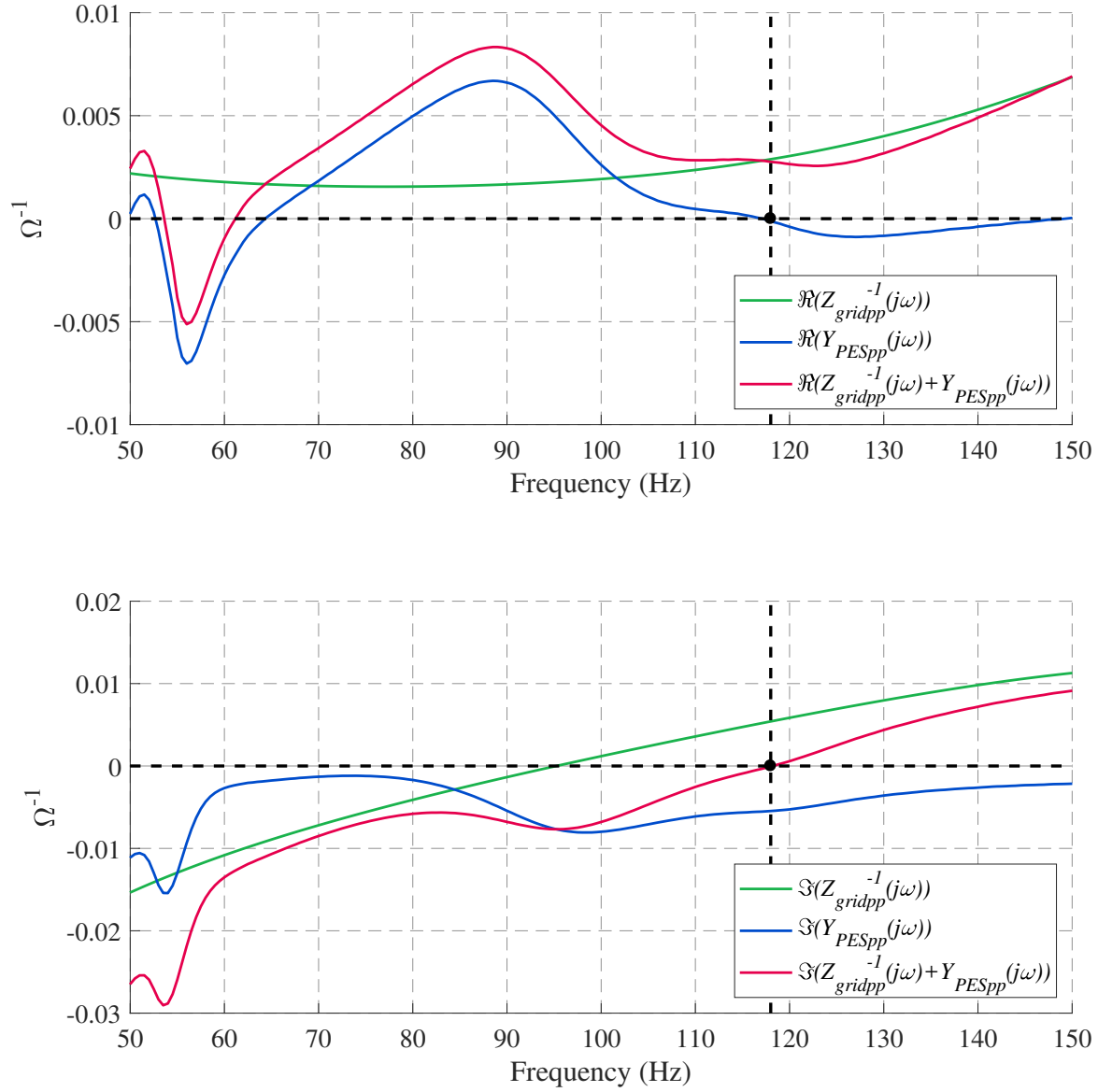
Two cases are created by changing the proportional gain (K_p) of the dc-link current controller at rectifier side. In the first case $K_p = 1.0 \text{ rad/p.u.}$ and in the second case $K_p = 3.0 \text{ rad/p.u.}$ The real and imaginary parts of $(Z_{grid}^{seq}(j\omega))^{-1} + Y_{PES}^{seq}(j\omega)$ are used to determine the stability of interaction between the ac grid and the converter system at the rectifier side.

For this purpose, the sequence impedance matrix of the ac grid ($Z_{grid}^{seq}(j\omega)$) and

the sequence admittance matrix of the HVDC system ($Y_{PES}^{seq}(j\omega)$) at the rectifier side are obtained by frequency scanning. After these models are obtained, the stability of the combined system is determined using the criteria given in Equations 5.5 and 5.6.

5.3.1 Case 1: Stable Case ($K_p = 1.0 \text{ rad/p.u.}$)

The real and imaginary parts of $Z_{grid_{pp}}^{-1}(j\omega) + Y_{PES_{pp}}(j\omega)$ for positive sequence are illustrated in Figure 5.4. From this figure, it is observed that $\Im(Z_{grid_{pp}}^{-1}(j\omega) + Y_{PES_{pp}}(j\omega)) = 0$ at frequency $f = 118Hz$. Next the value of $\Re(Z_{grid_{pp}}^{-1}(j\omega) + Y_{PES_{pp}}(j\omega))$ should be determined at this frequency. At $f = 118Hz$, the real part of $Y_{PES_{pp}}(j\omega)$ is negative. However, it is not adequate to overcome the positive value of $Z_{grid_{pp}}^{-1}(j\omega)$ at this frequency. Consequently, the overall sequence admittance is positive at $f = 118Hz$. Next, the same procedure should be applied for negative sequence to check whether the conditions for instability occur.

Figure 5.4: The real and imaginary parts of $Z_{gridpp}^{-1}(j\omega) + Y_{PESpp}(j\omega)$.

The real and imaginary parts of $Z_{grid_{nn}}^{-1}(j\omega) + Y_{PES_{nn}}(j\omega)$ for negative sequence are illustrated in Figure 5.5. It is observed that $\Im(Z_{grid_{nn}}^{-1}(j\omega) + Y_{PES_{nn}}(j\omega)) = 0$ at frequency $f = 111Hz$. Since both $Y_{PES_{pp}}(j\omega)$ and $Z_{grid_{pp}}^{-1}(j\omega)$ are positive at $f = 111Hz$, the overall negative sequence admittance is positive at this frequency.

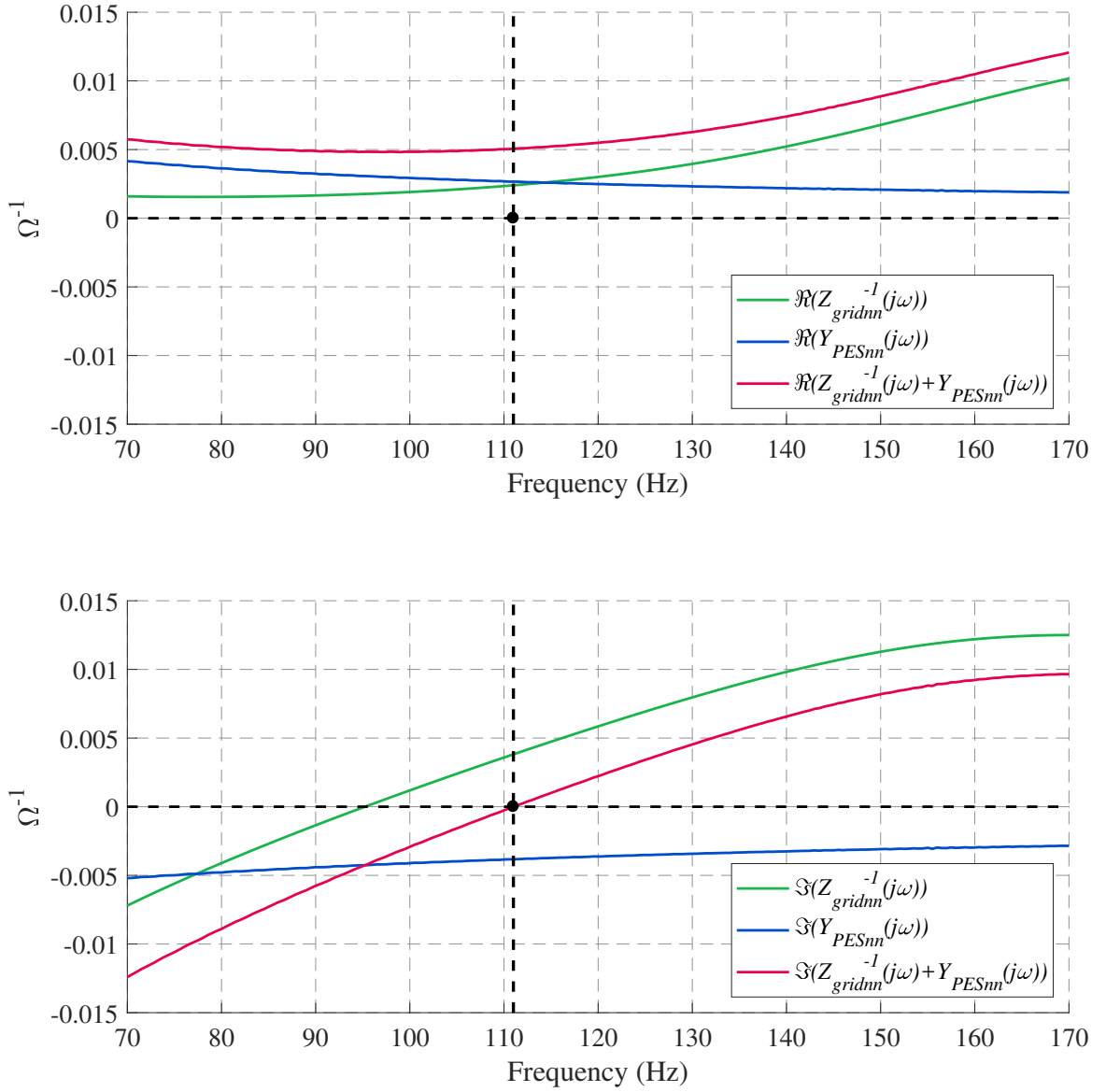


Figure 5.5: The real and imaginary parts of $Z_{grid_{nn}}^{-1}(j\omega) + Y_{PES_{nn}}(j\omega)$ at $f = 111Hz$.

Since neither of the conditions for instability occurs in positive or negative sequences, this system is regarded as to not be at a risk of instability, which agrees with the dc-link current response of the stable case illustrated in Figure 5.6.

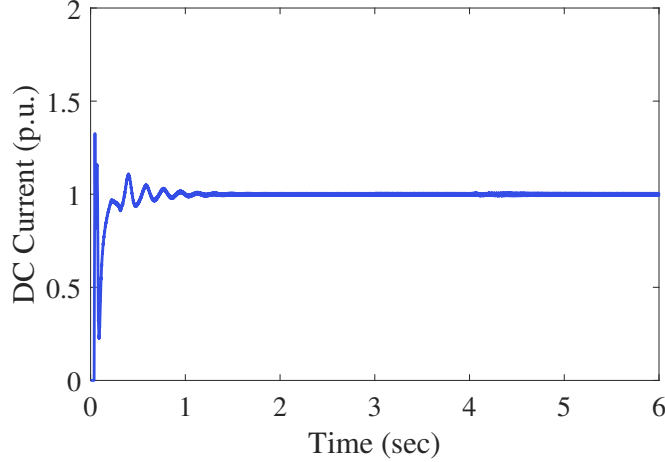


Figure 5.6: The dc-link current response for the stable case.

5.3.2 Case 2: Unstable Case ($K_p = 3.0 \text{ rad/p.u.}$)

Similar to Chapter 3, the proportional gain (K_p) of the dc-link current controller is changed from $K_p = 1.0 \text{ rad/p.u.}$ to $K_p = 3.0 \text{ rad/p.u.}$ at $t = 3.0 \text{ sec.}$

The real and imaginary parts of $Z_{grid_{pp}}^{-1}(j\omega) + Y_{PES_{pp}}(j\omega)$ for positive sequence are illustrated in Figure 5.7. From this figure, it is observed that $\Im(Z_{grid_{pp}}^{-1}(j\omega) + Y_{PES_{pp}}(j\omega)) = 0$ at frequency $f = 125\text{Hz}$. By similar reasoning to the previous case, it can be seen that the overall positive sequence admittance is negative at $f = 125\text{Hz}$, and the system is deemed to be unstable.

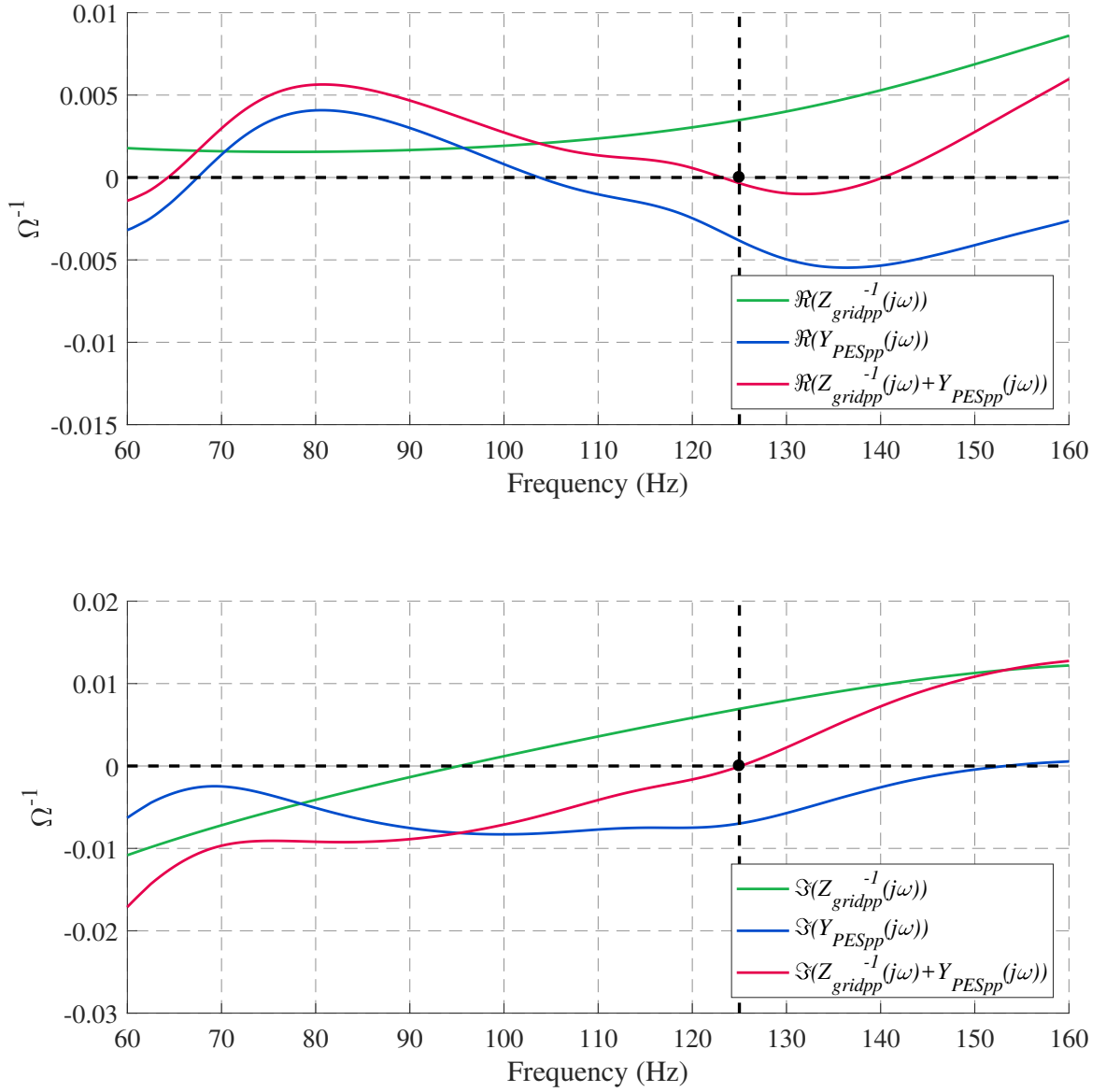


Figure 5.7: The real and imaginary parts of $Z_{gridpp}^{-1}(j\omega) + Y_{PESpp}(j\omega)$.

The real and imaginary parts of $Z_{gridnn}^{-1}(j\omega) + Y_{PESnn}(j\omega)$ for negative sequence are illustrated in Figure 5.8 from which, it is observed that the overall negative sequence admittance is positive.

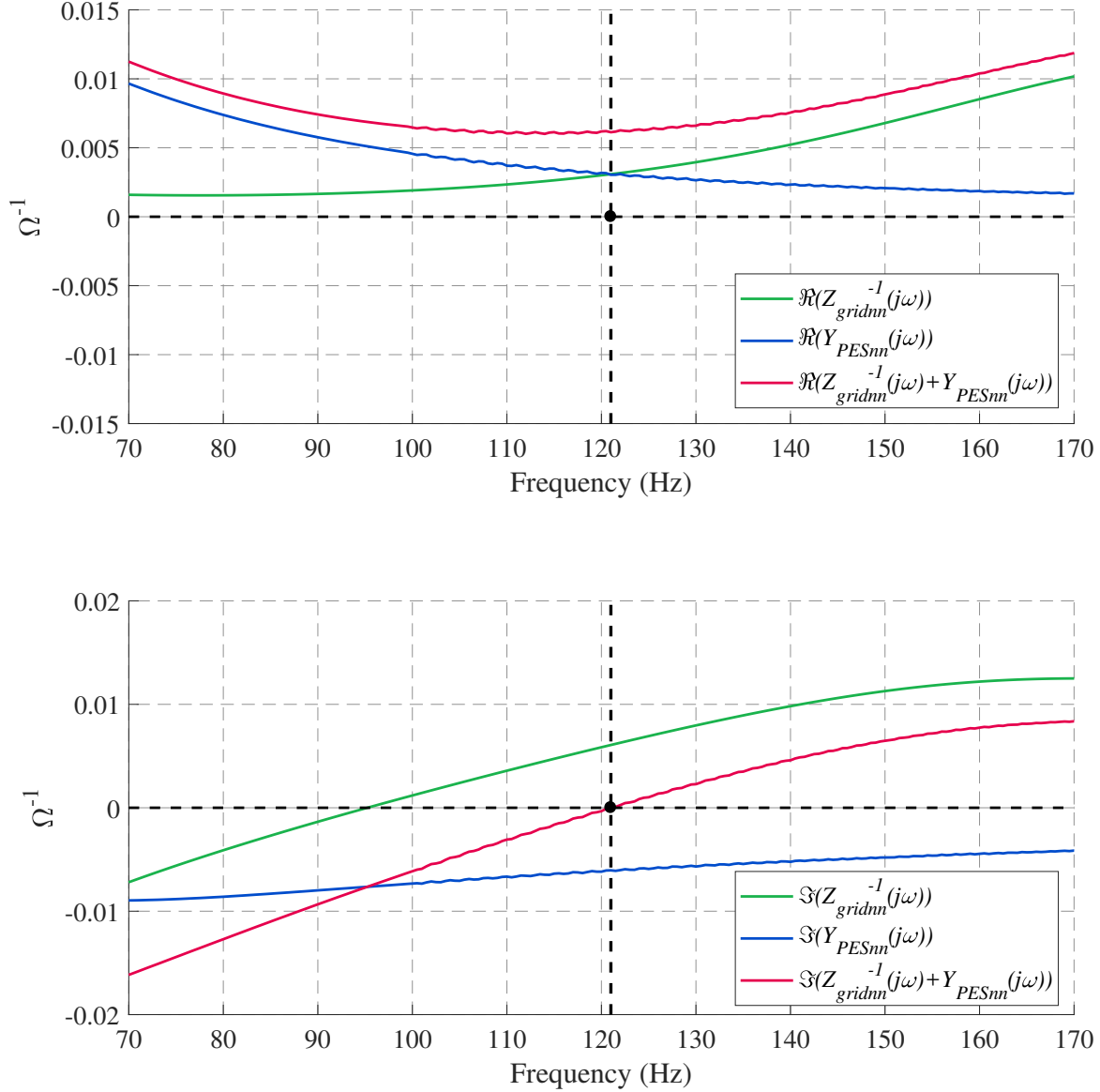


Figure 5.8: The real and imaginary parts of $Z_{gridnn}^{-1}(j\omega) + Y_{PESnn}(j\omega)$.

Since the condition for instability occurs in positive sequence admittance of the overall system, this system is at the risk of instability when the proportional gain (K_p) of the dc-link current controller is changed from $K_p = 1.0 \text{ rad/p.u.}$ to $K_p = 3.0 \text{ rad/p.u.}$ at $t = 3.0 \text{ sec}$, which agrees with the dc-link current response for the unstable case illustrated in Figure 5.9. Note that the oscillation starts to grow and is limited by control non-linearity.

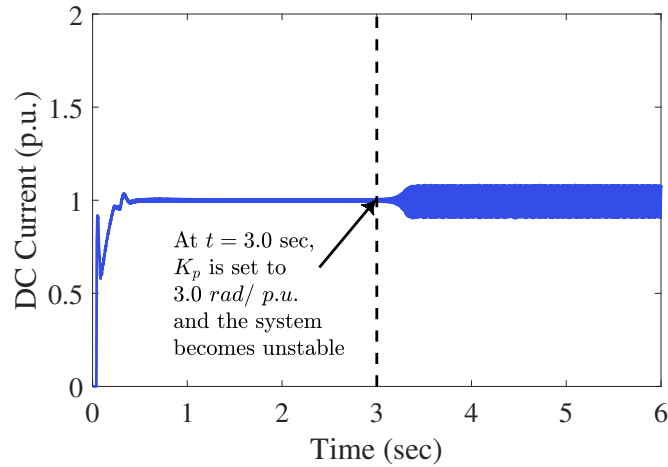


Figure 5.9: The dc-link current response for the unstable case.

5.4 Stability Screening Using the Net Sequence Impedance

Consider the grid-connected PES illustrated in Figure 5.2. The overall closed-loop system can also be represented using Figure 5.10 as discussed in Section 3.2.1 of Chapter 3.

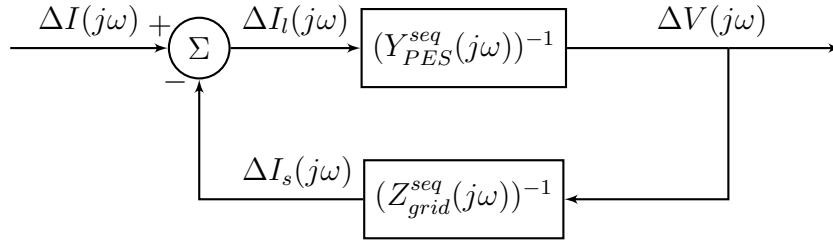


Figure 5.10: The closed-loop representation of the grid-connected PES using the inverse models.

$(Z_{grid}^{seq}(j\omega))^{-1}$ and $(Y_{PES}^{seq}(j\omega))^{-1}$ are the inverse of the sequence impedance of the ac grid and the inverse of the sequence admittance of the PES, respectively. As discussed in Section 5.2, these matrices are obtained using the DQ-based frequency scanning and applying the transformation matrix given in Section 2.9.4 and Equation 2.26 to get the sequence impedance/admittance. Therefore, the stability criterion which was applied to the DQ-based frequency scanning results can be applied to the obtained sequence model as well.

The closed-loop transfer function of the system illustrated in Figure 5.10, is given by:

$$T_2(j\omega) = \left(I + (Y_{PES}^{seq}(j\omega))^{-1} (Z_{grid}^{seq}(j\omega))^{-1} \right)^{-1} (Y_{PES}^{seq}(j\omega))^{-1} \quad (5.7)$$

This transfer function can also be written as:

$$T_2(j\omega) = \left(Z_{grid}^{seq}(j\omega) + (Y_{PES}^{seq}(j\omega))^{-1} \right)^{-1} Z_{grid}^{seq}(j\omega) (Y_{PES}^{seq}(j\omega))^{-1} \quad (5.8)$$

Consider $\Delta(j\omega)$ as:

$$\Delta(j\omega) = \det \left(Z_{grid}^{seq}(j\omega) + (Y_{PES}^{seq}(j\omega))^{-1} \right) \quad (5.9)$$

Considering the approximation illustrated in Figure 5.2, $\Delta(j\omega)$ can be simplified as:

$$\Delta(j\omega) = \left(Z_{grid_{pp}}(j\omega) + Y_{PES_{pp}}^{-1}(j\omega) \right) \left(Z_{grid_{nn}}(j\omega) + Y_{PES_{nn}}^{-1}(j\omega) \right) \quad (5.10)$$

From this equation, it can be observed that the overall system has been divided into two independent positive/negative subsystems and the positive/negative sequences can be separated for stability screening. If the conditions for instability occur in either positive or negative sequences, the system could be at the risk of instability.

If the following conditions are satisfied for a given frequency such as ω_0 , then the deemed to be unstable under certain circumstances:

$$\begin{aligned} \Im \left(Z_{grid_{pp}}(j\omega_0) + Y_{PES_{pp}}^{-1}(j\omega_0) \right) &= 0 \quad \text{and} \\ \Re \left(Z_{grid_{pp}}(j\omega_0) + Y_{PES_{pp}}^{-1}(j\omega_0) \right) &< 0 \end{aligned} \quad (5.11)$$

or,

$$\begin{aligned} \Im \left(Z_{grid_{nn}}(j\omega_0) + Y_{PES_{nn}}^{-1}(j\omega_0) \right) &= 0 \quad \text{and} \\ \Re \left(Z_{grid_{nn}}(j\omega_0) + Y_{PES_{nn}}^{-1}(j\omega_0) \right) &< 0 \end{aligned} \quad (5.12)$$

Note that \Re and \Im denote the real part and the imaginary part, respectively.

To apply the GNC discussed in section 3.4, the open-loop system has to be stable (i.e., $(Z_{grid}^{seq}(j\omega))^{-1}(Y_{PES}^{seq}(j\omega))^{-1}$ has to be stable). However, when using the closed-loop transfer function of the system illustrated in Figure 5.10, the stability of $(Y_{PES}^{seq}(j\omega))^{-1}$ is not guaranteed. As a result, the open-loop system may or may not be stable, and we may get some ambiguity regarding the stability of the system when using the inverse model for the PES.

Since PES is not a passive system, $\Re(Y_{PES_{pp}}^{-1})$ and $\Re(Y_{PES_{nn}}^{-1})$ can become positive or negative at different frequencies. If $\Re(Y_{PES_{pp}}^{-1}(j\omega_0))$ is negative and has a magnitude higher than $\Re(Z_{grid_{pp}}(j\omega_0))$, the $\Re(Z_{grid_{pp}}(j\omega_0) + Y_{PES_{pp}}^{-1}(j\omega_0))$ can become negative and the system could become unstable.

To prevent such instabilities, the controllers could be designed so that the values of $\Re(Y_{PES_{pp}}^{-1})$ and $\Re(Y_{PES_{nn}}^{-1})$ are positive at all frequencies. As a result, both real parts of $Z_{grid_{pp}}(j\omega) + Y_{PES_{pp}}^{-1}(j\omega)$ and $Z_{grid_{nn}}(j\omega) + Y_{PES_{nn}}^{-1}(j\omega)$ are positive at all frequencies, which makes the system is less susceptible to instabilities. Next, two case studies are presented to analyze the stability of a grid-connected PES via approximate stability screening using the net sequence impedance.

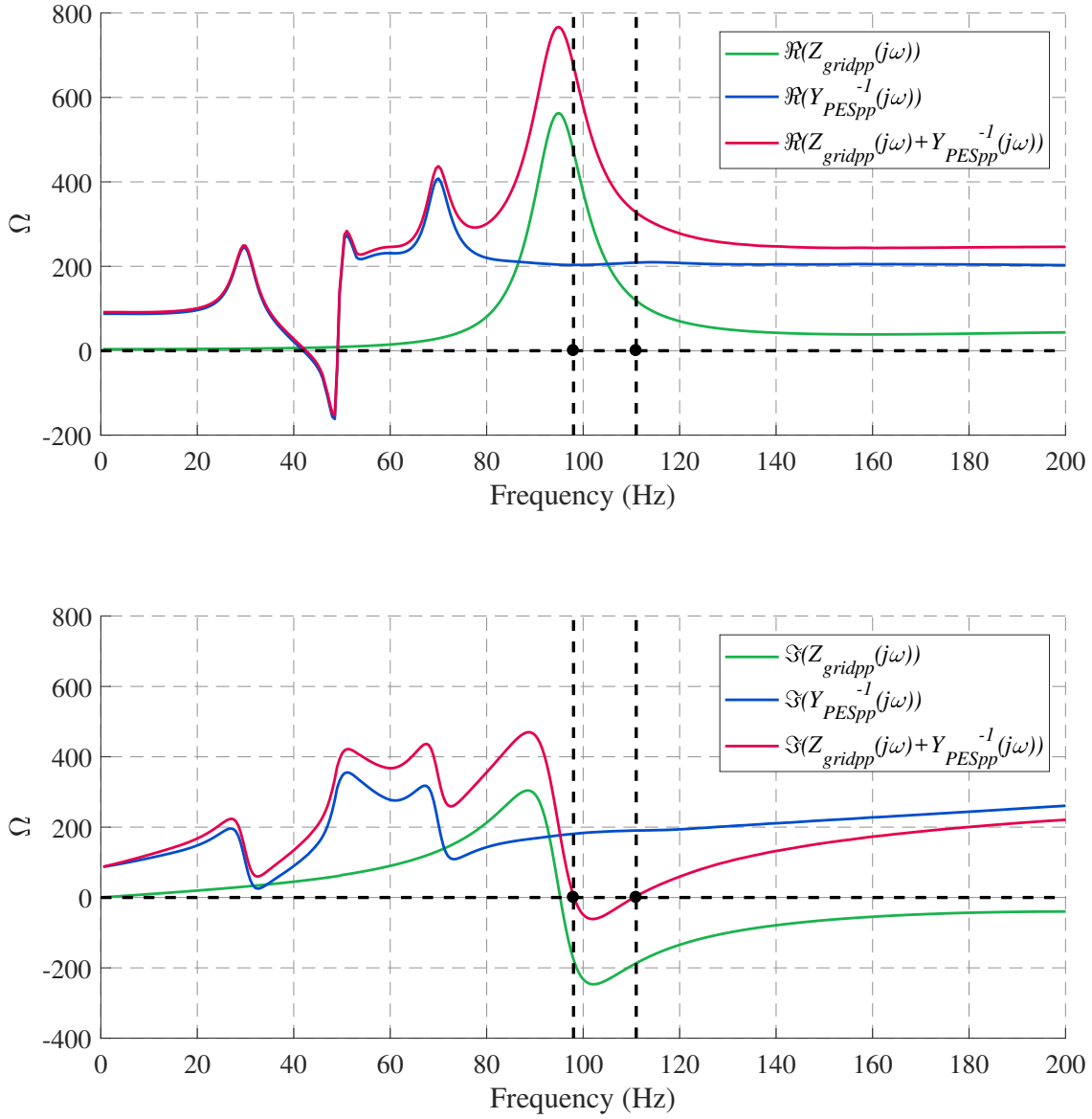
5.5 Case Study: CIGRE-HVDC Benchmark Model

Stability Screening Using the Net Sequence Impedance

The CIGRE-HVDC benchmark model illustrated in Figure 5.3, is used for approximate stability screening using the net sequence impedance.

5.5.1 Case 1: Stable Case ($K_p = 1.0 \text{ rad/p.u.}$)

The real and imaginary parts of $Z_{grid_{pp}}(j\omega) + Y_{PES_{pp}}^{-1}(j\omega)$ for positive sequence are illustrated in Figure 5.11. It is observed that $\Im(Z_{grid_{pp}}(j\omega) + Y_{PES_{pp}}^{-1}(j\omega)) = 0$ at frequencies $f = 98Hz$ and $f = 111Hz$. At both frequencies, the real part of $Y_{PES_{pp}}^{-1}(j\omega)$ is positive. The overall sequence impedance is thus positive at $f = 98Hz$ and $f = 111Hz$. Next, the same procedure should be applied for the negative sequence to check whether the conditions for instability occur.

Figure 5.11: The real and imaginary parts of $Z_{gridpp}(j\omega) + Y_{PESpp}^{-1}(j\omega)$.

The real and imaginary parts of $Z_{gridnn}(j\omega) + Y_{PESnn}^{-1}(j\omega)$ for negative sequence are illustrated in Figure 5.12. Since $Y_{PESnn}^{-1}(j\omega)$ is positive at both frequencies $f = 97Hz$ and $f = 122Hz$, the overall negative sequence impedance positive at these frequencies.

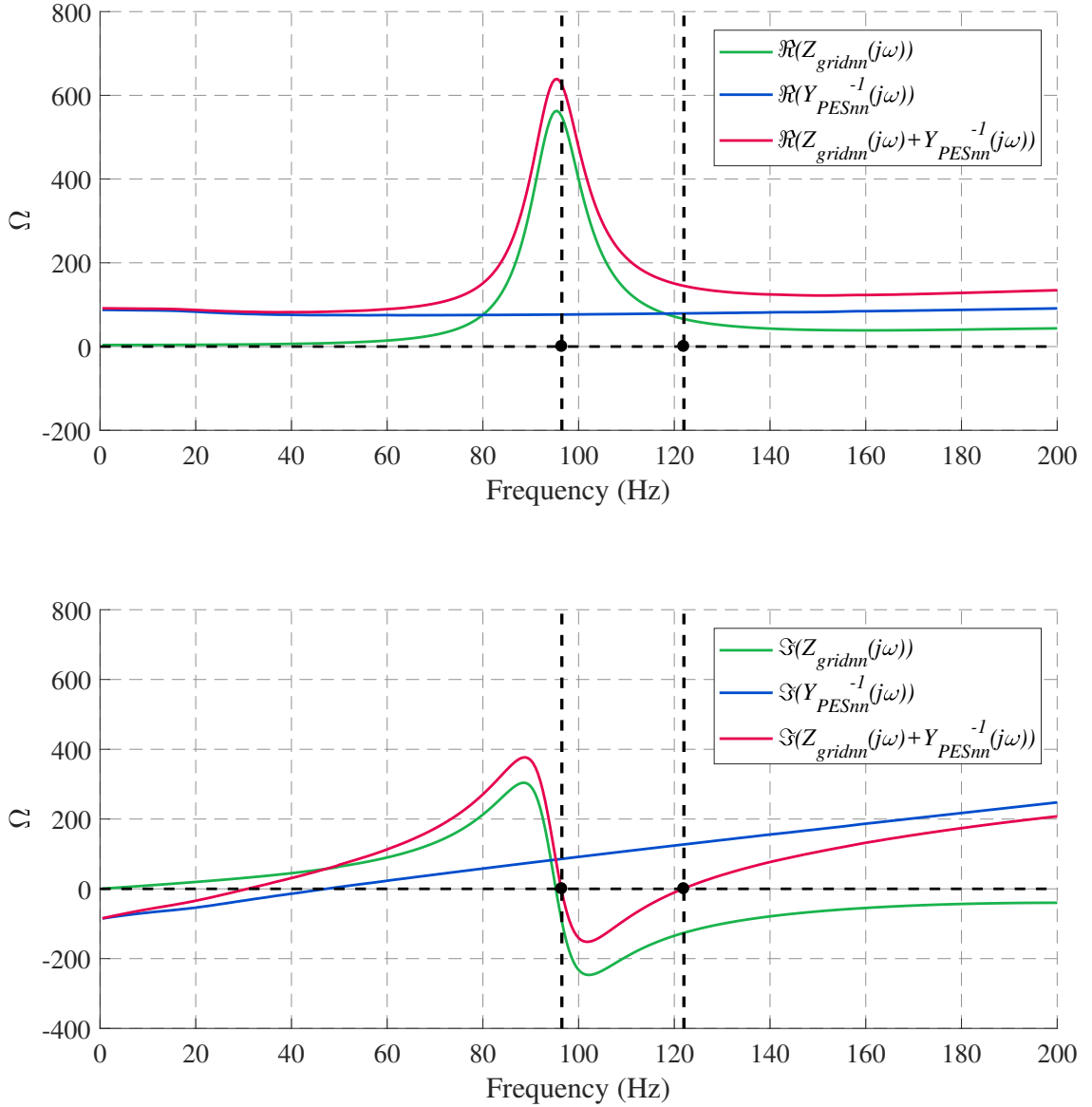


Figure 5.12: The real and imaginary parts of $Z_{gridnn}(j\omega) + Y_{PESnn}^{-1}(j\omega)$.

Since neither of the conditions for instability occurs in positive or negative sequences, this system is likely stable, which agrees with the dc-link current response of the stable case illustrated in Figure 5.6.

5.5.2 Case 2: Unstable Case ($K_p = 3.0 \text{ rad/p.u.}$)

The proportional gain (K_p) of the dc-link current controller is changed from $K_p = 1.0 \text{ rad/p.u.}$ to $K_p = 3.0 \text{ rad/p.u.}$ at $t = 3.0 \text{ sec.}$

The real and imaginary parts of $Z_{grid_{pp}}(j\omega) + Y_{PES_{pp}}^{-1}(j\omega)$ for positive sequence are illustrated in Figure 5.13. From this figure, it is observed that $\Im(Z_{grid_{pp}}(j\omega) + Y_{PES_{pp}}^{-1}(j\omega)) = 0$ at no frequencies. Consequently, the overall positive sequence admittance is positive and the system is likely stable.

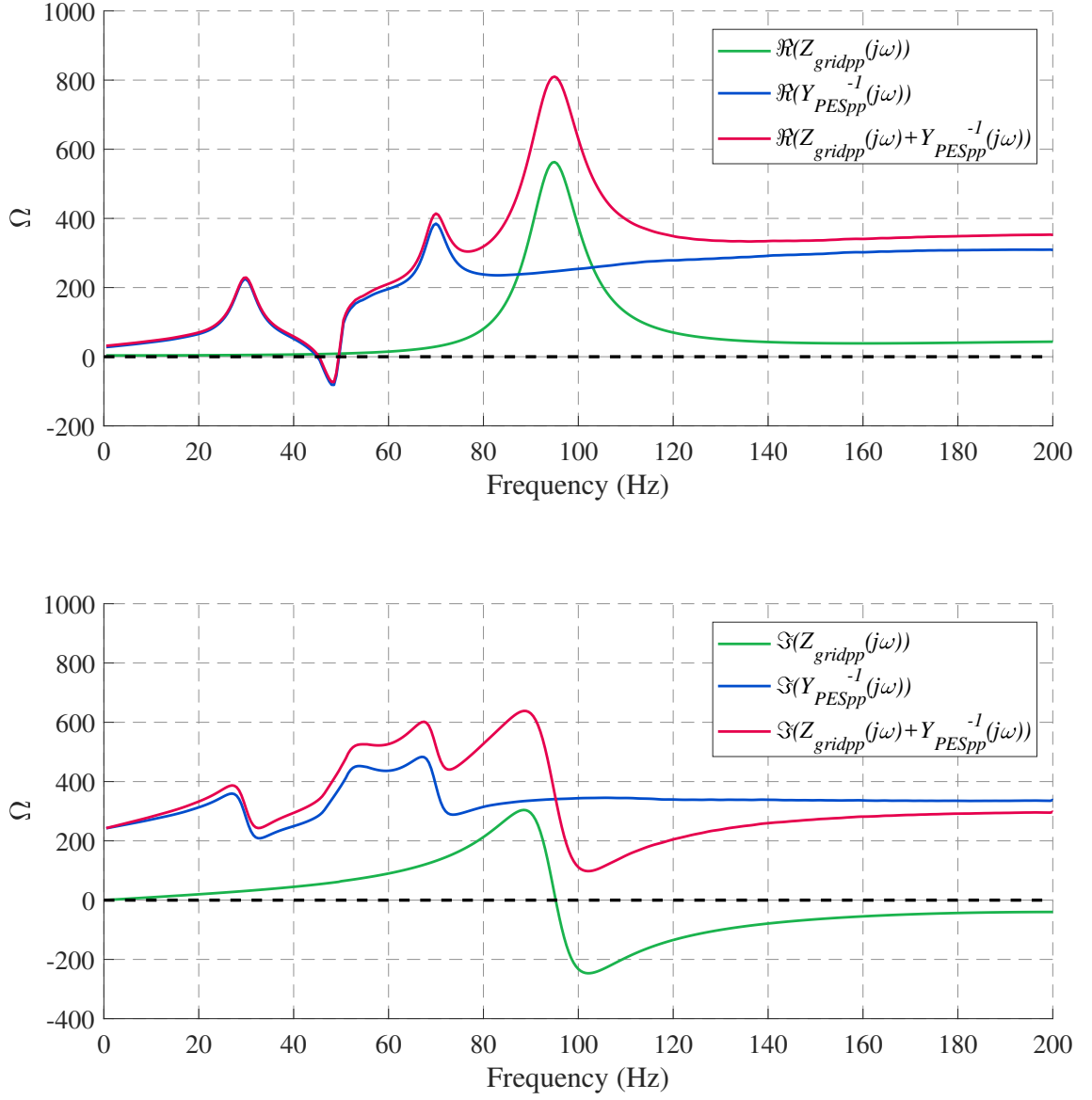


Figure 5.13: The real and imaginary parts of $Z_{gridpp}(j\omega) + Y_{PESpp}^{-1}(j\omega)$.

The real and imaginary parts of $Z_{gridnn}(j\omega) + Y_{PESnn}^{-1}(j\omega)$ for negative sequence are illustrated in Figure 5.14. It is seen that the overall negative sequence impedance is negative at $f = 58Hz$ and the system is at the risk of instability.

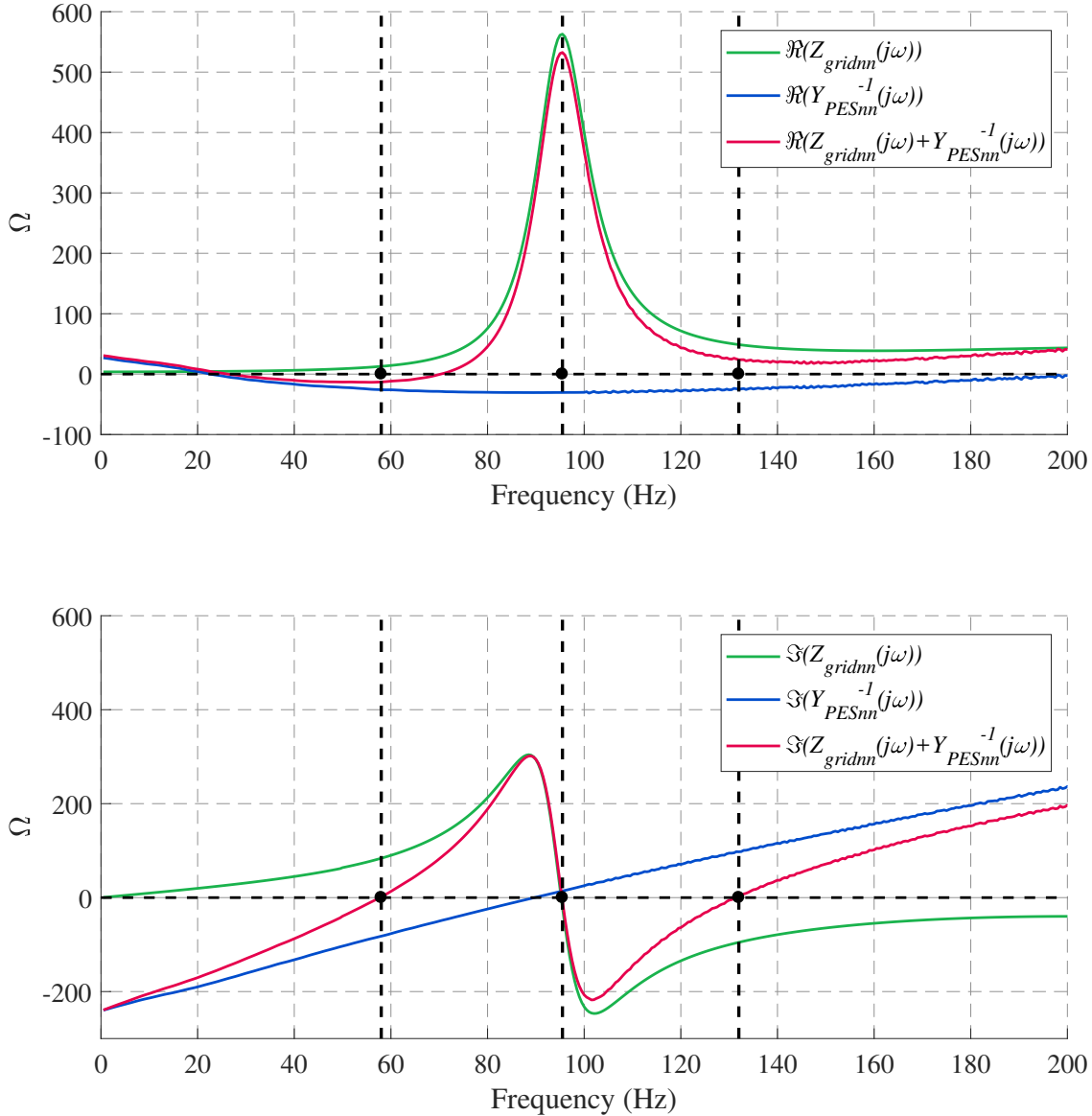


Figure 5.14: The real and imaginary parts of $Z_{gridnn}(j\omega) + Y_{PESnn}^{-1}(j\omega)$.

Since the condition for instability occurs in negative sequence impedance of the overall system, this system is at the risk of instability when the proportional gain (K_p) of the dc-link current controller is changed from $K_p = 1.0 \text{ rad/p.u.}$ to $K_p = 3.0 \text{ rad/p.u.}$ at $t = 3.0 \text{ sec.}$ This agrees with the dc-link current response for the unstable case illustrated in Figure 5.9.

5.6 Case Study: STATCOM Stability Screening

Using the Net Sequence Impedance

A $\pm 200 \text{ MVar}$ STATCOM operating with a Type-I controller [27], is illustrated in Figure 5.15. This STATCOM is connected to an ac network with the operating frequency of 50 Hz .

The real and imaginary parts of $Z_{gridpp}(j\omega) + Y_{PESpp}^{-1}(j\omega)$ for positive sequence are illustrated in Figure 5.16. It is observed that the overall positive sequence admittance is positive at $f = 59Hz$ and $f = 249Hz$ and the system is likely stable.

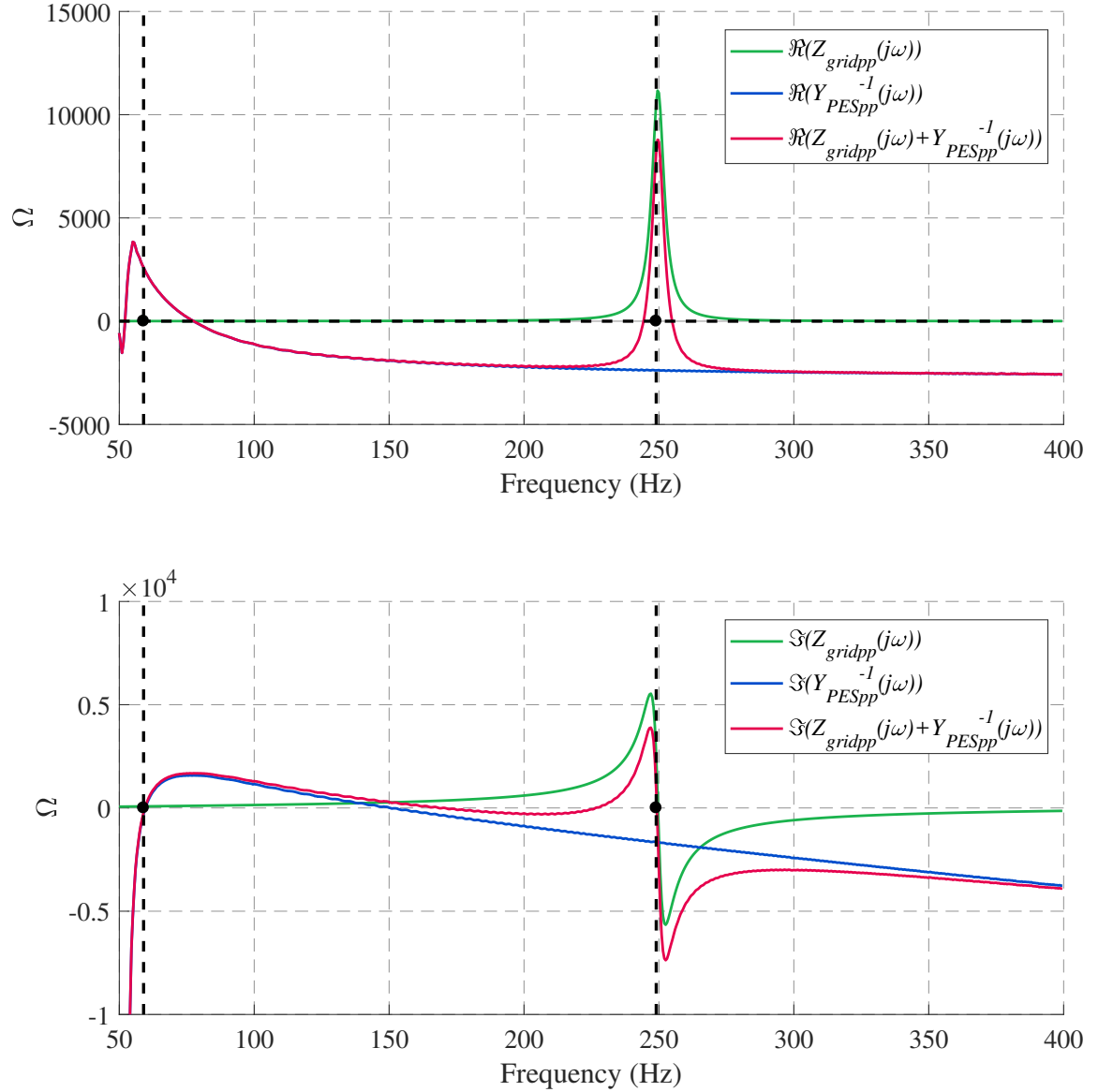


Figure 5.16: The real and imaginary parts of $Z_{gridpp}(j\omega) + Y_{PESpp}^{-1}(j\omega)$.

The real and imaginary parts of $Z_{grid_{nn}}(j\omega) + Y_{PES_{nn}}^{-1}(j\omega)$ for negative sequence are illustrated in Figure 5.17. It is seen that the overall negative sequence impedance is negative at $f = 141Hz$ and the system is deemed to be unstable.

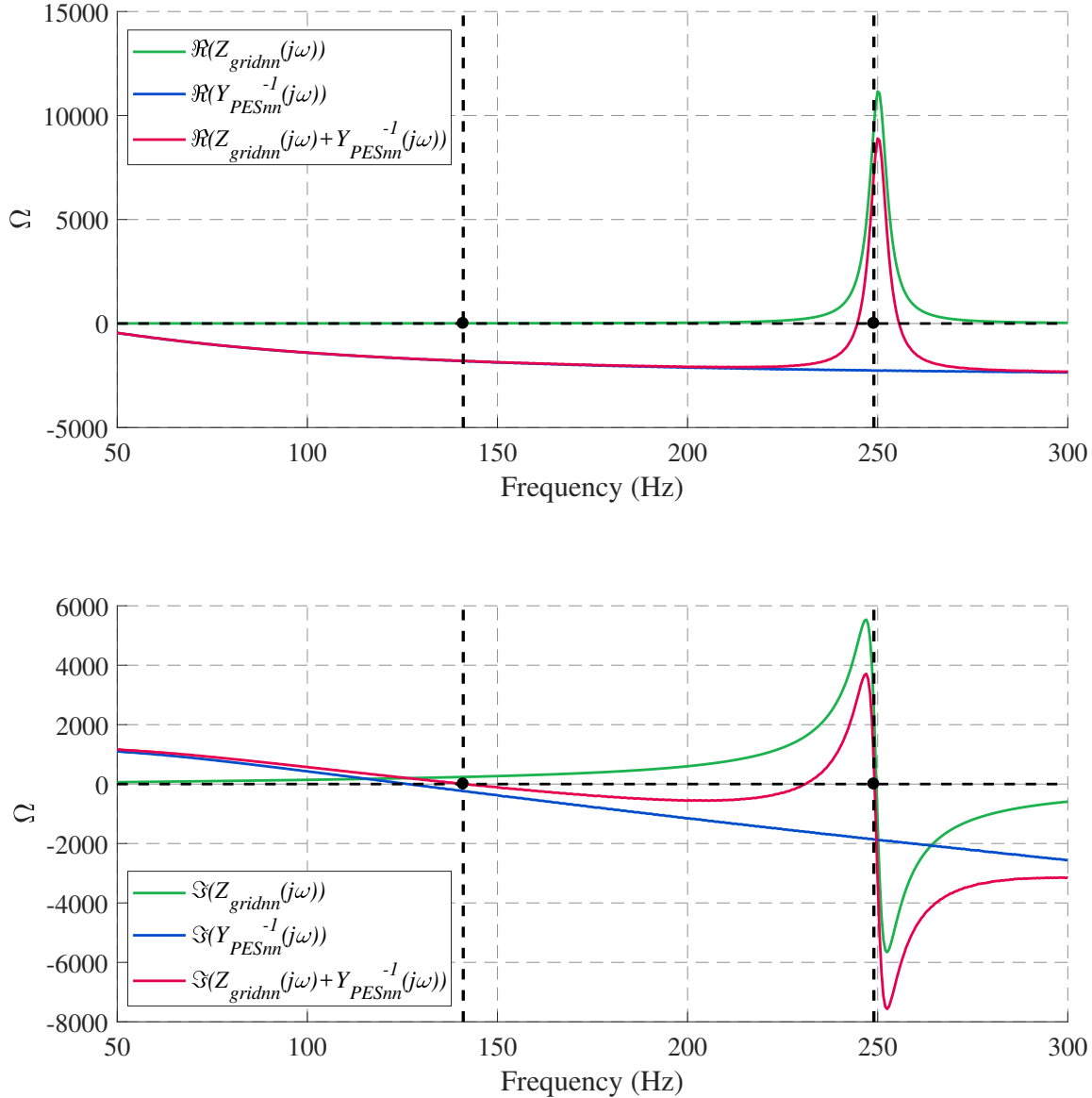


Figure 5.17: The real and imaginary parts of $Z_{grid_{nn}}(j\omega) + Y_{PES_{nn}}^{-1}(j\omega)$.

Since the condition for instability occurs in negative sequence impedance of the overall system, this system is deemed to be unstable when the proportional gain (K_p) of the dc-link voltage controller is set to $K_p = 0.5 \text{ rad/p.u.}$. This conclusion does not agree with the simulation as seen by the simulation of line current in Figure 5.18, which is stable.

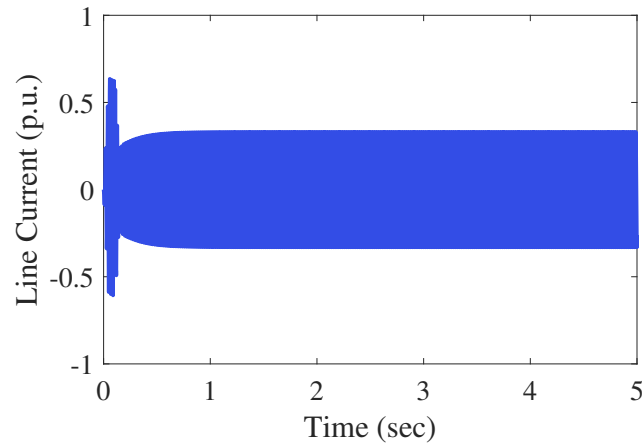


Figure 5.18: The response of the line current of STATCOM for the stable case.

When using the net sequence impedance of the overall system for stability screening, the inverse of the sequence admittance of the PES is used. Note that $Y_{PES}(j\omega)$ is a non-passive system and it may have RHP zeros. Consequently, $Y_{PES}^{-1}(j\omega)$ may be an unstable system. Note that, if $Y_{PES}^{-1}(j\omega)$ is unstable, it may lead to inaccurate stability screening conclusions.

5.7 Discussion

The positive/negative sequence-based approach is widely used in industry as a screening tool [70], as shown in the examples in Section 5.3 and Section 5.5. But it has the disadvantage that even though it gives generally correct indications of stability, it can give erroneous results due to the small but existent cross-coupling of frequencies. Instead, the stability analysis using GNC or eigenlocus stability analysis based on the DQ-based frequency scanning results is recommended. Bellow, a comparison between the approximate sequence based stability screening technique discussed in this chapter and the Nyquist stability criterion presented in Chapter 3 is summarized:

1. In DQ-based stability analysis, the Nyquist stability criterion requires calculating $\det(D(j\omega))$. Alternatively, the eigenlocus stability approach requires calculating the eigenvalues of $D(j\omega)$. Since a determinant or an eigenvalue calculation is required and the main concentration is on the number of encirclement, measuring the direct effects of a change in the PES (i.e., changing $Y_{PES_{pp}}(j\omega)$), on the stability of the combined system is not straightforward. In contrast, using the sequence-based approximate stability screening technique gives the advantage of calculating $\det(D(j\omega))$ in terms of positive and negative sequences and monitoring the positive and negative sequences separately (i.e., no determinant is involved). As a result, the stability information obtained from the sequence-based approximate stability screening technique is quite intuitive since the resistance/conductance of the PES is monitored at the point of resonance.

2. It should be considered that $Y_{PES}^{seq}(j\omega)$ is assumed to be a diagonal matrix, which is not true for non-passive systems, as illustrated in Section 2.7. Consequently, the stability screening technique discussed in this chapter is an approximate method. Whereas, the GNC gives exact information about the instability and the number of unstable poles in a system. Nevertheless, the approximate stability screening can predict the instabilities in a system, as illustrated in the case studies of this chapter.
3. When using the approximate stability screening, the DQ-based frequency scanning results are obtained and used. Screening the stability using the net sequence impedance, requires the calculation of the inverse of the sequence admittance of the PES. Even if the sequence admittance has all left hand side poles, its inverse may not, if it is not passive as in the with PES. If the inverse of the sequence admittance of the PES has right hand side poles, it may result in incorrect stability screening results. In such circumstances, further detailed simulation is required to determine the stability of the system.

5.8 Conclusion

In this chapter, an approximate stability screening technique was presented. This approximate stability screening method uses the results from the frequency scanning of the ac network and the PES. This technique can be used instead of GNC if the direct effects of changing the impedance/admittance of the PES on the stability of the interactions is to be studied. Two stable and unstable case studies were presented to verify the results from this approximate stability screening method. From the simulation cases, it can be concluded that this method can predict the stability of the interactions. However, in some cases, it may result in incorrect stability screening results. As a result, this thesis discourages using this technique for stability screening purposes.

Chapter 6

Conclusion

6.1 Concluding Remarks and Discussion

Frequency scanning is a numerical method for extracting the small-signal model of the power electronic systems (PESs) via injecting a small-amplitude wide-band signal in the time-domain simulation of the PES. This thesis conducted a comprehensive survey of frequency scanning based stability analysis methods. It then implemented these on several examples to show the benefit or drawback of each. It then applied it to two examples, one of the CIGRE-HVDC benchmark and the other of a STATCOM, to show how the stability can be determined for such systems.

This thesis is focused on the stability analysis of the interactions between a PES and its ac grid using frequency scanning techniques. The frequency scanning response of a system can be obtained using different variables. It was illustrated that the frequency scanning results using phase/sequence and $\alpha\beta$ variables are distorted due to frequency coupling and cannot be used for stability analysis. For balanced three-

phase PESs with negligible low order harmonics, DQ-based frequency scanning can be used instead to obtain accurate frequency scanning results.

The stability of the interactions of a PES with its grid can be predicted using the obtained models of PESs and the ac grids. The Generalized Nyquist Criterion (GNC) and eigenlocus stability approach were used to determine the stability. Using the eigenlocus stability approach gives the advantage of determining the unstable modes and unstable eigenvalue, calculating the gain margin and finding the frequency of oscillations at instability. Whereas the GNC only provides information on whether the system is stable or not.

The gain margin of a system was calculated using the eigenlocus stability approach and it was illustrated that using this technique, the ac grid critical system strength (i.e., SCR) on the boundary of stability can be determined.

An approximate stability screening technique based on the positive and negative sequence impedance/admittance seen at the terminals of the PES was presented. This approach is widely used in industry, but in the thesis, it was shown that it has the disadvantage that even though it gives generally correct indications of stability, it can give erroneous results due to the small but existent cross-coupling of frequencies. As a result, this thesis discourages using the approximate stability screening technique based on the positive and negative sequence impedance/admittance. The DQ-based frequency scanning can be used instead to access the stability by applying GNC or eigenlocus stability approach.

6.2 Suggestions for Future Work

1. The stability screening methods presented in this thesis were used to verify the stability of an HVDC system and a STATCOM system. However, these techniques can be used for stability analysis of other converter systems such as MMC systems.
2. The stability screening techniques can be used to study the converter-network interactions in different systems such as grid forming inverters.
3. The time-domain simulations and analytical calculations such as the state-space based eigenvalue analysis are used for grid-connected PESs. Each of these methods have some limitations. The time-domain simulations are time-consuming, case-specific, and can be performed for small size systems due to limited computational power. The state-space based eigenvalue analysis provides detailed information about the system and can be used for larger size systems. However, this method requires complete detailed information about the system, which makes it difficult to use when black-box controllers/models are present in the system. In such scenarios, the frequency scanning technique can be used to extract the frequency response of the black-box controllers/models. Vector fitting techniques can be applied to the frequency response obtained from frequency scanning for getting the state-space equations of the black-box controllers/models. The state-space equations for the black-box controllers/models can then be combined with the state-space equations of other known elements of the system to get the state-space equations of the overall system. When the

state-space equations of the overall system are extracted, the state-space based eigenvalue analysis can be performed to access the detailed information of the overall system.

4. The sequence-based approximate stability screening technique can assist in reducing the risk of instabilities in a system when designing controllers. Setting the controller gain properly so that the real parts of $Y_{PESpp}(j\omega)$ and $Y_{PESnn}(j\omega)$ are positive can help prevent instabilities resulting from a negative resistance/conductance. An objective function can be defined using the positive/negative sequence resistance/conductance, and the frequency scanning techniques can be performed to assess the objective function. A proper controller gain can then be determined by optimizing the formulated objective function using automated design tools.

Appendix A

Relationship between positive and negative frequency components

Since any real signal has equal parts of positive and negative frequencies,

$$x(t) \longleftrightarrow X(j\omega) \implies |X(-j\omega)| = |X(j\omega)| \quad (\text{A.1})$$

In other words, for any real signal, the absolute value of positive and negative frequencies are equal. However, a phase shift between the positive and negative frequencies exists.

For example, $\sin(\omega_0 t) = \frac{e^{j\omega_0 t} - e^{-j\omega_0 t}}{2j}$ and $\cos(\omega_0 t) = \frac{e^{j\omega_0 t} + e^{-j\omega_0 t}}{2}$. It is observed that the positive and negative frequencies have the same absolute value and opposite phase angle. This means that a negative frequency component at frequency f_0 is equal to the positive frequency component at frequency f_0 and, vice versa.

Appendix B

Relationship between the sequence and DQ variables

To obtain the relationship between the sequence and DQ variables, the following transformations can be considered:



Figure B.1: Transformation between different domains

The relationship between DQ variables and $\alpha\beta$ variables is illustrated in Equation B.2. Note that the power invariant property has been used for the equations.

$$\begin{aligned}
\begin{bmatrix} x_d(t) \\ x_q(t) \\ x_0(t) \end{bmatrix} &= \sqrt{\frac{2}{3}} \begin{bmatrix} \cos(\omega_0 t) & \cos(\omega_0 t - \frac{2\pi}{3}) & \cos(\omega_0 t + \frac{2\pi}{3}) \\ \sin(\omega_0 t) & \sin(\omega_0 t - \frac{2\pi}{3}) & \sin(\omega_0 t + \frac{2\pi}{3}) \\ \frac{1}{\sqrt{2}} & \frac{1}{\sqrt{2}} & \frac{1}{\sqrt{2}} \end{bmatrix} \begin{bmatrix} x_a(t) \\ x_b(t) \\ x_c(t) \end{bmatrix} \\
\begin{bmatrix} x_a(t) \\ x_b(t) \\ x_c(t) \end{bmatrix} &= \sqrt{\frac{2}{3}} \begin{bmatrix} 1 & 0 & \frac{1}{\sqrt{2}} \\ -\frac{1}{2} & \frac{\sqrt{3}}{2} & \frac{1}{\sqrt{2}} \\ -\frac{1}{2} & -\frac{\sqrt{3}}{2} & \frac{1}{\sqrt{2}} \end{bmatrix} \begin{bmatrix} x_\alpha(t) \\ x_\beta(t) \\ x_0(t) \end{bmatrix}
\end{aligned} \tag{B.1}$$

Therefore,

$$\begin{bmatrix} x_d(t) \\ x_q(t) \\ x_0(t) \end{bmatrix} = \begin{bmatrix} \cos(\omega_0 t) & \sin(\omega_0 t) & 0 \\ \sin(\omega_0 t) & -\cos(\omega_0 t) & 0 \\ 0 & 0 & 1 \end{bmatrix} \begin{bmatrix} x_\alpha(t) \\ x_\beta(t) \\ x_0(t) \end{bmatrix} \tag{B.2}$$

Therefore:

$$\begin{aligned}
x_d(t) &= \cos(\omega_0 t)x_\alpha(t) - \sin(\omega_0 t)x_\beta(t) \\
x_q(t) &= \sin(\omega_0 t)x_\alpha(t) - \cos(\omega_0 t)x_\beta(t)
\end{aligned} \tag{B.3}$$

Since $\cos(\omega_0 t) \pm j \sin(\omega_0 t) = e^{\pm j\omega_0 t}$, the following equations can be obtained:

$$\begin{aligned}
x_d(t) + jx_q(t) &= e^{j\omega_0 t} (x_\alpha(t) - jx_\beta(t)) \\
x_d(t) - jx_q(t) &= e^{-j\omega_0 t} (x_\alpha(t) + jx_\beta(t))
\end{aligned} \tag{B.4}$$

This equation has been obtained in [36]. The relationship between $\alpha\beta$ variables and

the sequence variable can be obtained using the following procedure:

$$\begin{aligned}
 \begin{bmatrix} x_\alpha(j\omega) \\ x_\beta(j\omega) \\ x_0(j\omega) \end{bmatrix} &= \sqrt{\frac{2}{3}} \begin{bmatrix} 1 & -\frac{1}{2} & -\frac{1}{2} \\ 0 & \frac{\sqrt{3}}{2} & -\frac{\sqrt{3}}{2} \\ \frac{1}{\sqrt{2}} & \frac{1}{\sqrt{2}} & \frac{1}{\sqrt{2}} \end{bmatrix} \begin{bmatrix} x_a(j\omega) \\ x_b(j\omega) \\ x_c(j\omega) \end{bmatrix} \\
 \begin{bmatrix} x_a(j\omega) \\ x_b(j\omega) \\ x_c(j\omega) \end{bmatrix} &= \sqrt{\frac{1}{3}} \begin{bmatrix} 1 & 1 & 1 \\ e^{\frac{4\pi}{3}j} & e^{\frac{2\pi}{3}j} & 1 \\ e^{\frac{2\pi}{3}j} & e^{\frac{4\pi}{3}j} & 1 \end{bmatrix} \begin{bmatrix} x_p(j\omega) \\ x_n(j\omega) \\ x_0(j\omega) \end{bmatrix}
 \end{aligned} \tag{B.5}$$

Therefore:

$$\begin{aligned}
 \begin{bmatrix} x_\alpha(j\omega) \\ x_\beta(j\omega) \\ x_0(j\omega) \end{bmatrix} &= \sqrt{\frac{1}{2}} \begin{bmatrix} 1 & 1 & 0 \\ -j & j & 0 \\ 0 & 0 & \sqrt{2} \end{bmatrix} \begin{bmatrix} x_p(j\omega) \\ x_n(j\omega) \\ x_0(j\omega) \end{bmatrix} \\
 \begin{bmatrix} x_p(j\omega) \\ x_n(j\omega) \\ x_0(j\omega) \end{bmatrix} &= \sqrt{\frac{1}{2}} \begin{bmatrix} 1 & j & 0 \\ 1 & -j & 0 \\ 0 & 0 & \sqrt{2} \end{bmatrix} \begin{bmatrix} x_\alpha(j\omega) \\ x_\beta(j\omega) \\ x_0(j\omega) \end{bmatrix}
 \end{aligned} \tag{B.6}$$

By using the above equation and neglecting the zero sequence:

$$\begin{aligned}
 x_p(j\omega) &= \sqrt{\frac{1}{2}} (x_\alpha(j\omega) + jx_\beta(j\omega)) \\
 x_n(j\omega) &= \sqrt{\frac{1}{2}} (x_\alpha(j\omega) - jx_\beta(j\omega))
 \end{aligned} \tag{B.7}$$

By combining Equation B.4 and Equation B.7,

$$\begin{aligned} x_p(t) &= \sqrt{\frac{1}{2}} e^{j\omega_0 t} (x_d(t) - jx_q(t)) \\ x_n(t) &= \sqrt{\frac{1}{2}} e^{-j\omega_0 t} (x_d(t) + jx_q(t)) \end{aligned} \quad (\text{B.8})$$

Since $x(t) \longleftrightarrow X(j\omega)$, $\implies e^{j\omega_0 t} x(t) \longleftrightarrow X(j\omega - j\omega_0)$, the following transformation matrices can be derived:

$$\begin{aligned} \begin{bmatrix} x_p(j\omega + j\omega_0) \\ x_n(j\omega - j\omega_0) \end{bmatrix} &= \sqrt{\frac{1}{2}} \begin{bmatrix} 1 & -j \\ 1 & j \end{bmatrix} \begin{bmatrix} x_d(j\omega) \\ x_q(j\omega) \end{bmatrix} \\ \begin{bmatrix} x_d(j\omega) \\ x_q(j\omega) \end{bmatrix} &= \sqrt{\frac{1}{2}} \begin{bmatrix} 1 & 1 \\ j & -j \end{bmatrix} \begin{bmatrix} x_p(j\omega + j\omega_0) \\ x_n(j\omega - j\omega_0) \end{bmatrix} \end{aligned} \quad (\text{B.9})$$

Appendix C

Phase to sequence admittance transformation matrix

To obtain phase to sequence admittance transformation matrix, consider the following equation:

$$\begin{aligned} I_{abc}(j\omega) &= Y_{abc}(j\omega)V_{abc}(j\omega) \\ I_{pn0}(j\omega) &= Y_{pn0}(j\omega)V_{pn0}(j\omega) \end{aligned} \tag{C.1}$$

Also, from 2.9 and constant power situation,

$$\begin{aligned} \begin{bmatrix} I_a(j\omega) \\ I_b(j\omega) \\ I_c(j\omega) \end{bmatrix} &= \sqrt{\frac{1}{3}} \begin{bmatrix} 1 & 1 & 1 \\ \alpha^2 & \alpha & 1 \\ \alpha & \alpha^2 & 1 \end{bmatrix} \begin{bmatrix} I_p(j\omega) \\ I_n(j\omega) \\ I_0(j\omega) \end{bmatrix} \\ \begin{bmatrix} V_a(j\omega) \\ V_b(j\omega) \\ V_c(j\omega) \end{bmatrix} &= \sqrt{\frac{1}{3}} \begin{bmatrix} 1 & 1 & 1 \\ \alpha^2 & \alpha & 1 \\ \alpha & \alpha^2 & 1 \end{bmatrix} \begin{bmatrix} V_p(j\omega) \\ V_n(j\omega) \\ V_0(j\omega) \end{bmatrix} \end{aligned} \tag{C.2}$$

By combining the two equations above:

$$\begin{bmatrix} I_p(j\omega) \\ I_n(j\omega) \\ I_0(j\omega) \end{bmatrix} = \begin{bmatrix} 1 & 1 & 1 \\ \alpha^2 & \alpha & 1 \\ \alpha & \alpha^2 & 1 \end{bmatrix}^{-1} Y_{abc}(j\omega) \begin{bmatrix} 1 & 1 & 1 \\ \alpha^2 & \alpha & 1 \\ \alpha & \alpha^2 & 1 \end{bmatrix} \begin{bmatrix} V_p(j\omega) \\ V_n(j\omega) \\ V_0(j\omega) \end{bmatrix} \quad (\text{C.3})$$

Therefore,

$$\begin{aligned} Y_{pn0}(j\omega) &= \begin{bmatrix} 1 & 1 & 1 \\ \alpha^2 & \alpha & 1 \\ \alpha & \alpha^2 & 1 \end{bmatrix}^{-1} Y_{abc}(j\omega) \begin{bmatrix} 1 & 1 & 1 \\ \alpha^2 & \alpha & 1 \\ \alpha & \alpha^2 & 1 \end{bmatrix} \\ Y_{abc}(j\omega) &= \begin{bmatrix} 1 & 1 & 1 \\ \alpha^2 & \alpha & 1 \\ \alpha & \alpha^2 & 1 \end{bmatrix} Y_{pn0}(j\omega) \begin{bmatrix} 1 & 1 & 1 \\ \alpha^2 & \alpha & 1 \\ \alpha & \alpha^2 & 1 \end{bmatrix}^{-1} \end{aligned} \quad (\text{C.4})$$

Bibliography

- [1] M. Yang, “Application of Power Electronics in Power System,” in *2016 7th International Conference on Education, Management, Computer and Medicine (EMCM 2016)*, Atlantis Press, 2017.
- [2] B. K. Bose, “Power Electronics, Smart Grid, and Renewable Energy Systems,” *Proceedings of the IEEE*, vol. 105, no. 11, pp. 2011–2018, 2017.
- [3] R. Teodorescu, M. Liserre, and P. Rodriguez, *Grid Converters for Photovoltaic and Wind Power Systems*. Wiley-IEEE Press, Jul. 2011.
- [4] P. Brogan, “The Stability of Multiple, High power, Active Front End Voltage Sourced Converters When Connected to Wind Farm Collector System,” in *Proc. Euro. Conf. Power Electron. and Appl.*, 2010, pp. 1–6.
- [5] J. H. R. Enslin and P. J. M. Heskes, “Harmonic Interaction Between a Large Number of Distributed Power Inverters and the Distribution Network,” *IEEE Transactions on Power Electronics*, vol. 19, no. 6, pp. 1586–1593, Nov. 2004.
- [6] J. Rocabert, A. Luna, F. Blaabjerg, and P. Rodríguez, “Control of Power Converters in AC Microgrids,” *IEEE Transactions on Power Electronics*, vol. 27, no. 11, pp. 4734–4749, Nov. 2012.

- [7] E. Mollerstedt and B. Bernhardsson, "Out of control because of harmonics-an analysis of the harmonic response of an inverter locomotive," *IEEE Control Systems Magazine*, vol. 20, no. 4, pp. 70–81, Aug. 2000.
- [8] S. Lissandron, L. Dalla Santa, P. Mattavelli, and B. Wen, "Experimental Validation for Impedance-Based Small-Signal Stability Analysis of Single-Phase Interconnected Power Systems With Grid-Feeding Inverters," *IEEE Journal of Emerging and Selected Topics in Power Electronics*, vol. 4, no. 1, pp. 103–115, Mar. 2016.
- [9] B. R. Andersen, "HVDC transmission-opportunities and challenges," in *The 8th IEE International Conference on AC and DC Power Transmission*, Mar. 2006, pp. 24–29.
- [10] J. A. C. Forrest and B. Allard, "Thermal problems caused by harmonic frequency leakage fluxes in three-phase, three-winding converter transformers," *IEEE Transactions on Power Delivery*, vol. 19, no. 1, pp. 208–213, Jan. 2004.
- [11] M. Heathcote and D. Franklin, *The J & P Transformer Book, twelfth edition*. Reed Educational and Professional Publishing Ltd, 1998.
- [12] L. Luo, Y. Li, Kazuo Nakamura, G. Krost, J. Li, J. Xu, and F. Liu, "Harmonic characteristics of new HVDC transmission system based on new converter transformer," in *2008 Third International Conference on Electric Utility Deregulation and Restructuring and Power Technologies*, Apr. 2008, pp. 1868–1872.

- [13] J. D. Ainsworth, "Harmonic instability between controlled static convertors and a.c. networks," *Proceedings of the Institution of Electrical Engineers*, vol. 114, no. 7, pp. 949–957, Jul. 1967.
- [14] K. R. Padiyar, *Analysis of Subsynchronous Resonance in Power Systems*. Jan. 1999.
- [15] G. D. Irwin, A. K. Jindal, and A. L. Isaacs, "Sub-synchronous control interactions between type 3 wind turbines and series compensated AC transmission systems," in *2011 IEEE Power and Energy Society General Meeting*, Jul. 2011, pp. 1–6.
- [16] M. K. Das, A. M. Kulkarni, and P. B. Darji, "Comparison of DQ and Dynamic Phasor based frequency scanning analysis of grid-connected Power Electronic Systems," in *2016 Power Systems Computation Conference (PSCC)*, Jun. 2016, pp. 1–7.
- [17] L. P. Kunjumammed, B. C. Pal, C. Oates, and K. J. Dyke, "Electrical Oscillations in Wind Farm Systems: Analysis and Insight Based on Detailed Modeling," *IEEE Transactions on Sustainable Energy*, vol. 7, no. 1, pp. 51–62, Jan. 2016.
- [18] E. Ebrahimzadeh, F. Blaabjerg, X. Wang, and C. L. Bak, "Reducing Harmonic Instability and Resonance Problems in PMSG-Based Wind Farms," *IEEE Journal of Emerging and Selected Topics in Power Electronics*, vol. 6, no. 1, pp. 73–83, Mar. 2018.

- [19] C. Karawita and U. D. Annakkage, “Multi-Infeed HVDC Interaction Studies Using Small-Signal Stability Assessment,” *IEEE Transactions on Power Delivery*, vol. 24, no. 2, pp. 910–918, Apr. 2009.
- [20] X. Yue, X. Wang, and F. Blaabjerg, “Review of Small-Signal Modeling Methods Including Frequency-Coupling Dynamics of Power Converters,” *IEEE Transactions on Power Electronics*, vol. 34, no. 4, pp. 3313–3328, Apr. 2019.
- [21] M. Amin and M. Molinas, “Impedance Based Stability Analysis of VSC-Based HVDC System,” in *2015 IEEE Eindhoven PowerTech*, Jun. 2015, pp. 1–6.
- [22] C. Zhang, M. Molinas, A. Rygg, and X. Cai, “Impedance-based Analysis of Interconnected Power Electronics Systems: Impedance Network Modeling and Comparative Studies of Stability Criteria,” *IEEE Journal of Emerging and Selected Topics in Power Electronics*, pp. 1–1, 2019.
- [23] A. Rygg, “Impedance-based methods for small-signal analysis of systems dominated by power electronics,” PhD thesis, Oct. 2018.
- [24] M. Amin, “Small-signal Stability Characterization of Interaction Phenomena between HVDC System and Wind Farms,” PhD thesis, NTNU, 2017.
- [25] A. U. Rahman, I. Syed, and M. Ullah, “Small-Signal Stability Criteria in AC Distribution Systems—A Review,” *Electronics*, vol. 8, no. 2, 2019.
- [26] P. Kundur, *Power system stability and control*. New York: McGraw-hill, 1994.
- [27] M. K. Das, “D-Q and Dynamic Phasor based Frequency Scanning Analysis of Grid-Connected Power Electronic Systems,” PhD thesis, Indian Institute of Technology Bombay, Maharashtra, India, 2016.

- [28] R. D. Middlebrook, "Input filter considerations in design and application of switching regulators," in *Proc. IEEE Ind. Appl. Soc. Annu. Meet.*, 1976, pp. 366–382.
- [29] M. Belkhat, "Stability Criteria for AC Power Systems with Regulated Loads," PhD thesis, Purdue Univ., West Lafayette, IN, USA, 1997.
- [30] J. Sun, "Small-Signal Methods for AC Distributed Power Systems—A Review," *IEEE Transactions on Power Electronics*, vol. 24, no. 11, pp. 2545–2554, Nov. 2009.
- [31] J. Sun, "Impedance-Based Stability Criterion for Grid-Connected Inverters," *IEEE Transactions on Power Electronics*, vol. 26, no. 11, pp. 3075–3078, Nov. 2011.
- [32] A. Rygg and M. Molinas, "Apparent Impedance Analysis: A Small-Signal Method for Stability Analysis of Power Electronic-Based Systems," *IEEE Journal of Emerging and Selected Topics in Power Electronics*, vol. 5, no. 4, pp. 1474–1486, Dec. 2017.
- [33] B. Wen, D. Dong, D. Boroyevich, R. Burgos, P. Mattavelli, and Z. Shen, "Impedance-Based Analysis of Grid-Synchronization Stability for Three-Phase Paralleled Converters," *IEEE Transactions on Power Electronics*, vol. 31, no. 1, pp. 26–38, Jan. 2016.
- [34] A. Rygg, M. Molinas, C. Zhang, and Xu Cai, "Frequency-Dependent Aource and Load Impedances in Power Systems Based on Power Electronic Converters," in *2016 Power Systems Computation Conference (PSCC)*, Jun. 2016, pp. 1–8.

- [35] A. G. J. MacFarlane and I. Postlethwaite, "The Generalized Nyquist Stability Criterion and Multivariable Root Loci," *International Journal of Control*, vol. 25, no. 1, pp. 81–127, 1977.
- [36] L. Harnefors, M. Bongiorno, and S. Lundberg, "Input-Admittance Calculation and Shaping for Controlled Voltage-Source Converters," *IEEE Transactions on Industrial Electronics*, vol. 54, no. 6, pp. 3323–3334, Dec. 2007.
- [37] A. U. Rahman, I. Syed, and M. Ullah, "Small Signal Stability of a Balanced Three-Phase AC Microgrid Using Harmonic Linearization: Parametric-Based Analysis," *Electronics*, vol. 8, no. 1, 2018.
- [38] J. L. Moiola and G. Chen, *Hopf Bifurcation Analysis*.: World Scientific, 1996.
- [39] T. Roinila, M. Vilkkko, and J. Sun, "Online Grid Impedance Measurement Using Discrete-Interval Binary Sequence Injection," *IEEE Journal of Emerging and Selected Topics in Power Electronics*, vol. 2, no. 4, pp. 985–993, 2014.
- [40] Z. Shen, M. Jaksic, P. Mattavelli, D. Boroyevich, J. Verhulst, and M. Belkhat, "Three-phase AC system impedance measurement unit (IMU) using chirp signal injection," in *2013 Twenty-Eighth Annual IEEE Applied Power Electronics Conference and Exposition (APEC)*, 2013, pp. 2666–2673.
- [41] M. Cespedes and J. Sun, "Adaptive Control of Grid-Connected Inverters Based on Online Grid Impedance Measurements," *IEEE Transactions on Sustainable Energy*, vol. 5, no. 2, pp. 516–523, 2014.
- [42] N. Hoffmann and F. W. Fuchs, "Minimal Invasive Equivalent Grid Impedance Estimation in Inductive–Resistive Power Networks Using Extended Kalman

- Filter,” *IEEE Transactions on Power Electronics*, vol. 29, no. 2, pp. 631–641, 2014.
- [43] P. Xiao, G. K. Venayagamoorthy, K. A. Corzine, and J. Huang, “Recurrent Neural Networks Based Impedance Measurement Technique for Power Electronic Systems,” *IEEE Transactions on Power Electronics*, vol. 25, no. 2, pp. 382–390, 2010.
- [44] A. Rygg, M. Molinas, C. Zhang, and X. Cai, “A modified sequence-domain impedance definition and its equivalence to the dq-domain impedance definition for the stability analysis of ac power electronic systems,” *IEEE Journal of Emerging and Selected Topics in Power Electronics*, vol. 4, no. 4, pp. 1383–1396, 2016.
- [45] C. Li, R. Burgos, Y. Tang, and D. Boroyevich, “Application of D-Q frame impedance-based stability criterion in power systems with multiple STATCOMs in proximity,” in *IECON 2017 - 43rd Annual Conference of the IEEE Industrial Electronics Society*, Oct. 2017, pp. 126–131.
- [46] Xiao Jiang and A. M. Gole, “A frequency scanning method for the identification of harmonic instabilities in HVDC systems,” *IEEE Transactions on Power Delivery*, vol. 10, no. 4, pp. 1875–1881, Oct. 1995.
- [47] J. C. Das, *Power system analysis : short-circuit load flow and harmonics*. Boca Raton, 2012.
- [48] Y. Qi, H. Zhao, S. Fan, A. M. Gole, H. Ding, and I. T. Fernando, “Small Signal Frequency-Domain Model of a LCC-HVDC Converter Based on an Infinite

- Series-Converter Approach,” *IEEE Transactions on Power Delivery*, vol. 34, no. 1, pp. 95–106, Feb. 2019.
- [49] Y. Qi, A. M. Gole, and X. Chen, “Investigation of Sub-Synchronous Control Interaction for LCC Using the Generalized Nyquist Stability Criterion,” in *15th IET International Conference on AC and DC Power Transmission (ACDC 2019)*, Feb. 2019, pp. 1–6.
- [50] T. Kato, K. Inoue, and T. Sakiyama, “Stability Analysis Methods of a Grid-Connected Inverter in Time and Frequency Domains,” in *2018 International Power Electronics Conference (IPEC-Niigata 2018 -ECCE Asia)*, May 2018, pp. 2186–2192.
- [51] H. Zhang, Z. Liu, and S. Wu, “Sequence Impedance Modeling and Stability Analysis of Single-Phase Converters,” in *2018 21st International Conference on Electrical Machines and Systems (ICEMS)*, Oct. 2018, pp. 2234–2239.
- [52] Y. Wang, X. Wang, F. Blaabjerg, and Z. Chen, “Frequency Scanning-Based Stability Analysis Method for Grid-Connected Inverter System,” in *2017 IEEE 3rd International Future Energy Electronics Conference and ECCE Asia (IFEEC 2017 - ECCE Asia)*, Jun. 2017, pp. 1575–1580.
- [53] A. M. Kulkarni, M. K. Das, and A. M. Gole, “Frequency Scanning Analysis of STATCOM - Network Interactions,” in *2016 IEEE 6th International Conference on Power Systems (ICPS)*, Mar. 2016, pp. 1–6.
- [54] B. Wen, D. Boroyevich, R. Burgos, P. Mattavelli, and Z. Shen, “Small-Signal Stability Analysis of Three-Phase AC Systems in the Presence of Constant

- Power Loads Based on Measured d-q Frame Impedances,” *IEEE Transactions on Power Electronics*, vol. 30, no. 10, pp. 5952–5963, Oct. 2015.
- [55] S. Sanchez, G. Bergna, E. Berne, P. Egrot, J. .-.-. Vannier, and M. Molinas, “Frequency Scanning of Power Electronic-Based Smart Grids: The Modular Multilevel Converter Application,” in *2013 4th IEEE International Symposium on Power Electronics for Distributed Generation Systems (PEDG)*, Jul. 2013, pp. 1–8.
- [56] M. K. Das, A. M. Kulkarni, and A. M. Gole, “A screening Technique for Anticipating Network Instabilities in AC-DC Systems Using Sequence Impedances Obtained by Frequency Scanning,” in *10th IET International Conference on AC and DC Power Transmission (ACDC 2012)*, Dec. 2012, pp. 1–6.
- [57] M. Mohaddes, A. M. Gole, and S. Elez, “Steady state frequency response of STATCOM,” *IEEE Transactions on Power Delivery*, vol. 16, no. 1, pp. 18–23, Jan. 2001.
- [58] M. Das and A. Kulkarni, “Dynamic phasor based frequency scanning for grid-connected power electronic systems,” *Sādhanā*, vol. 42, no. 10, pp. 1717–1740, 2017.
- [59] R. Pintelon and J. Schoukens, “An Introduction to Identification,” in *System Identification: A Frequency Domain Approach*. IEEE, 2001.
- [60] A. Rygg, M. Molinas, C. Zhang, and X. Cai, “A Modified Sequence-Domain Impedance Definition and Its Equivalence to the dq-Domain Impedance Definition for the Stability Analysis of AC Power Electronic Systems,” *IEEE Journal*

- of Emerging and Selected Topics in Power Electronics*, vol. 4, no. 4, pp. 1383–1396, Dec. 2016.
- [61] *PSCAD/EMTDC User's guide*, Manitoba HVDC Research Centre, 2010, Winnipeg, Canada.
- [62] S. Shah and L. Parsa, "Impedance modeling of three-phase voltage source converters in dq, sequence, and phasor domains," *IEEE Transactions on Energy Conversion*, vol. 32, no. 3, pp. 1139–1150, Sep. 2017.
- [63] B. Wen, D. Boroyevich, R. Burgos, P. Mattavelli, and Z. Shen, "Analysis of D-Q Small-Signal Impedance of Grid-Tied Inverters," *IEEE Transactions on Power Electronics*, vol. 31, no. 1, pp. 675–687, Jan. 2016.
- [64] Y. Liao, Z. Liu, H. Zhang, and B. Wen, "Low-Frequency Stability Analysis of Single-Phase System With dq-Frame Impedance Approach—Part I: Impedance Modeling and Verification," *IEEE Transactions on Industry Applications*, vol. 54, no. 5, pp. 4999–5011, Sep. 2018.
- [65] B. Wen, D. Boroyevich, R. Burgos, P. Mattavelli, and Z. Shen, "Inverse nyquist stability criterion for grid-tied inverters," *IEEE Transactions on Power Electronics*, vol. 32, no. 2, pp. 1548–1556, Feb. 2017.
- [66] C. Desoer and Yung-Terng Wang, "On the generalized nyquist stability criterion," *IEEE Transactions on Automatic Control*, vol. 25, no. 2, pp. 187–196, 1980.
- [67] L. M. Wedepohl, H. V. Nguyen, and G. D. Irwin, "Frequency-dependent transformation matrices for untransposed transmission lines using Newton-Raphson

- method,” *IEEE Transactions on Power Systems*, vol. 11, no. 3, pp. 1538–1546, 1996.
- [68] G. F. Franklin, J. D. Powell, and A. Emami-Naeini, *Feedback control of dynamic systems*, Seventh edition. Boston: Pearson, 2014.
- [69] A. Gavrilovic, “AC/DC system strength as indicated by short circuit ratios,” in *International Conference on AC and DC Power Transmission*, 1991, pp. 27–32.
- [70] B. Badrzadeh, M. Sahni, Y. Zhou, D. Muthumuni, and A. Gole, “General methodology for analysis of sub-synchronous interaction in wind power plants,” *IEEE Transactions on Power Systems*, vol. 28, no. 2, pp. 1858–1869, 2013.